Design of Radio Frequency Pulses for Parallel Transmit Systems at High-Field MRI

Alessandro Sbrizzi

October 6, 2009

Contents

Introduction 5

1 Principles of Magnetic Resonance Imaging **9**
1.1 Proton spin and Larmor frequency 10
1.2 The Bloch Equation 11
1.3 Excitation by RF pulses 13
1.4 Signal 15
1.5 Gradient Fields and k-space formalism 17
1.6 Imaging 19
1.6.1 Slice Selection 19
1.6.2 Spatial Encoding 20

2 Two Dimensional Excitation Pulses **23**
2.1 Small tip angle approximation 23
2.2 An Analytic Solution 26
2.2.1 Reformulation of 2.4 in Terms of Fourier Transform . . 26
2.2.2 A Specific Case: Gaussian Profile and Spiral Trajectory 28
2.2.3 Considerations about the k-space scan: aliasing effects 31
2.3 Numerical Experiments 36

3 Parallel Transmit Systems **45**
3.1 SENSE 46
3.1.1 Parallel Imaging in MRI using Multiple Coils 46
3.1.2 Transmit SENSE 51
3.2 Regularized Least Square Problems 53
3.2.1 Specific Absorption Rate 57
3.2.2 The choice for an optimal λ value: the L-curve 57
3.3 Multishift CGLS 58
3.4 k-space trajectories: constraints and optimization 61

4 Numerical Simulations and Experiment. 69
4.1 Simulation 1 69
4.2 Simulation 2 76
4.3 Simulation 3 83
4.4 Simulation 4 93
4.5 Experiment 96

5 Conclusions and Outlook 99
5.1 The desired magnetization pattern 100
5.2 The B_1 (and B_0) maps 100
5.3 An optimal k-space trajectory 101
5.4 The Least Squares Problem and mCGLS 102
5.5 The choice of a good numerical solution 103
5.6 SAR computation 104
5.7 Implementation in the MRI hardware 104

A Derivation of the Normal Equations 107

B The Bloch Simulator 109

Introduction

Magnetic Resonance Imaging (MRI) is nowadays one of the best tools for non invasive inner inspection of the human body. Since 1978, that is, when the first studies on human being were performed, the number of applications of MRI for clinical purposes (in particular in fields like Oncology and Neurology) has constantly grown. Two of the main contributors to the development of the MRI techniques, namely Paul Lauterbur and Sir Peter Mansfield, were awarded the 2003 Nobel Prize in Medicine. Research on MRI still continues and at the present day is a subject of research involving the work of thousands of scientists around the world, whose results are reported in a comparable amount of publications each year. This great research effort is unveiling new aspects and new possibilities to exploit this imaging technique with great expectations for the future of medical imaging. Like it often happens in the scientific world, new discoveries are followed by new technical issues to be solved and the present work deals with some of such problems.
As a student of the Master Course in Scientific Computing at the Utrecht University, the author decided to conclude his studies with an internship at the Radiotherapy Department of the University Medical Center (UMC). In particular, he participated to the RF 7 Tesla (7T) MRI research group directed by Nico van den Berg. Also Hans Hoogduin from the 7 Tesla group of the Radiology Department gave fundamental contributions to the project. Beside the conventional 1.5T and 3T MRI scanners, the UMC owns a high field 7T MRI scanner.
High field MRI is a very promising research field, since images obtained making use of this high magnetic fields can be sharper and exhibit a greater level of detail than traditional MRI. More specifically, the ratio between the signal intensity and the noise from measurements (signal to noise ratio, SNR) is higher. Figure 1 shows an example of the difference in spatial resolution that is possible to achieve between a 1.5 T and a 7 T scanner.

High field MRI implies that radio waves have higher frequencies and thus shorter wavelengths. The shortening of wavelength causes standing waves

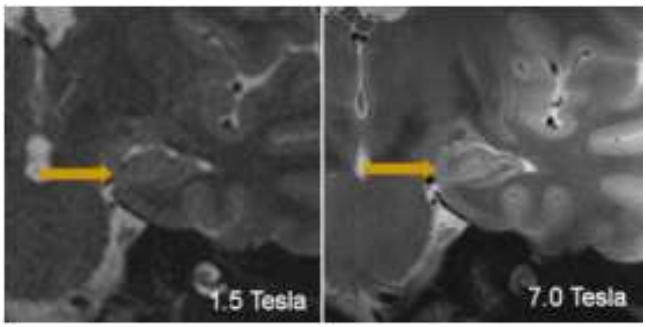

Figure 1: Difference in spatial resolution between two pictures taken by a 1.5 Tesla (left) and 7.0 Tesla (right) scanner.

and interference effects, resulting in the distortion of the magnetic fields inside an object whose dimensions are comparable to the wavelengths (for instance a human body).
This results in one of the major drawbacks of high field MRI: the magnetic field (B_1 field) caused by radio frequency (RF) coils is much less homogeneous. Since the RF field is responsible for the hydrogen spins magnetization and thus for generating the signal, little or no magnetization results in a loss of signal from the target region. As a consequence, some region of the patient's body could not be investigated accurately enough. See figure 2 for an example of an inhomogeneous magnetization obtained on a 7 Tesla MRI scanner (human pelvis region): the dark areas represent little or no magnetization.

To solve this problem, a technique called multidimensional spatially selective excitation (SSE) has been developed to obtain the desired magnetization (and hence a good signal) in the ROI (a necessary condition is that the inhomogeneities of the excitation RF field, i.e. the B_1 sensitivity profiles, are known). Exploiting this technique enables us to achieve *local* excitation and even to repair for the B_1 inhomogeneities and achieve an homogeneous magnetization over an extended area, like for instance, a slice of the whole brain. MRI is a relatively slow imaging technique, speed up of the whole process is sometimes necessary for certain applications. Since the excitation step requires usually too long RF pulses, efforts are being made to shorten this step. A possible solution is to employ parallel transmit systems: several channels send RF waves simultaneously and independently from each other (this is different from the conventional MRI, where one single transmit channel is usually employed) requiring a shorter pulse duration. The spatially selective excitation technique combined to the multichannel transmit system make thus possible a more accurate and faster imaging process.

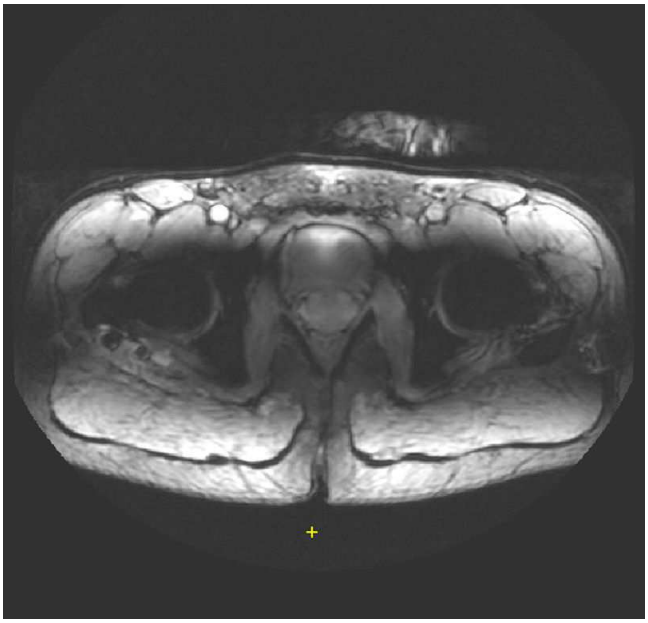

Figure 2: Inhomogeneity of excitation obtained by RF coils at 7 Tesla MRI for human pelvis region. The dark areas represent little or no magnetization.

The goals of the present work are:

- to explain the mathematical models describing the two above mentioned techniques, that is: multidimensional spatially selective excitation and parallel transmit systems
- to design and implement the algorithms aimed to find the proper RF pulses
- to validate the mathematical models by numerical simulations
- to describe and solve other problems related to the numerical process or constrained optimization procedures
- to present the first experiment on the UMC's Philips 7T MRI scanner.

In particular, the attention is focused on finding the RF pulses needed to excite a given region inside the human body in a predetermined way by mean of multiple transmit coils.
The electric fields produced by the RF coils cause heating of the object being scanned. This is expressed through a quantity called Specific Absorption Rate (SAR). For patient's safety reasons, the SAR must be kept under a certain maximum value. Since SAR evaluation asks for a large computational

burden, this is not implemented in the RF pulses optimization processes but rather computed after the desired RF pulse is known.
In Chapter 1 a description of the principles of magnetic resonance imaging is given. Readers already acquainted with this subject could skip this part, although a quick reading of it may be helpful since many notations are introduced there. In Chapters 2 and 3 the mathematical fundaments of the spatially selective excitation and parallel transmit system are studied. Chapter 3 contains also two sections devoted to the numerical solution of the Least Squares Problems and a section on a constrained optimization problem. Finally, in Chapter 4 several numerical simulations performed on a PC (the algorithms are implemented and run in MATLAB 7.4.0) and the result of an experiment on the 7T MRI scanner are reported.
The reader should have a basic knowledge of Fourier theory, (numerical) linear algebra and electromagnetism.

The author is grateful to his supervisors: Nico van den Berg at the UMC Radiotherapy Department and Gerard Sleijpen at the Mathematical Department of the Utrecht University. The discussions with them and their invaluable advices made possible this work. Furthermore, the author would like to thank Hans Hoogduin (UMC) for the brilliant work done to set up the two channels transmit system at the UMC's 7T scanner, making thus possible the experiment, and Astrid van Lier (UMC) for her work on the B_1 sensitivity maps.

Chapter 1

Principles of Magnetic Resonance Imaging

A MR-scanner (Figure 1.1) acts by combining Magnetic fields in various ways: the large magnet surrounding the patient induces a main static magnetic field, $\vec{B}_0$ along the longitudinal direction (feet to head). Other, much weaker and possibly varying in time, magnetic fields are superimposed to $\vec{B}_0$. They are induced by Gradient and Radio Frequency coils.

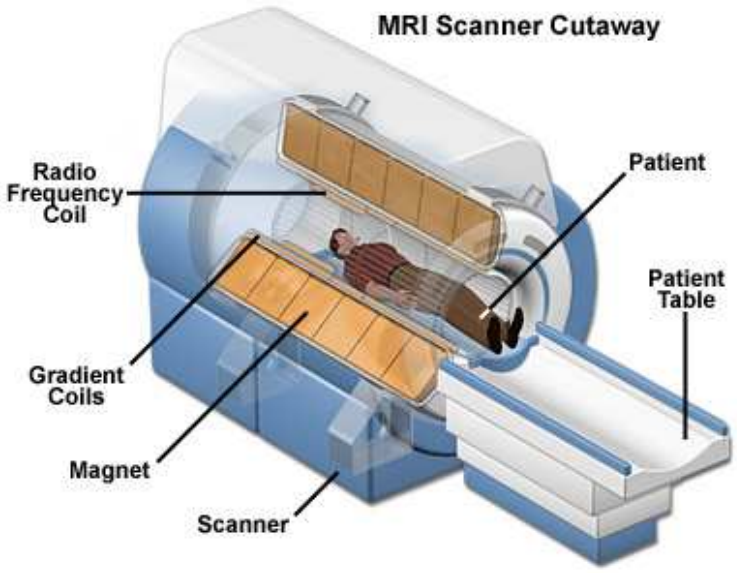

Figure 1.1: MRI-scanner (image taken from [2])

The goal of MRI is to measure the hydrogen spins density ρ at certain

points $\vec{r}$ in space. When $\rho(\vec{r})$ is known, a picture can be made representing the proton density and hence the type of tissue.
Protons can be seen as small magnets, when they undergo the main magnetic field ($\vec{B}_0$) they tend to align parallel or anti-parallel along the direction of the field. If they are brought out of this equilibrium position, they start to precess very much like a gyroscope. From this perturbed state, after a relaxation period, they will again align along the direction of the main field. During this relaxation process they release energy and this energy is proportional to their density.
In MRI this energy is measured in the form of induced currents along a coil (the radio-frequency coil). Other much weaker magnetic fields (gradients) are also applied in such a way that we are able to determine the spatial position of the protons causing this current.
A more detailed explanation of the whole process will follow below. The description relies on the classic interpretation of the atom model. An extensive treatment can be found in [1] and [4] while [3] contains a lot of very useful animations that can help to understand the underlying physical principles.

1.1 Proton spin and Larmor frequency

Protons can be considered as small, rotating, magnets (proton spins, $\vec{\mu}$). In presence of a magnetic field, they align along it, in parallel or anti-parallel way.
In presence of the magnetic field $\vec{B}$ the following relation holds:

$$\frac{d\vec{\mu}}{dt} = \gamma\vec{\mu} \times \vec{B}. \tag{1.1}$$

γ is called the gyromagnetic ratio and it depends on the type of proton. For an hydrogen proton (the most present in the human body and hence the most important for MRI) $\gamma \approx 2.68 \cdot 10^8$ rad/s/Tesla.
There is a strong analogy between the motion of the nuclear spins undergoing an external magnetic field and a gyroscope: when a torque acts on them, they start to wobble around the original equilibrium direction. In other words: if a magnetic field $\vec{B}$ is applied the spins start to precess (see figure 1.2).
Looking at Figure 1.2 we can write

$$|d\vec{\mu}| = \mu \sin\theta |d\phi|$$

and

$$|d\vec{\mu}| = \gamma|\vec{\mu} \times \vec{B}|dt = \gamma\mu B \sin\theta dt$$

The precession occurs with a given frequency, ω, which is called *Larmor frequency* and is given by:

$$\omega \equiv |\frac{d\phi}{dt}| = \gamma B$$

Therefore the Larmor frequency depends on the type of protons and on the magnetic field applied.

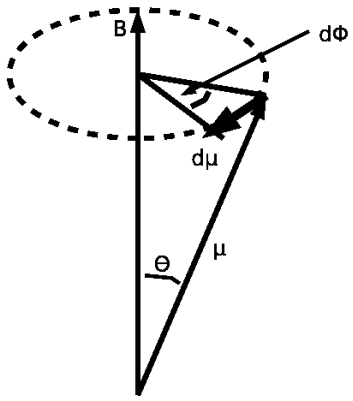

Figure 1.2: Precession of the proton spin: a magnetic field $\vec{B}$ not parallel to $\vec{\mu}$ is applied. The resulting torque is perpendicular to the plane containing $\vec{B}$ and $\vec{\mu}$ (equation 1.1). This torque causes a rotation of the spin by an angle $d\phi$ during the time interval dt.

1.2 The Bloch Equation

Summing up all proton spins inside a given volume V we obtain a net magnetic moment called *magnetization*:

$$\vec{M} \equiv \frac{1}{V}\sum \vec{\mu}$$

where the sum is taken over all the protons in the volume V.
Assume the protons do not interact with each other, then from equation

(1.1):

$$\frac{d\vec{M}}{dt} = \gamma \vec{M} \times \vec{B} \tag{1.2}$$

Suppose that the static main magnetic field lies along the z direction, i.e $\vec{B} = B_0\hat{z}$, then we define the z component of $\vec{M}$ (i.e. M_z) as the *longitudinal* magnetization and $\vec{M}_\perp = M_x\hat{x} + M_y\hat{y}$ the *transversal* component.
As spins do not rotate in phase, the sum of all the microscopic transverse magnetizations of each spin is a null transverse macroscopic magnetization: $\vec{M}_\perp = 0$. The only non zero component is the longitudinal magnetization.
We introduce a new reference frame, which rotates around the $\hat{z}$ axis at the same angular velocity as the spins do, that is, at Larmor frequency ω. We denote the quantities relative to this rotating system by primes (').
Formula 1.2 holds in case the protons do not interact with the surrounding environment. In practice, there are two main interaction : Spin-lattice interaction and Spin-Spin interaction. We will not discuss in detail these phenomena. It will suffice to say that the first has effect on the regrowth of the longitudinal component after a disturbance, the latter on the decay of transversal component (these regrowth and decay are called *relaxation* processes). Since in many MRI application it is important to know the longitudinal and transversal magnetization at given times, these interaction effects must be taken into account in the quantitative treatment. They are described by the following relations:

$$\frac{dM_z}{dt} = \frac{1}{T_1}(M_0 - M_z) \tag{1.3}$$

$$\left(\frac{d\vec{M}_\perp}{dt}\right)' = -\frac{1}{T_2}\vec{M}_\perp \quad \text{(rotating frame)} \tag{1.4}$$

where M_0 is the equilibrium value and T_1 and T_2 the relaxation times (proton-dependent). Suppose the magnetization is tipped away from the equilibrium and has components $\vec{M}(0) = (\vec{M}_\perp(0), M_z(0))$, then the respective solutions to the above equations are:

$$M_z(t) = M_z(0)e^{-t/T_1} + M_0(1 - e^{-t/T_1}) \tag{1.5}$$

$$\vec{M}_\perp(t) = \vec{M}_\perp(0)e^{-t/T_2} \quad \text{(rotating frame)} \tag{1.6}$$

The transverse component can be expressed in terms of the laboratory frame. If the the angular velocity of the rotating frame w.r.t. the laboratory is $\vec{\omega}_0 = \omega_0\hat{z}$, then the transversal magnetization in the laboratory frame , M_+ is given by

$$M_+(t) = e^{-i\omega_0 t - t/T_2}M_+(0) \tag{1.7}$$

where $M_+(t) \equiv M_x + iM_y$ (that is: the complex notation for a two dimensional vector). The absolute values of these solutions are plotted in figure 1.3.

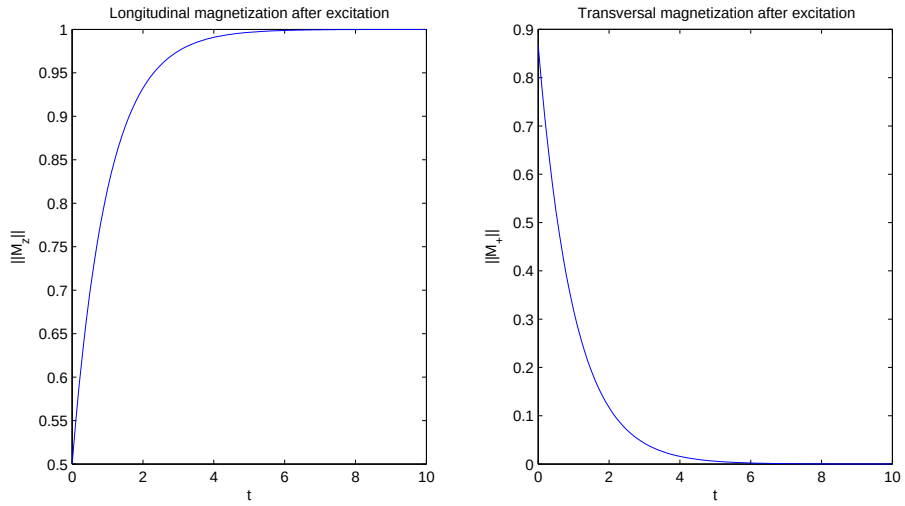

Figure 1.3: Regrowth of longitudinal magnetization (left) and decay of transversal magnetization (right) after excitation.

Including the relaxation effects in equation 1.2 we obtain the *Bloch Equation*:

$$\frac{d\vec{M}}{dt} = \gamma\vec{M} \times \vec{B} + \frac{1}{T_1}(M_0 - M_z)\hat{z} - \frac{1}{T_2}\vec{M}_\perp \tag{1.8}$$

1.3 Excitation by RF pulses

The scope of excitation is to bring the net magnetization $\vec{M}$ out of the equilibrium position and let it acquire a transversal component, see Figure 1.4. This is achieved by a radio frequency pulse (RF pulse) and we will denote its magnetic field by B_1.

The motion in a *rotating* frame with angular velocity $\vec{\Omega} = \Omega\hat{z}$ can be described by:

$$\left(\frac{d\vec{M}}{dt}\right)' = \gamma\vec{M} \times \left(\vec{B} + \frac{\vec{\Omega}}{\gamma}\right). \tag{1.9}$$

The term $\frac{\vec{\Omega}}{\gamma}$ represents a fictitious magnetic field (it is experienced only in the rotating frame). If $\vec{\Omega} = -\gamma\vec{B}$ then $\vec{M}$ in the rotating frame is constant. Suppose the magnetization is aligned along the z direction. To push the spins down and let them acquire a y' component we need a B_1 field that has

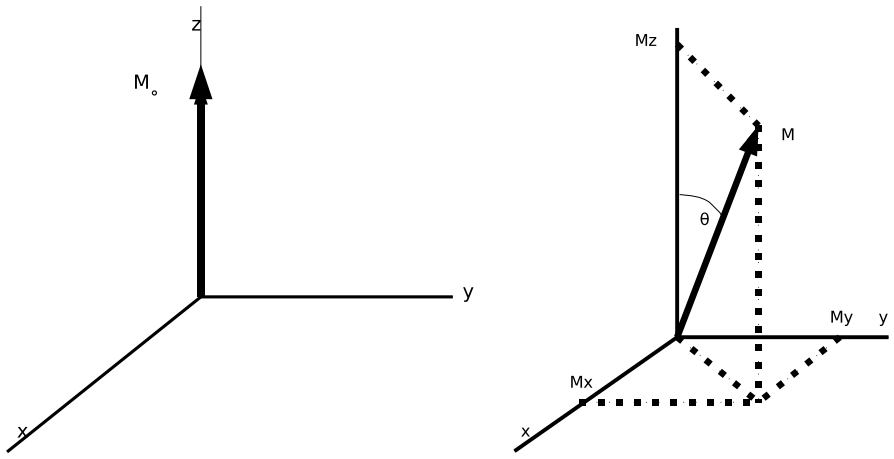

Figure 1.4: Effect of RF pulse excitation: the magnetization is originally aligned along the $\hat{z}$ axis. After the RF pulse application it is rotated by an angle θ and it has nonzero components in the xy-plane.

a x' component which is constant.
Suppose the B_1 field has the (polarized) form

$$\vec{B_1}(t) = b_1 \cos(\omega t)\hat{x}. \tag{1.10}$$

If the spin is precessing with frequency ω then the B_1 field is synchronized with it and every time the spin is back at a given position, it acquires a tip by the B_1 field. In this case the B_1 field is *on resonance*.
Take now $\Omega = -\omega\hat{z}$, then the following holds:

$$\hat{x}' = \hat{x}\cos\omega t - \hat{y}\sin\omega t \tag{1.11}$$
$$\hat{y}' = \hat{x}\sin\omega t + \hat{y}\cos\omega t \tag{1.12}$$

And inverting the above two formulas:

$$\hat{x} = \hat{x}'\cos\omega t + \hat{y}'\sin\omega t \tag{1.13}$$
$$\hat{y} = -\hat{x}'\sin\omega t + \hat{y}'\cos\omega t \tag{1.14}$$

From 1.10 we obtain:

$$\vec{B_1}(t) = \frac{1}{2}b_1\left[\hat{x}'(1+\cos 2\omega t) + \hat{y}'\sin 2\omega t\right]$$

that is: a constant term in the $\hat{x}'$ direction and two oscillating terms whose effects average to zero over times much larger than the RF period:

$$< \vec{B_1} >= \frac{1}{2}b_1\vec{x}'.$$

Note that only half of the original amplitude b_1 is available in the rotating frame. The field B_1 is called radio frequency pulse because the Larmor frequency ω lies in that range of frequencies.
If we choose

$$\vec{B_1} = \vec{B_1}(t) = b_1(\hat{x}\cos\omega t - \hat{y}\sin\omega t) \tag{1.15}$$

then we see immediately that $\vec{B_1} = b_1\hat{x}'$: the RF field is at rest in the rotating frame and is aligned along the $\hat{x}'$ axis. Furthermore, the full amplitude b_1 is now available also in the rotating frame. The effect of this constant magnetic field is to tip down $\vec{M}$ letting it rotate around the x'-axis. In the laboratory frame, this rotation about the x'-axis is superimposed to the precession about the z-axis, resulting in a downward spiral motion (see figure 1.5).

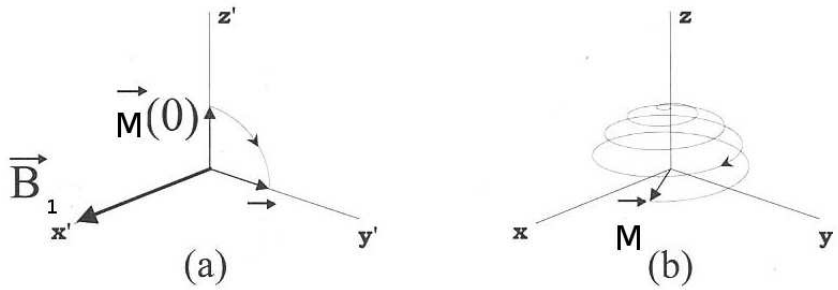

Figure 1.5: The motion of the magnetization vector $\vec{M}$ under effect of a RF pulse $\vec{B_1}$ which lies along the x' axis. Rotating frame (a) and laboratory frame (b).

The angle by which the magnetic spin is rotated from the equilibrium position (θ in figure 1.2) is called *flip* or *tip* angle and its dependence on b_1 is given by

$$\theta(t) = \gamma \int_0^t b_1(\tau)d\tau \tag{1.16}$$

It is common to refer to RF pulses as θ-pulses, that is: the RF pulses which achieve a flip angle θ.

1.4 Signal

After excitation with a 90^o-pulse around the x' axis, the spins precess in the transverse xy-plane. If a receive coil is present in the neighborhood, the

change in magnetic flux will give rise to a current in the coil (the Faraday's law). As effect of relaxation, the current will decay after some time. The measured signal (i.e. the induced current) is called the *free induction decay* (FID).
Again, suppose $\vec{B} = B_0\hat{z}$ and the sample has been excited such that , at time t, a nonzero transverse magnetization is present. Following the Faraday's law, the induced electromotive force emf is given by

$$\text{emf} = -\frac{d}{dt}\phi_M(t) = -\frac{d}{dt}\int_{\text{sample}} \vec{M}(\vec{r},t)\cdot\mathcal{B}(\vec{r})d^3r$$

where $\mathcal{B}$ represents a spatial weighting that relates the magnetic field at the original position and the magnetic field experienced at the coil's surface. It is important to note that $\vec{M}$ depends also on the position vector $\vec{r}$: image reconstruction is possible when we are able to determine the magnetization at all (discretized) spatial positions in the region of interest.
The signal $S(t)$ is proportional to the emf (the proportionality is dependent on the amplifier gain):

$$s(t) \sim -\frac{d}{dt}\int_{\text{sample}} \vec{M}(\vec{r},t)\cdot\mathcal{B}(\vec{r})d^3r \tag{1.17}$$

Using the complex notation for M_+ and the relations from (1.6) we can write

$$M_+(\vec{r},t) = e^{-t/T_2(\vec{r})}e^{-i\omega_0 t+\phi_0(\vec{r})}M_\perp(\vec{r},0)$$

where the phase ϕ_0 and magnitude $M_\perp(\vec{r},0)$ are determined by the initial RF pulse conditions. The precession frequency is here supposed to be space-independent and equal to the Larmor frequency. In a later stadium we will see how gradient fields will be applied, varying thus the precession frequency according to

$$\omega(\vec{r}) = \omega_0 + \Delta\omega(\vec{r}).$$

The Larmor frequency ω_0 is typically much larger (at least four orders of magnitude, that is, by a factor larger than 10^4) than the values of $1/T_1$ and $1/T_2$. In this case, taking the time derivative inside the integral in (1.17) we can neglect the derivative of the factors e^{-t/T_1} and e^{-t/T_2} . As consequence, the longitudinal magnetization M_z disappears and only the transversal component plays a role in the signal. This fact explains why the transversal magnetization M_+ or its magnitude $M_\perp = \sqrt{M_x^2 + M_y^2}$ are often referred to as *the signal*.

Suppose the transmitting and receiving RF coils are sufficiently uniform, then the initial magnetization phase ϕ_0 and the receive amplitude $\mathcal{B}_\perp$ are all independent on the position. Introducing the proportionality factor Λ which includes all these constants and makes Eq. (1.17) an equality, then

$$s(t) = \omega_0 \Lambda \mathcal{B}_\perp \int M_\perp(\vec{r}, 0) e^{i(\omega_0 t + \phi(\vec{r},t))} d^3r.$$

The angle ϕ is the accumulated phase and it is given by

$$\phi(\vec{r}, t) = -\int_0^t \omega(\vec{r}, \tau) d\tau.$$

Suppose at time $t = 0$ a perfect $\pi/2$ pulse has just been applied. This means that the initial transversal magnetization is simply the equilibrium magnetization M_0. The equilibrium magnetization can be expressed in terms of the proton spin density, then

$$s(t) = \int \rho(\vec{r}) e^{i(\omega_0 t + \phi(\vec{r},t))} d^3r \tag{1.18}$$

1.5 Gradient Fields and k-space formalism

In the following we restrict the treatment to one spatial dimension. The extension to two and three dimensions will follow at the end of the present section.
In the preceding section we derived an expression that relates the spin density ρ to the measured signal s. To determine the spatial position of $\rho(z)$ we introduce an additional magnetic field zG which is linearly dependent on the position. The resulting total magnetic field is the superposition of the static and the linear magnetic field:

$$B_z(z, t) = B_0 + zG(t).$$

G is called *Gradient* (spatial derivative of zG). Note that, due to this variation of the magnetic field, also the Larmor frequency ω is now spatially dependent:

$$\omega(z, t) = \omega_0 + \omega_G(z, t)$$

where $\omega_G = \gamma z G(t)$ is the deviation from the original Larmor frequency ω_0. The above described procedure will be exploited in what is called *frequency encoding along the z direction*. After a RF excitation, at time $t = 0$, if a gradient is applied, then the accumulated phase difference is

$$\phi_G(z, t) = -\gamma z \int_0^t G(\tau) d\tau$$

Ignoring any initial and spatially constant phase, the signal takes the form

$$s(t) = \int \rho(z) e^{i\phi_G(z,t)} dz = \int \rho(z) e^{-i2\pi z \gamma \int_0^t G(\tau) d\tau} dz$$

(here we introduce the quantity $\gamma \equiv \gamma/2\pi$).
The fundamental step is to introduce the *spatial frequency*

$$k = k(t) \equiv \gamma \int_0^t G(\tau) d\tau$$

and to rewrite the signal as :

$$s(k) = \int \rho(z) e^{-i2\pi kz} dz \tag{1.19}$$

that is: *the signal is the Fourier Transform of the spin density.* This fact implies that formula (1.19) can be easily inverted to obtain

$$\rho(z) = \int s(k) e^{2\pi kz} dk.$$

Furthermore, after discretization of Equation (1.19), the Fast Fourier Transform Algorithm can be applied to compute the spin density in the notorious efficient way.
The spatial frequency k should vary from $-\infty$ to $+\infty$ (that is, the integral should be taken over the interval $I_k \equiv (-\infty, +\infty)$). This interval is called the *k-space*. For practical reasons, the process is discretized and the k-space reduced to a bounded interval I_k such that

$$I_k = [-k_{max}, -k_{max} + \Delta k, -k_{max} + 2\Delta k, \ldots, k_{max} - \Delta k, k_{max}]$$

where k_{max} and Δk are determined by the desired spatial resolution of the image (the relation between frequency domain sampling and spatial domain resolution is described by the Nyquist sampling criterion [1]).
Note that the k-space coverage is affected by relaxation effects: sampling a large number of frequencies requires a longer signal in time. Decay of transversal magnetization will affect the quality of the signal if this becomes too long.

The above described process can be extended to two (or three) dimensions. In case of 2D imaging in the xy-plane, formula 1.19 becomes

$$s(\vec{k}) = \int \rho(\vec{r}) e^{-i2\pi \vec{k} \cdot \vec{r}} d^2 r \tag{1.20}$$

with $\vec{r} = (x, y)$ and

$$\vec{k} = (k_x, k_y) = (\gamma \int_0^t G_x(\tau)d\tau, \gamma \int_0^t G_y(\tau)d\tau) \tag{1.21}$$

The Gradient magnetic field has 2 components: $xG_x(t)$ and $yG_y(t)$ and the k-space is now a 2D interval and it is often referred to as k-plane.
An analogous k-space formulation can be developed for the transmit (excitation by RF-pulse) procedure. This subject will be studied in the next chapter.

1.6 Imaging

The process of imaging requires a spatial determination of the spin density. In the previous sections we have seen how this can be achieved by means of additional magnetic fields. A common procedure in MRI is 2D imaging. It consists of two main step:

1. Slice Selection: only the spins belonging to a thin slice of the object being scanned are excited by a slice selective RF pulse and a gradient orthogonal to the slice;

2. Spatial Encoding: a 2 dimensional Gradient is applied during relaxation and the 2D spatial encoding is acquired through the measured signal. The image is then obtained by inverse 2D FFT applied to this signal.

1.6.1 Slice Selection

Suppose a patient lies in a MRI scan and we want to image a slice of a patient on the xy-plane (transverse plane). Applying a Gradient $G_z(t)$ along the z direction causes the Larmor frequency to vary along the same direction. In this case, the resonance frequency in the rotating reference frame will be

$$f(z, t) = \gamma G_z(t) z$$

To excite the spins and bring them out of the equilibrium position the RF frequency should match the Larmor frequency. The frequency content of a transmit RF field B_1 is given by its Fourier Transform

$$B_{1,\perp}(\vec{r}, f(z)) = \int_{-\infty}^{\infty} B_{1,\perp}(\vec{r}, t) e^{-i2\pi f(z)t} dt \quad (1.22)$$

$$= \int_{-\infty}^{\infty} B_{1,\perp}(\vec{r}, t) e^{-i2\pi \gamma G_z(t) z t} dt \quad (1.23)$$

$$= \int_{-\infty}^{\infty} B_{1,\perp}(\vec{r}, t) e^{-i2\pi k(t) z} dt \quad (1.24)$$

where we assumed G_z is constant is time and hence $k(t) = \gamma G_z t$. Substituting and rewriting in terms of k :

$$B_{1,\perp}(\vec{r}, z) = \frac{1}{\gamma G_z} \int_{-\infty}^{\infty} B_{1,\perp}(\vec{r}, k) e^{-i2\pi k z} dk.$$

Assume we want to select a slice of thickness Δz whose center is z_0, i.e. $z \in [z_0 - \Delta z/2, z_0 + \Delta z/2]$. In this case the frequency range of $B_{1,\perp}(\vec{r}, k)$ should be $[f(z_0 - \Delta z/2), f(z_0 + \Delta z/2)]$. Since we wish a uniform profile, the Frequency response should resemble a boxcar function with support $[f(z_0 - \Delta z/2), f(z_0 + \Delta z/2)]$. The inverse Fourier Transform of a boxcar profile is a sinc function. The RF should have a sinc shaped amplitude $B_{1,\perp}$ to obtain a perfectly homogeneous slice selection. (Of course a sinc function is impossible to implement in any hardware since its support is unbounded and it must be truncated. To reduce Gibbs effects, the truncated sinc could be multiplied by a window function) .
In conclusion: the simultaneous application of a constant gradient along the longitudinal z-direction and a sinc shaped RF along the transversal plane causes only the spins in the range $[z_0 - \Delta z/2, z_0 + \Delta z/2]$ to be excited.
Note that the $B_{1,\perp}$ profile is the RF measured in the rotating frame whose angular velocity w.r.t the laboratory frame is $\omega = 2\pi f(z_0)$. In the laboratory frame this is the *envelope* of the RF pulse, which has the form given by equation (1.15) with $b_1 = B_{1,\perp}$.

1.6.2 Spatial Encoding

Once the slice selective excitation is obtained, the RF and G_z are turned off. During the relaxation, the Gradients G_x and G_y are switched on and the signal is collected. In the section about the gradients field we saw how spatial encoding is possible by mean of different gradients combinations.
The G_x gradient is responsible for the frequency encoding step. A *phase encoding* step can be achieved in a similar manner with the G_y component (phases, like resonance frequencies, are dependent on the position) . The

way these two gradients are applied determine the type of k-plane scanning. The path described by $\vec{k}(t) = \vec{k}(G_x(t), G_y(t))$ is called the *k-space trajectory*. In a typical 2D sequence, called Echo-planar, the k space is scanned on a rectangular grid, the individual k-space trajectories run parallel to the k_x-axis from k_{min} to k_{max} (see figure 1.6) resulting in a Inverse Discrete Fourier Transform Matrix which can be easily transformed back to the reconstructed image.

To achieve this k-trajectory, first a the G_y gradient is applied and then

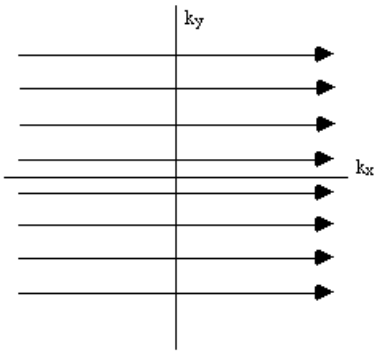

Figure 1.6: k trajectory for echo-planar imaging

the G_x. This sequence is repeated until the whole k-plane is covered. The frequency encoding step (corresponding to the application of G_x) is also called *readout* because the data is collected during this stage. See figure 1.7 for a sequence diagram displaying schematically the whole process.

The echo-planar imaging is only one among several ways to run through the k-space. In case of non linear paths, the data must be first interpolated to a uniform cartesian rectangular grid to apply inverse FFT. In the following chapters a particular class of trajectories, the spirals, will be studied and employed.

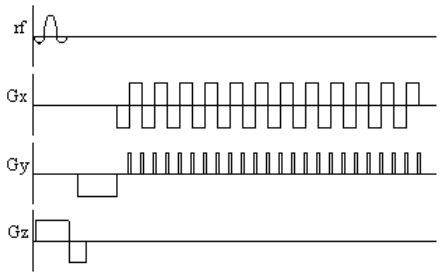

Figure 1.7: Sequence diagram showing the different steps in echo-planar imaging. The horizontal axis represents the time. First a slice selective sinc RF-pulse is applied simultaneously to a G_z gradient. After that, the k-plane scanning starts: a first negative G_y and G_x cause the scan to start from the bottom left corner of the k-plane. A first positive G_x lobe moves the trajectory to the right. A short G_y moves up the trajectory by a Δk_y step and a negative G_x brings it to the left. The procedure is repeated until the whole k-plane is scanned.

Chapter 2

Two Dimensional Excitation Pulses

In the previous chapter we have seen how a selective excitation can be obtained by the simultaneous application of a gradient field and a RF pulse. This selectivity is one dimensional, that is, only along one dimension (in that specific case the $\hat{z}$ axis). The result is that only the spins belonging to a given slice parallel to the xy-plane are excited, i.e. brought out from the equilibrium position. In this chapter we will describe a method to obtain a two dimensional spatial selectivity that enable us to excite a specific region of a plane according to a previous determined pattern.
Suppose for instance that we want to obtain a 20^o flip angle excitation only over a disc of radius 1 cm centered at (2,-2) in the xy-plane. The magnetization profile will be that displayed in figure 2.1, that is: $M_\perp = M_0 \sin 20^o \approx 0.342 M_0$ inside the disc and $M_\perp = 0$ outside.

2.1 Small tip angle approximation

To be able to produce a 2 dimensional selectivity we must find an expression which relates the desired magnetization to the gradient fields and the RF pulse. The Bloch equation (1.8) describes the process of excitation and relaxation as consequence of the applied magnetic fields: static ($B_0\hat{z}$), gradients ($(\vec{G}\cdot\vec{r})\hat{z}$) and RF ($\vec{B}_1$).
Suppose the whole process is taking place in a time much shorter then the relaxation times T_1 and T_2. Neglecting the relaxation effects, the Bloch equa-

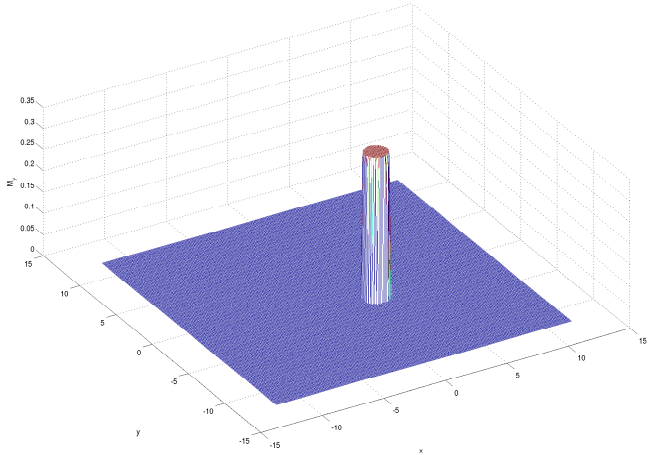

Figure 2.1: A magnetization profile. In the plane xy (measures in cm) a unit circle centered at (2,-2) is excited such that $M_\perp = M_0 \sin 20^o$. Here $M_0 = 1$.

tion takes the simpler form

$$\frac{d\vec{M}}{dt} = \gamma \vec{M} \times \vec{B}$$

where $\vec{M} = \vec{M}(\vec{r}, t)$ and $\vec{B}$ is the net magnetic field: $\vec{B} = (B_0 + \vec{G} \cdot \vec{r})\hat{z} + \vec{B}_1$. In the frame rotating at the Larmor frequency the effect of the static field B_0 is not perceived and the Bloch equation in this rotating frame becomes

$$\frac{d\vec{M}}{dt} = \gamma \vec{M} \times \left(\vec{B}_1 + (\vec{G} \cdot \vec{r})\hat{z} \right). \tag{2.1}$$

Suppose the RF field $\vec{B}_1$ lies on the xy plane (we have studied this situation in the previous chapter), that is: $\vec{B}_1 = (B_{1x}, B_{1y}, 0)$. Working out the cross product in (2.1) we obtain:

$$\frac{d\vec{M}}{dt} = \begin{pmatrix} 0 & \gamma \vec{G} \cdot \vec{r} & -\gamma B_{1,y} \\ -\gamma \vec{G} \cdot \vec{r} & 0 & \gamma B_{1,x} \\ \gamma B_{1,y} & -\gamma B_{1,x} & 0 \end{pmatrix} \begin{pmatrix} M_x \\ M_y \\ M_z \end{pmatrix}. \tag{2.2}$$

Remember that the initial condition to the Bloch equation is:

$$\vec{M}(0) = (0, 0, M_0)^T.$$

At this point comes a crucial step: to obtain an analytical expression for the solution to (2.2) we make the following assumption [5]:

the flip angle θ is small and the z component of $\vec{M}$ is constant, that is,

$$M_z(t) = M_0 \cos\theta(t) \approx M_0.$$

Writing the transverse Magnetization and the applied RF field in complex form:

$$\begin{aligned} M_\perp &= M_x + i\, M_y \\ B_1 &= B_{1,x} + i\, B_{1,y} \end{aligned}$$

equation 2.2 can be rewritten as:

$$\frac{dM_\perp}{dt} = -i\gamma \vec{G} \cdot \vec{r} M_\perp + i\gamma B_1 M_0,$$

that is: a first order linear nonhomogenous ordinary differential equation. The solution to this equation is given by

$$M_\perp(\vec{r}, T) = i\gamma M_0 \int_0^T B_1(t) e^{-i\gamma \vec{r} \cdot \int_t^T \vec{G}(s) ds} dt.$$

Analogously to what we did in the imaging step (see previous chapter), we introduce the k-space interpretation by defining

$$\vec{k}(t) \equiv -\gamma \int_t^T \vec{G}(s) ds. \tag{2.3}$$

In this case the solution to (2.2) becomes

$$\boxed{M_\perp(\vec{r}, T) = i\gamma M_0 \int_0^T B_1(t) e^{i\vec{r} \cdot \vec{k}(t)} dt} \tag{2.4}$$

Formula (2.4) is of fundamental importance for this project. The main concern from now on will be to find the RF profile $B_1(t)$ given a well suited $\vec{k}(t)$ trajectory (and hence Gradient fields) to obtain a desired, a priori determined, transversal magnetization profile $M_\perp$: this will be achieved by solving (2.4) for $B_1(t)$ given $\vec{k}(t)$ and $M_\perp$. Putting it in mathematical terms: we are interested to the solution $f(t)$ of the *Fredholm Integral Equation* (first kind)

$$g(\vec{r}) = \int_a^b f(t) K(\vec{r}, t)\, dt$$

with the unknown

$$f(t) = B_1(t)$$

and the known

$$\begin{aligned} g(\vec{r}) &= M_\perp(\vec{r}) \\ K(\vec{r},t) &= e^{i\vec{r}\cdot\vec{k}(t)} \\ a &= 0 \\ b &= T. \end{aligned}$$

The quantity T will be referred to as the *pulse length*.

2.2 An Analytic Solution

John Pauly et al. [5] derived an approximated solution in analytical form for a specific case of equation 2.4, that is, when $M_\perp(\vec{r}) = \mu_1 e^{-\mu_2^2|\vec{r}|^2}$ with μ_1 and μ_2 two parameters. This approximated solution will be useful to test the reliability of the mathematical procedure explained above. Also, we will use this reference solution in numerical simulations later on.
We will report the derivation and work out some details. Helpful informations can also be found in [7].

2.2.1 Reformulation of 2.4 in Terms of Fourier Transform

The right hand side of (2.4) suggests that the same formula could be expressed as an Inverse Fourier Transform involving $\vec{k}$ and $\vec{r}$ as variables for frequency and time respectively. Of course, the integral in (2.4) is over a one dimensional time interval while $\vec{k}$ and $\vec{r}$ are three dimensional vectors. To 'translate' the problem to a n-dimensional integral, a multidimensional delta function δ is applied.
For a delta function the *sifting* property holds:

$$\int_{-\infty}^{\infty} f(t)\delta(t-T)\,dt = f(T).$$

The same property holds for a n-dimensional delta function which is defined as

$$\delta^n(\vec{x}) \equiv \delta(x_1)\delta(x_2)\ldots\delta(x_{n-1})\delta(x_n), \quad \vec{x} = (x_1, x_2, \ldots, x_{n-1}, x_n) \in \mathbb{R}^n$$

Then

$$\int_{\mathbb{R}^n} f(\vec{\xi})\delta^n(\vec{\xi}-\vec{x})d\vec{\xi} = f(\vec{x}).$$

Making use of this fact we can rewrite (2.4) as

$$M_\perp(\vec{r},T) = i\gamma M_0 \int_0^T B_1(t) \int_{\mathbb{K}} \delta^n(\vec{k}(t)-\vec{\kappa})e^{i\vec{r}\cdot\vec{\kappa}}d\vec{\kappa}dt$$

where $\mathbb{K}$ denotes the n-dimensional k-space. Interchanging the integrals

$$M_\perp(\vec{r},T) = i\gamma M_0 \int_{\mathbb{K}} \left(\int_0^T B_1(t)\delta^n(\vec{k}(t)-\vec{\kappa})dt \right) e^{i\vec{r}\cdot\vec{\kappa}}d\vec{\kappa}.$$

The term within brackets can be rewritten as

$$p(\vec{\kappa}) = \int_0^T B_1(t)\delta^n(\vec{k}(t)-\vec{\kappa})dt = \int_0^T \frac{B_1(t)}{|\gamma\vec{G}(t)|} \left(\delta^n(\vec{k}(t)-\vec{\kappa})|\dot{\vec{k}}(t)| \right) dt$$

where we used the fact

$$\dot{\vec{k}}(t) \equiv \frac{d\vec{k}(t)}{dt} = \gamma\vec{G}(t)$$

following from (2.3).
Setting

$$W(\vec{k}(t)) \equiv \frac{B_1(t)}{|\gamma\vec{G}(t)|} \tag{2.5}$$

we have

$$p(\vec{\kappa}) = \int_0^T W(\vec{k}(t)) \left(\delta^n(\vec{k}(t)-\vec{\kappa})|\dot{\vec{k}}(t)| \right) dt = W(\vec{\kappa}) \int_0^T \left(\delta^n(\vec{k}(t)-\vec{\kappa})|\dot{\vec{k}}(t)| \right) dt \tag{2.6}$$

which follows from the property

$$f(x)\delta(x-x_0) = f(x_0)\delta(x-x_0).$$

The term to the right in (2.6) contains a change of variable formulation of the form

$$\int_{\mathbb{R}} \delta(g(x))|g'(x)|dx = \int_{g(\mathbb{R})} \delta(u)\, du,$$

therefore one can see $p(\vec{\kappa})$ as a path that scans the k-space with a k-space dependent weight $W(\vec{\kappa})$ following the unit weight trajectory $S(\vec{\kappa})$ given by

$$S(\vec{\kappa}) \equiv \int_0^T \left(\delta^n(\vec{k}(t)-\vec{\kappa})|\dot{\vec{k}}(t)| \right) dt.$$

Putting all these results together, we conclude that:

$$M_\perp = i\gamma M_0 \int_{\mathbb{K}} W(\vec{\kappa}) S(\vec{\kappa}) e^{i\vec{r}\cdot\vec{\kappa}} d\vec{\kappa}. \tag{2.7}$$

We obtained what we wished: a Fourier Transform relation between $M_\perp$ and B_1 as function of $\vec{r}$ and $\vec{\kappa}$.
Assume that W is a smooth function and the k-space trajectory $\vec{k}(t)$ scans $\mathbb{K}$ with sufficient density and completely, that is, where the Fourier coefficients have significant energy. Look, for a practical example, at Figure 2.2 where a smooth function W (left picture) is sampled following a spiral trajectory over a two dimensional k-space: the sampled function WS can be a good approximation for W if the integral in (2.7) is computed. Making thus the following approximation:

$$\int_{\mathbb{K}} W(\vec{\kappa}) S(\vec{\kappa}) e^{i\vec{r}\cdot\vec{\kappa}} d\vec{\kappa} = \int_{\mathbb{K}} W(\vec{\kappa}) e^{i\vec{r}\cdot\vec{\kappa}} d\vec{\kappa}$$

Equation (2.7) becomes

$$M_\perp(\vec{r}) = i\gamma M_0 \int_{\mathbb{K}} W(\vec{k}) e^{i\vec{r}\cdot\vec{k}} d\vec{k} \tag{2.8}$$

where, from (2.5):

$$W(\vec{k}(t)) = \frac{B_1(t)}{|d\vec{k}(t)/dt|}.$$

This implies that the desired magnetization pattern can be seen as the (Inverse) Fourier Transform of the RF pulse, weighted by the reciprocal of $|\gamma\vec{G}(t)|$.

2.2.2 A Specific Case: Gaussian Profile and Spiral Trajectory

The Fourier Relationship between $M_\perp$ and B_1 explains why the choice

$$M_\perp(\vec{r}) = \mu_1 e^{-\mu_2^2 |\vec{r}|^2} \tag{2.9}$$

can be practical for our scope: the Fourier Transform of a Gaussian is again a Gaussian. We could therefore restrict the k-space scan (in this case $\mathbb{K} = \mathbb{R}^2$) to the (circular) area where the Fourier Coefficients has sufficient magnitude to obtain an accurate solution. Furthermore a Gaussian profile can be useful for the spatially selective excitation: given a point $\vec{r}_0$ of interest we can

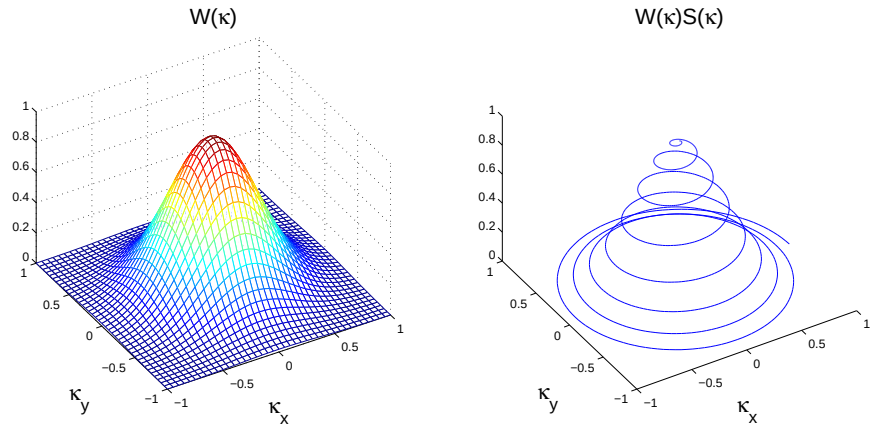

Figure 2.2: A smooth function W (left picture) is sampled following a spiral trajectory over a two dimensional k-space (right picture).

center the Gaussian at $\vec{r}_0$ and derive the respective RF pulse. We assume, for simplicity, that $\vec{r}_0 = 0$.

The Fourier transform W of $M_\perp$ will have the form

$$W(\vec{k}) = \alpha_1 e^{-\alpha_2^2|\vec{k}|^2}.$$

To find expressions for the coefficients α_1 and α_2 write out (2.8):

$$\begin{aligned} \mu_1 e^{-\mu_2^2|\vec{r}|^2} &= i\gamma M_0 \int_{\mathbb{K}} W(\vec{k}) e^{i\vec{r}\cdot\vec{k}} d\vec{k} = i\gamma M_0 \int_{\mathbb{R}^2} \alpha_1 e^{-\alpha_2^2|\vec{k}|^2} e^{i\vec{r}\cdot\vec{k}} d\vec{k} = \\ &= \frac{i\gamma M_0 \alpha_1 \pi}{\alpha_2^2} e^{-(1/2\alpha_2)^2|\vec{r}|^2}. \end{aligned}$$

It follows that

$$\begin{aligned} \alpha_2 &= \frac{1}{2\mu_2} \\ \text{and} \quad \alpha_1 &= \frac{\mu_1}{4M_0\gamma\pi\mu_2^2}. \end{aligned}$$

In conclusion, from (2.5):

$$B_1(t) = W(\vec{k}(t))|d\vec{k}(t)/dt| = \frac{\mu_1}{4M_0\gamma\pi\mu_2^2} e^{-\frac{|\vec{k}|^2}{(2\mu_2)^2}} |d\vec{k}(t)/dt|. \tag{2.10}$$

The above expression for B_1 is an approximated solution to (2.4) in analytic form. It depends on the path employed to scan the k-space and relies

on the assumptions made in the previous section regarding W and $\vec{k}(t)$. A variety of possibilities for $\vec{k}(t)$ could be exploited, we will choose a constant angular rate spiral trajectory of the form

$$\begin{aligned} k_x(t) &= A\left(1-\frac{t}{T}\right)\cos\frac{2\pi nt}{T} \\ k_y(t) &= A\left(1-\frac{t}{T}\right)\sin\frac{2\pi nt}{T}. \end{aligned} \tag{2.11}$$

In the above expression, A denote the maximal radius and n the number of spiral interleaves (see figure 2.3 for an example).

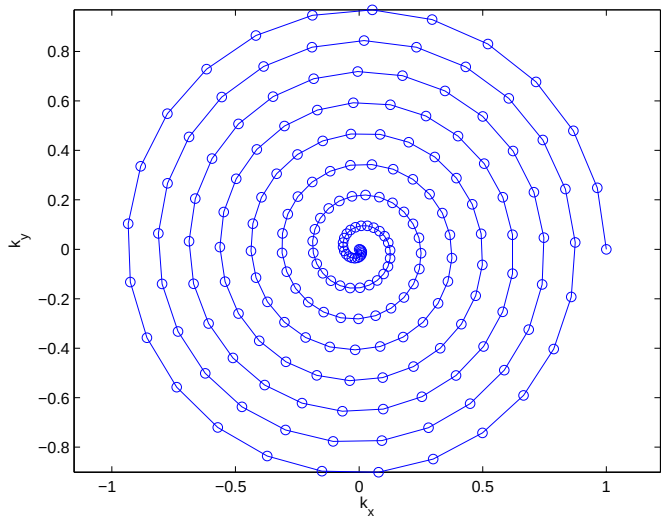

Figure 2.3: A constant angular rate spiral trajectory with $A = 1$ and $n = 8$. The circles denote points on the trajectory at the same time-distance, that is $\vec{k}(t_j)$ with $t_j = j\Delta t$ and $j = 0, 1, 2, \ldots$.

Note that the spiral ends at $\vec{k}(T) = 0$: this fact has practical advantages in application since the spins do not need an extra gradient to refocus them (they are automatically refocused).

The gradient is given by $\vec{G}(t) = \dot{\vec{k}}(t)/\gamma$:

$$\begin{aligned} G_x(t) &= -\frac{A}{\gamma T}\left[2\pi n\left(1-\frac{t}{T}\right)\sin\frac{2\pi nt}{T}+\cos\frac{2\pi nt}{T}\right] \\ G_y(t) &= \frac{A}{\gamma T}\left[2\pi n\left(1-\frac{t}{T}\right)\cos\frac{2\pi nt}{T}-\sin\frac{2\pi nt}{T}\right]. \end{aligned}$$

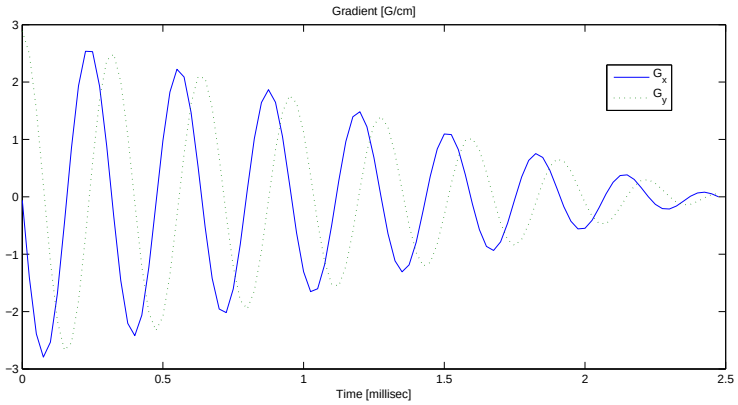

Figure 2.4: Gradient for $n = 8$. Solid line for G_x and dotted line for G_y

A plot for $n = 8$ is given in figure 2.4
For these values of $\vec{k}(t)$ and $\vec{G}(t)$ it is easy to see that

$$\begin{aligned} |\vec{k}(t)|^2 &= A^2\left(1-\frac{t}{T}\right)^2 \\ |\dot{\vec{k}}(t)| &= \gamma|\vec{G}(t)| = \gamma\frac{A}{T}\sqrt{\left[2\pi n\left(1-\frac{t}{T}\right)\right]^2+1} \end{aligned}$$

and substituting in (2.10) we obtain the requested $B_1(t)$ (see also figure 2.5):

$$B_1(t) = \frac{A\mu_1}{4M_0\pi T\mu_2^2} e^{-\frac{A^2\left(1-\frac{t}{T}\right)^2}{(2\mu_2)^2}} \sqrt{\left[2\pi n\left(1-\frac{t}{T}\right)\right]^2+1}. \qquad (2.12)$$

.

Of course, formula (2.12) was obtained under the assumptions regarding W and $\vec{f}(t)$. Suppose that $n = 8$ and $A = 1$ as in the previous case for $\vec{k}(t)$. For the Gaussian function W like that displayed in Figure 2.2 the assumptions are realistic. This may not be the case if another Gaussian profile is employed (see for instance Figure 2.6). The dependence of A and n on the k-space scanning is investigated in the following section.

2.2.3 Considerations about the k-space scan: aliasing effects

An effective choice of A and n in the spiral trajectory has to depend on the problem. In addition to that, a discretization of the gradients has to

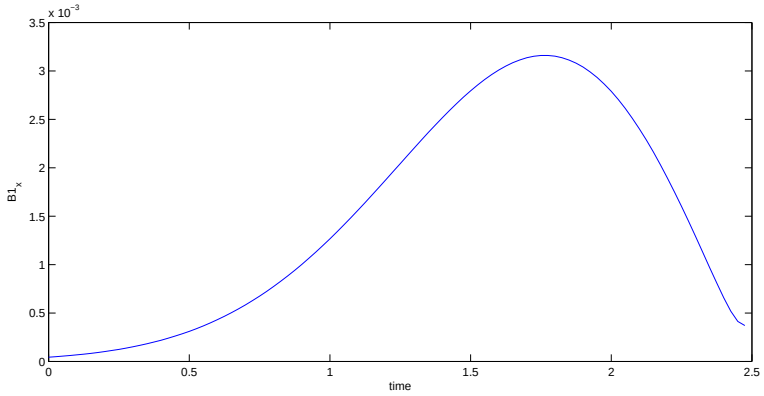

Figure 2.5: $B_1(t)$ given by formula (2.12).

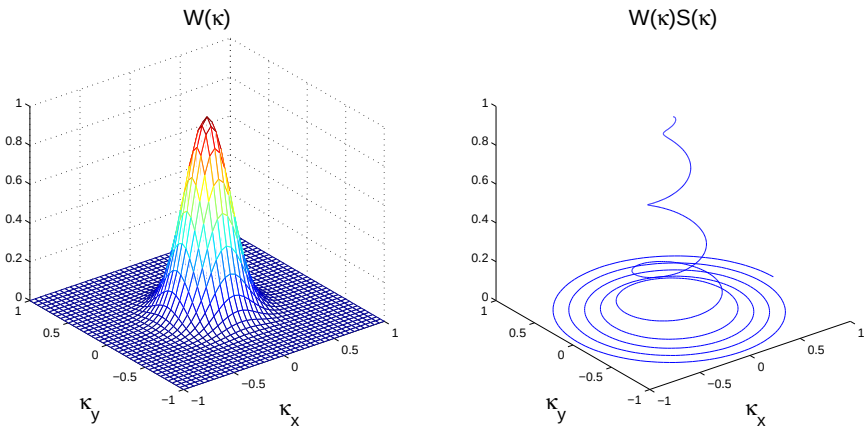

Figure 2.6: A Gaussian function W (left picture) is sampled following a spiral trajectory over a two dimensional k-space (right picture). The assumptions regarding W and $\vec{k}(t)$ are no longer realistic.

be performed (Gradient coils work with discretized signals). We denote the number of Gradient sample points by N_t (note that this is the same as for the k space trajectory samples). Therefore we need expressions for n, A and N_t which make the assumptions regarding W and $\vec{k}(t)$ realistic and enable us to obtain an accurate reconstruction of the desired magnetization profile. We suppose the following are given:

- the desired transversal magnetization profile $M_\perp(\vec{r})$
- the spatial resolution of the desired magnetization Δr
- the distance of the first alias to the center L
- the time sampling interval Δt.

First, we would like to restrict the k-space scanning to the (circular) area where the Fourier transform of the desired magnetization has sufficient power, therefore we set

$$A = \max_{k \in \mathbb{K}} \{|\vec{k}| : |W(\vec{k})| \geq v\}$$

and v a (small) threshold value to be determined. In this way we are sure that all the important part of the k-space is scanned.
Next, we wish a good choice of the parameter n which determines the radial sampling rate of the spiral. A lower bound for n can be found considering the next argument.
To avoid aliasing along the radial direction , the sample frequency (along this direction) should match the Nyquist criterion:

$$L = \frac{1}{\Delta k} = \frac{2n}{2k_{\max}} = 2n\Delta r$$

where L is the distance of the first aliasing point to the center (spatial domain), Δk the distance between adjacent spiral interleaves (taken along the radial direction), Δr the spatial resolution for the magnetization and $k_{\max}$ the maximum frequency obtained by the Discrete Fourier Transform of $M_\perp$. See figure 2.7 for a graphical explanation of the symbols used.

Furthermore, we used the fact that $\Delta r = 1/2k_{\max}$ (Nyquist condition) and setting $A = k_{\max}$ we have an expression for the minimum number of spiral interleaves for this special case.
We can conclude that, for $n = L/2\Delta r$ the distance from the center to the first alias point should be L. Note that this fact actually holds only for the positive x direction. Along the other radial directions we have $k_{\max} < A$ and therefore the aliasing should occur at a smaller distance, following a spiral

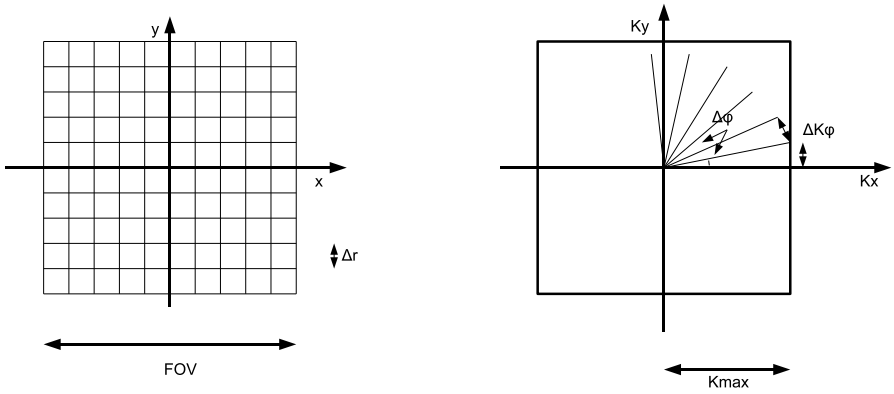

Figure 2.7: Graphical explanation of the symbols: discretized space domain (left) and k-space scanned following a constant angular rate spiral trajectory (right).

pattern.

For the sampling frequency along the tangent direction we can follow a similar reasoning: set Δk_φ the maximal distance between two points of the spiral trajectory, then:

$$\Delta k_\varphi \approx k_{\max} \Delta\varphi$$

where $\Delta\varphi$ denotes the angular sampling interval, i.e.:

$$\Delta\varphi = \frac{2\pi n \Delta t}{T}$$

with Δt the sampling interval in time. Denote $N_t = T/\Delta t$ the number of sampling points in time, then:

$$\Delta k_\varphi \approx k_{\max} \frac{2\pi n}{N_t}.$$

According to the Nyquist criterion:

$$\Delta k_\varphi = \frac{1}{L}.$$

Making again use of the relation $k_{\max} = 1/2\Delta r$ we can conclude

$$N_t \approx 2\pi n k_{\max} L = \frac{\pi}{2} \left(\frac{L}{\Delta r} \right)^2 = \frac{\pi}{2} N_s^2$$

where $N_s = L/\Delta r$ denotes the number of sampling points (space domain) along one dimension (here we assume it is the same for both dimensions).
The above expression for N_t gives us an estimate of the number of time sample points needed for a spiral trajectory in order to avoid longitudinal aliasing. The estimate is based on the outer part of the trajectory, i.e. when the longitudinal steps are largest. It is clear that approaching the center of the k-space the trajectory will oversample the k-space, resulting in a great number of superfluous points and a much longer RF pulse than actually needed. Also for this reason we see that the constant angular rate spiral trajectory does not offer an efficient way to scan the k-space. Optimization of k-space trajectory under a number of constraints will be addressed at a later stage.

2.3 Numerical Experiments

We can now run some simulation to validate the discussion in the previous sections. We will investigate the dependence between the error in the obtained magnetization profile and the parameters A, N_t and n. The desired magnetization profile will be a Gaussian (formula 2.9) centered at the origin of the spatial domain $[-12, 12] \times [-12, 12]$ cm^2, thus FOV $= 24$. . The number of points along one space dimension is $N_s = 32$ resulting in a spatial resolution $\Delta r = 0.77$ cm. The flip angle at the center is required to be $\theta = 10^o$ and the magnetization should have only a y component ($M_x = 0$ everywhere, thus $M_\perp = iM_y$). We take therefore $\mu_1 = i \sin 10^o = 0.1736i$. With $\mu_2 = 0.8$ the profile is sharply selective (see figure 2.8). The function W (i.e. the Fourier transform of the magnetization) is a Gaussian (see figure 2.9).

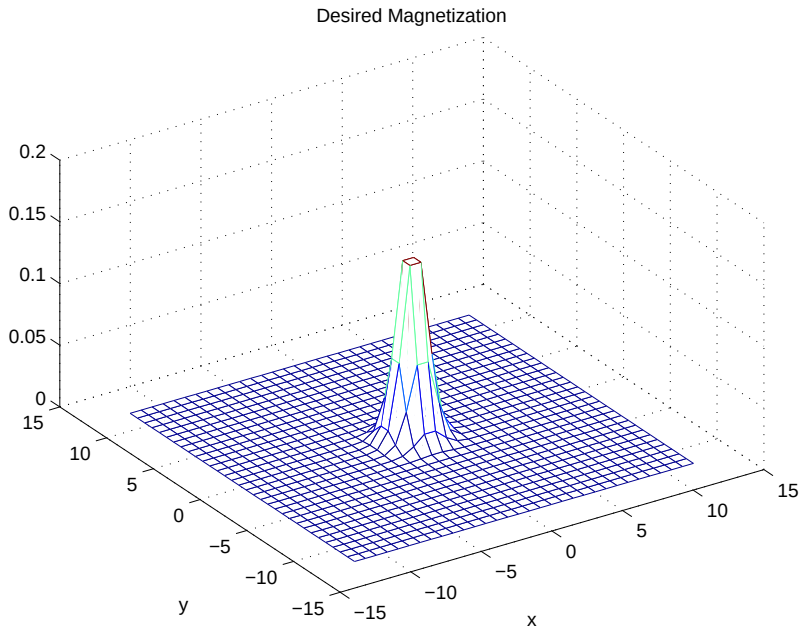

Figure 2.8: Magnetization profile for a 10^o degrees flip angle at the origin. Only the M_y component is shown since $M_x = 0$ everywhere.

For the computations, Equation (2.10) must be discretized. We set $\Delta t = 0.025$ millisec. (this depends on the hardware) and discretize t with this time step ($t_n = n\Delta t$). After having computed the $B_1(t_n)$ for $n = 0 \ldots N_t - 1$ we compute the integral of 2.4 and check the resulting $M_\perp = M_x + iM_y$. Also, we run a Bloch Equation Simulator that, given $\vec{G}$ and B_1, simulate the rotation

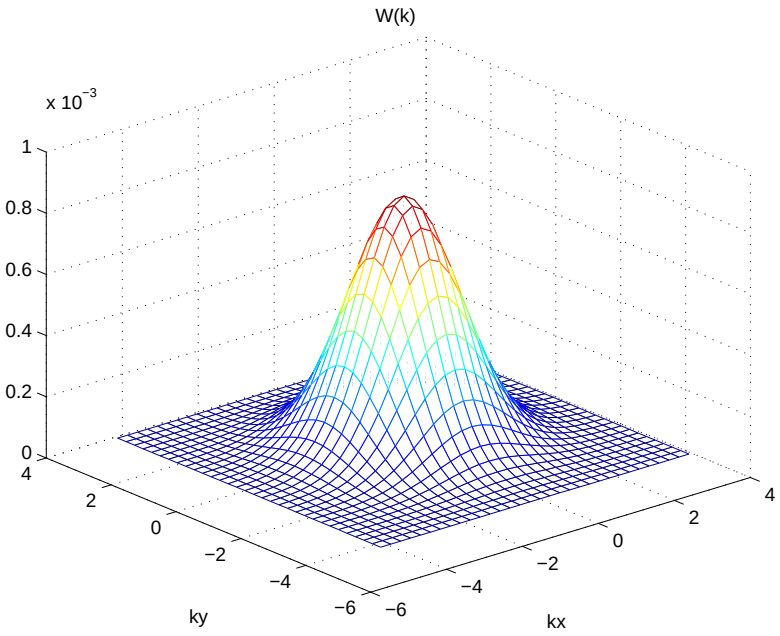

Figure 2.9: $W(\vec{k})$ for the magnetization profile of figure 2.8.

of $\vec{M}$ by means of rotation matrices: for each time step, t_n, a rotation matrix (dependent on $B_1(t_n)$) is computed and applied to $\vec{M}(t_{n-1})$. In this way a realistic representation of the whole process can be given, even for higher flip angles, when formula (2.4) does not longer hold. An explanation about how the numerical simulator works is reported in the appendix.
We will denote by M_i and M_s the profiles obtained by integration and by Bloch simulation respectively. Furthermore we will consider the following errors:

- E_x: the error relative to the x component and scaled by the maximum value of $M_\perp$ i.e. $|\mu_1|$:

$$E_x \equiv |\mathrm{Re}(M_\perp - M)|/\mu_1$$

- E_y: the error relative to the y component:

$$E_y \equiv |\mathrm{Im}(M_\perp - M)|/\mu_1$$

- E_{abs}: the error relative to the Absolute value:

$$E_{\mathrm{abs}} \equiv |\mathrm{abs}(M_\perp) - \mathrm{abs}(M)|/\mu_1$$

where M denotes either M_i or M_s.

Experiment 1

In the first experiment we respect the Nyquist criterions (radial and longitudinal) described above, i.e.:

$$\begin{aligned} n &= \frac{L}{2\Delta r} \\ N_t &= \frac{\pi}{2} N_s^2 \end{aligned}$$

with $L = 12$ cm and $A = k_{\max}$.
The obtained profile should not show alias effects within the circle of radius L. The Magnetization obtained by the Bloch Simulator, M_s, is displayed in figure 2.10.

Note the light (spiral) ringing in the M_y component at distance L tot the

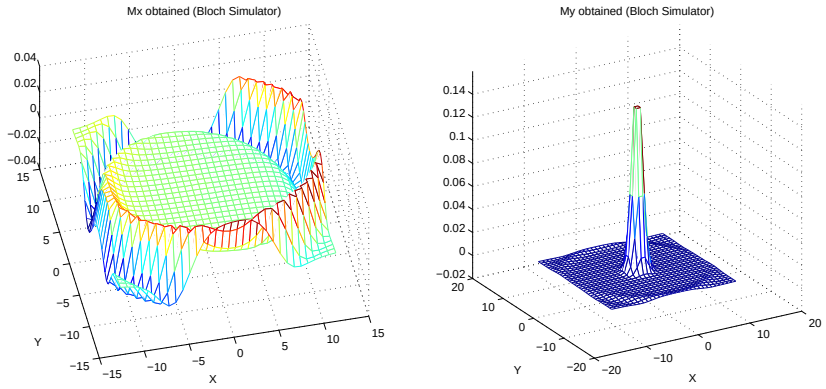

Figure 2.10: Simulated Magnetization M_x (left) and M_y (right) for Experiment 1.

center and the same , but more evident, in the M_x component (in this case the distance to the center is a bit smaller, about 10 cm). Within the regions delimited by these rings, a good reconstruction of the desired magnetization is achieved (See Figure 2.11 for a picture of E_{abs} relative to M_s within the circle of radius L). The values of the errors are reported in Table 2.1.

Profile	$\|E_x\|_2$	$\|E_y\|_2$	$\|E_{\text{abs}}\|_2$	$\|E_x\|_\infty$	$\|E_y\|_\infty$	$\|E_{\text{abs}}\|_\infty$
M_i	0.3497	0.1237	0.3709	0.0532	0.0081	0.0534
M_s	0.3484	0.1250	0.3701	0.0529	0.0084	0.0532

Table 2.1: Errors for Experiment 1. The errors are evaluated inside the circular area of radius L.

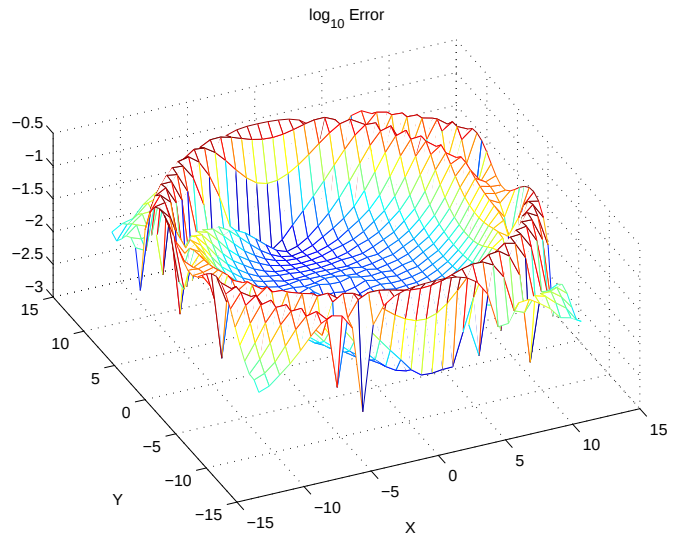

Figure 2.11: $\log_{10} E_{\text{abs}}$ for M_i (Experiment 1).

Since for practical reasons we are interested in small local errors, the supremum norm ($\|\cdot\|_\infty$) is a good measure for the quality of the obtained magnetization profile. Looking at table 2.1 we see that the supremum norm of the error is smaller then the L_2-norm ($\|\cdot\|_2$). This means that the error is locally very small over the whole region of interest (ROI) and we can conclude that for our scope the achieved accuracy is good enough.

Experiment 2

What if we choose, in the previous experiment, $A = 2k_{\max}$? The spiral would start from a further point from the origin and it would spend a long time scanning the k-space where the Fourier coefficients have negligible magnitude. Furthermore, maintaining the same number of spiral interleaves (n), this would result in a radial undersampling in the area scanned by the previous case ($A = k_{\max}$).
We first run the test for $A = 2k_{\max}$ and $n = n_1$, after that we set $A = k_{\max}$ and $n = n_1/2$ (n_1 is the previous, Nyquist value for n from Experiment 1). We expect an aliasing effect occurring at $L/2$ for both cases.
Figure 2.12 and 2.13 show the resulting M_s for $A = 2k_{\max}$ and $n = n_1/2$ respectively. Note that the resulting M_s is in both very similar: aliasing effects (with spiral profile) occur at distance of about $L/2$ in the x component. Also, for $A = 2k_{\max}$, the resulting $B_1(t)$ is plotted. Note that $B_1(t) \approx 0$ for $t < 4$: the scan is indeed not efficient.

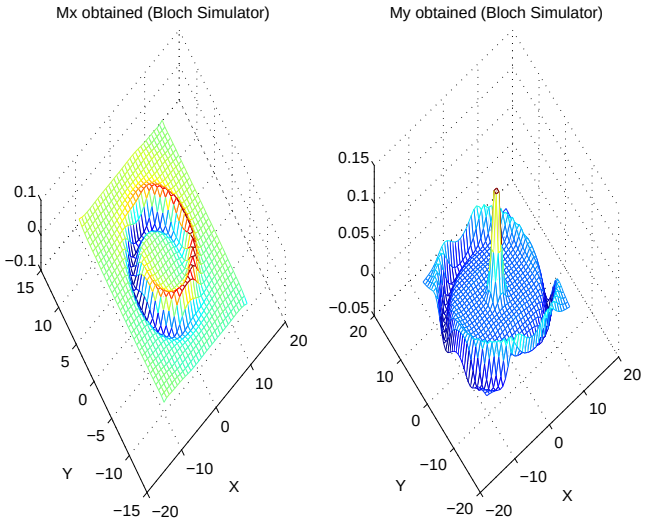

Figure 2.12: M_s for $A = 2k_{\max}$ and $n = n_1$ (Experiment 2).

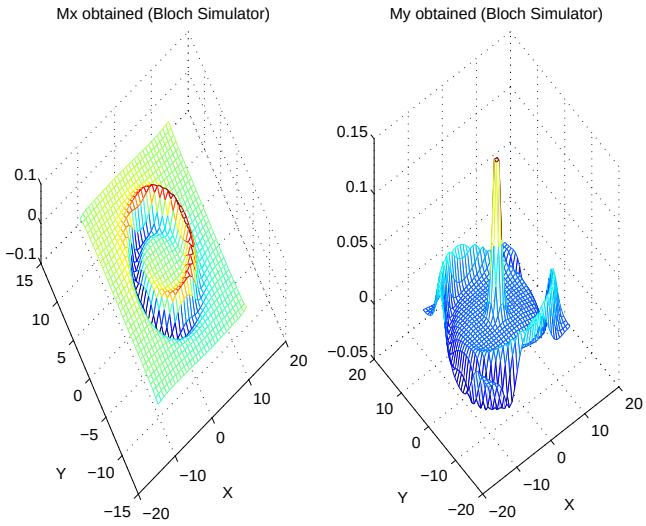

Figure 2.13: M_s for $A = k_{\max}$ and $n = n_1/2$ (Experiment 2).

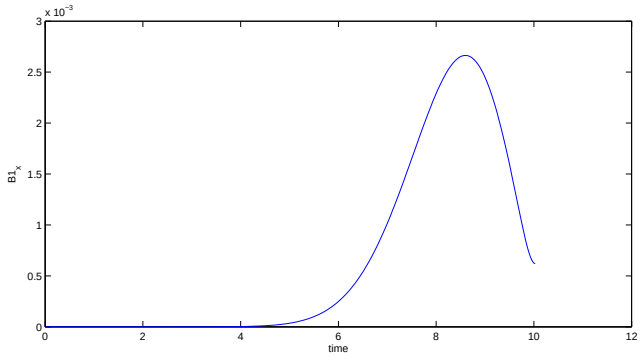

Figure 2.14: $B_1(t)$ for $A = 2k_{\max}$ (Experiment 2).

Experiment 3

We will now investigate the effects of scanning the k-space with fewer sample point then required by the Nyquist criterion along the longitudinal direction, that is: $N_t < N_{t,1} \equiv \frac{\pi}{2} N_s^2$.
We use the same settings of experiment 1 but we now take $N_t = N_{t,1}/2$. We expect the reconstructed profile suffers from aliasing along the longitudinal direction. Figure 2.15 confirms our prediction: the aliasing is evident especially in the y component.
The effects of reducing N_t are worsened if we take $N_t = N_{t,1}/10$ (see Figure 2.16).

Experiment 4

As a last test we investigate the behavior of the magnetization obtained by the Bloch Simulator (M_s) for large flip angles. Scaling $B_1(T)$ properly we are able to achieve a 90^0 flip angle excitation that retains the desired Gaussian profile (see Figure 2.17 and Table 2.2).

Profile	$\|E_x\|_2$	$\|E_y\|_2$	$\|E_{\text{abs}}\|_2$	$\|E_x\|_\infty$	$\|E_y\|_\infty$	$\|E_{\text{abs}}\|_\infty$
M_s	0.4180	0.2674	0.4962	0.0634	0.0670	0.0670

Table 2.2: Errors for Experiment 4. The errors are evaluated inside the circular area of radius 10 cm.

From Table 2.2 we see that the maximal local error is still small, and we can conclude that indeed, even for large flip angles (in this case 90^0) formula 2.4 can be applied to obtain an accurate magnetization profile.
This fact is rather important for practical reasons: increasing the flip angle,

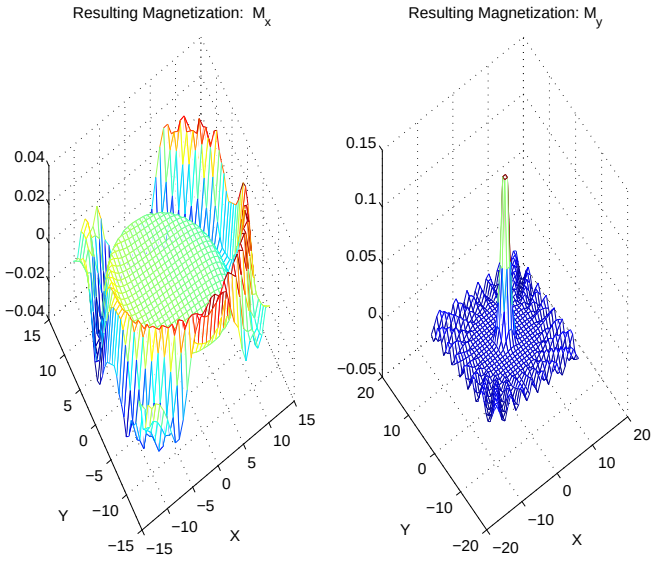

Figure 2.15: M_i for $N_t = N_{t,1}/2$ (Experiment 3).

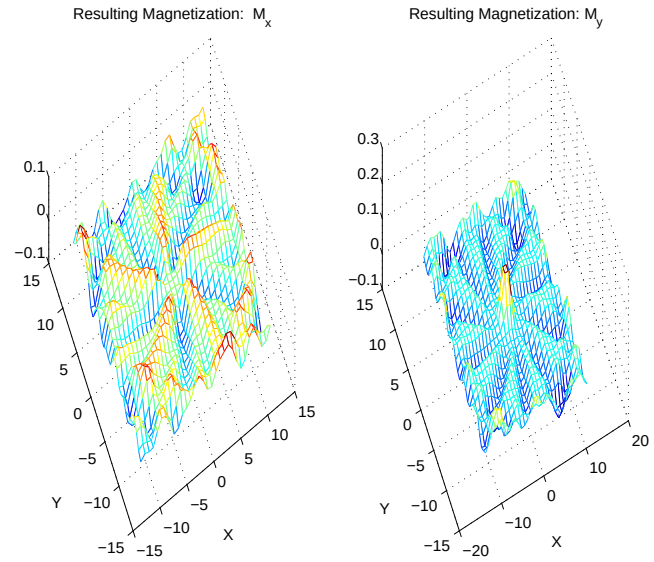

Figure 2.16: M_i for $N_t = N_{t,1}/10$ (Experiment 3).

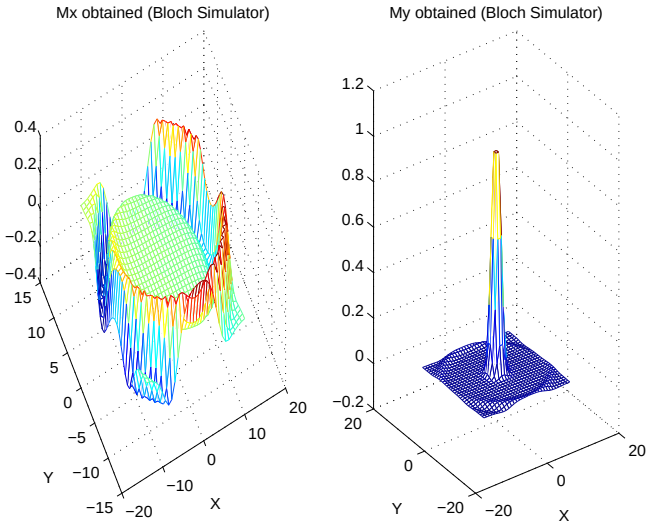

Figure 2.17: M_s for 90^o flip angle (Experiment 4).

the ratio between the signal amplitude and respective noise in measurements (*Signal to Noise Ratio*, SNR) varies, making thus possible to obtain better accuracy in the imaging process.

So far we have focused on an ideal situation, that is: the B_1 field produced by the transmitting coils is perfectly homogeneous over the whole ROI. Unfortunately, this is not the case in real-life transmit systems and the inhomogeneities can cause sever distortion in the excitation patter. Especially in high field MRI this is a serious problem. Furthermore, we are interested to shorten the scanning time of the k-space (again, for practical reasons). The solution to these problems will be the subject of the next chapter.

Chapter 3

Parallel Transmit Systems

The spatially selective excitation has been understood and a mathematical model has been designed for magnetization profiles at low flip angles regime. Now we will address the problem of shortening the excitation time.
In the previous chapter we assumed that the magnetic field caused by the RF coil were perfectly homogeneous. For high field MRI such as 3T or 7T these inhomogeneities can not be neglected. Higher magnetic fields are characterized by shorter wavelengths whose dimension is comparable to that of the human body. This causes severe distortions in the field inside the body. The resulting inhomogeneous magnetic field B_1 will be a spatially weighted version of the magnetic field at the source (b_1):

$$B_1(\vec{r}) = S(\vec{r})b_1$$

where S is the sensitivity map (also referred to as B_1 map) of the RF coil. The sensitivity map must be taken into account for an accurate study of excitation pulses.
At this point a new problem arises that is, how to determine S.Several methods are being employed at this moment (see [9], [10] and [11]). In the present work we will make use of B_1 maps obtained following the method described in [9] (see the article for a description of the procedure).
As we will see in the following sections, the inhomogeneities characterizing the RF fields in high field MRI have a fundamental beneficial effect on image reconstruction techniques involving accelerated k-space scanning. In particular, we will study an important case: the parallel imaging and transmit SENSE method.

3.1 SENSE

3.1.1 Parallel Imaging in MRI using Multiple Coils

A new approach to imaging (called SENSE) was presented in [8]: the underlying idea was that of shortening the scanning time by undersampling the k-space. In conventional Fourier Imaging this would lead to alias effects in the reconstructed image. Using multiple receiving coils, each with a different sensitivity profile, it is possible to recover the true image values at the right spatial position. Here follows a short explanation of the mathematical principles which are involved in the process.
Suppose a discrete signal (f_n) with $n \in [0, N-1]$ (figure 3.1a) is Discrete Fourier transformed to (F_k) (figure 3.1b). Of course, by inverse Discrete Fourier Transform (IDFT) of (F_k) it is possible to recover exactly the original signal (f_n). If we would apply IDFT to, say, just the even coefficients of (F_k) (i.e. to (F_m) with $m \in [0, 2, 4, \ldots, N/2-1]$) a *fold over* effect would influence the reconstructed signal $(\tilde{f}_n)$:

$$\tilde{f}_n = f_n + f_{n+N/2} \quad \text{with} \quad n \in [0, N/2-1].$$

In Figure 3.1c and 3.1d are plotted the IDFT of the undersampled (F_k) and the over-folded sample $(\tilde{f}_n)$ respectively: the two graphs are equal (note that these two samples are obviously twice as short as the original sample).

For the same reason, undersampling of the k-space by skipping the odd coefficients along one direction (the same effect can be generalized to more dimensions) would result in an aliased image (see figure 3.2). The resulting (reduced) aliased image is a superposition of pixel values from the original, full image.

Recovering of the true image values from the aliased image is possible if multiple receive RF coils are simultaneously employed, each of them with a distinct sensitivity profile. As we will see below, the differences between the individual sensitivity profiles make it possible to separate the signal contributions to each pixel from the individual coils and to bring back the aliased pixels to the original position (unfolding). Recall from equation (1.19) that the signal measured by a receive coil in standard MRI is the Fourier Transform of the spin density:

$$D(\vec{k}) = \int f(\vec{r}) e^{-i2\pi \vec{k}\cdot\vec{r}} d\vec{r} \tag{3.1}$$

where we denote the signal by D and the density (image function) by f for notation reasons.

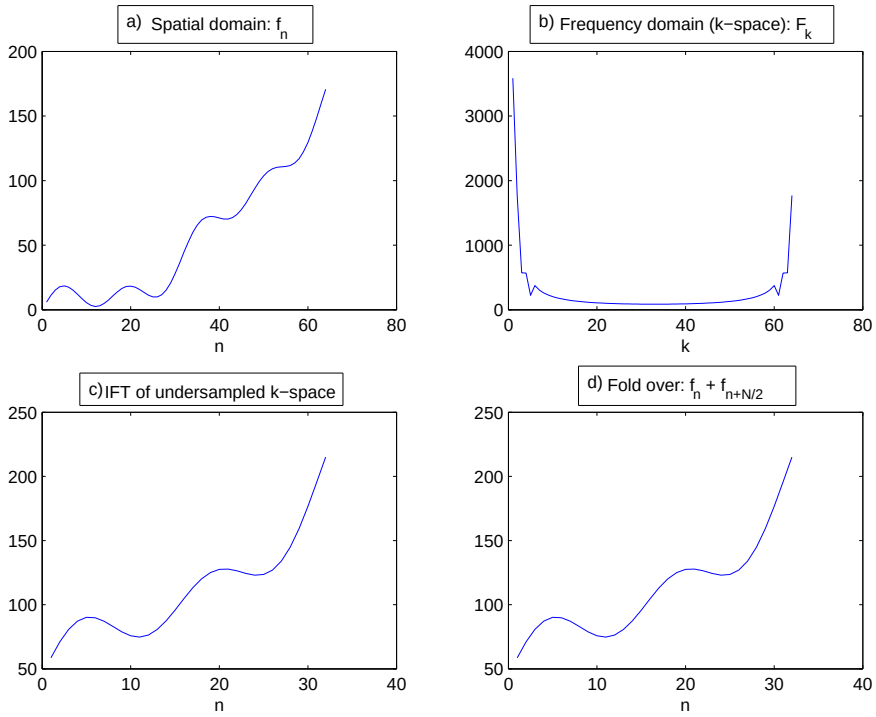

Figure 3.1: Undersampling of a one dimensional k-space. a): a sample f_n with $n \in [0, N-1]$ and $N = 64$; b): corresponding Fourier Transform F_k ($k \in [0, N]$); c): Inverse Discrete Fourier Transform of F_m with $m \in [0, 2, 4, \ldots, N/2 - 1]$ obtained by undersampling of the k-space; d) superposition (fold over) of f_n and $f_{n+N/2}$. The samples in c) and d) are obviously twice as short as the original sample.

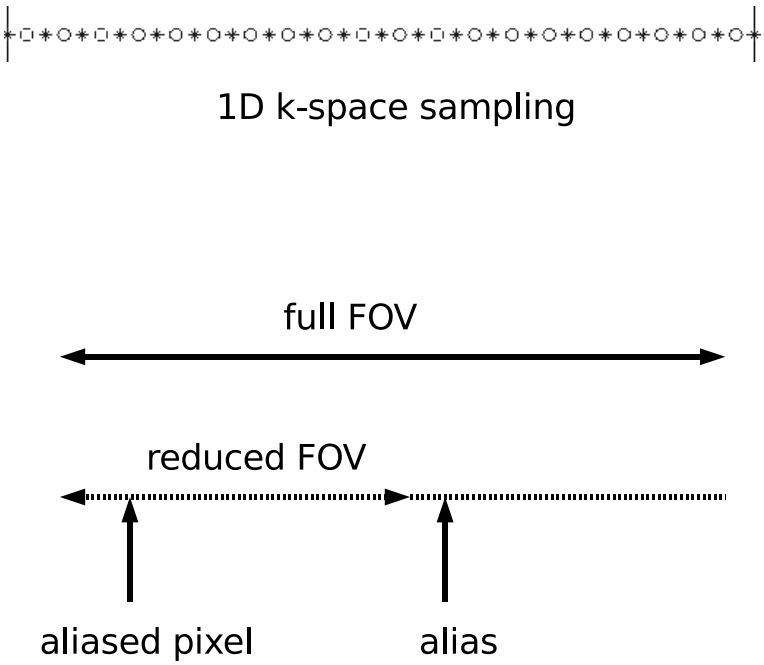

Figure 3.2: Undersampling of a one dimensional k-space. The asterisks and the circles denote the sampled and skipped points respectively during k-space scanning. This results in a reduction (by factor 2) of the FOV. An image values $\tilde{f}_n$ from the reduced FOV is the superposition of the true image value f_n and the alias $f_{n+N/2}$.

The Fourier Transform of the standard Fourier encoding function $\vec{r} \rightsquigarrow e^{-i2\pi\vec{k}\cdot\vec{r}}$ is a Dirac peak at $\vec{k}$. This reflects the fact that the encoding operation is equivalent to sampling the Fourier transform of $f(\vec{r})$ at this frequency position [20]. When multiple coils are used, we obtain for each p-th coil a corresponding signal D_p. Introducing the coil sensitivity s_p in equation (3.1) we can rewrite it as

$$D_p(\vec{k}) = \int f(\vec{r}) s_p(\vec{r}) e^{-i2\pi\vec{k}\cdot\vec{r}} d\vec{r}.$$

for $1 \leq p \leq P$ with P the number of coils employed.
In parallel MRI, the function $\vec{r} \rightsquigarrow s_p(\vec{r})e^{-i2\pi\vec{k}\cdot\vec{r}}$ is considered as a new, hybrid, encoding function. According to the sensitivity profiles of the coils, the hybrid encoding functions are no longer plane waves but show a more irregular profile, resulting in a distinct shape with a significant extent in the k-space representation, that is: the Fourier Transform of $s_p(\vec{r})e^{-i2\pi\vec{k}\cdot\vec{r}}$ has significant magnitude over an extended region of the k-space. Following this interpretation, the k-space encoding is no longer a pure sampling but rather a weighted integral of data from a certain "neighborhood' in the k-space [20]. Intuitively we could state that the hybrid encoding collects informations from the whole neighborhood, not only from a single sample point. We can hope that if we employ enough coils and the sensitivity spectrum (the Fourier transform of the sensitivity) is large enough, the information from the whole neighborhood can be recovered [19].

Let $\mathcal{F}$ be the Fourier Transform operator, $\mathbb{K}$ the k-space (either $\mathbb{R}$, $\mathbb{R}^2$ or $\mathbb{R}^3$) and $\mathbb{A}$ the subset of k-space which is scanned by a single coil. Making use of the convolution theorem:

$$\begin{aligned} D_p(\vec{k}) &= \int s_p(\vec{r}) f(\vec{r}) e^{-i2\pi\vec{k}\cdot\vec{r}} d\vec{r} = \mathcal{F}(s_p f(\vec{r})) = [\mathcal{F}(s_p) * \mathcal{F}(f)](\vec{k}) \\ &= \int_{\vec{k}' \in \mathbb{K}} S_p(\vec{k} - \vec{k}') F(\vec{k}') d\vec{k}' \end{aligned}$$

where $S_p(\vec{k}) = \mathcal{F}(s_p)(\vec{k})$ and $F(\vec{k}) = \mathcal{F}(f)(\vec{r})$. Discretizing the expression above we can write

$$D_{p,k} = \sum_{k' \in K} S_{p,k-k'} F_{k'} = [S_p * F]_k \quad \text{for} \quad k \in A \tag{3.2}$$

where K and A denote the bounded, discretized versions of $\mathbb{K}$ and $\mathbb{A}$ respectively. Set $N_K \equiv |K|$ and $N_t \equiv |A|$. The number of elements of A is denoted by N_t because it represents the number of sample points required by the (shortened) k-space trajectory, that is: the length of the Gradient and RF

pulses. We are interested in taking $N_t < N_K$ and N_t as small as possible (i.e. undersampling of k-space and thus shortening the scanning time) without the reconstructed image being affected by aliasing. The ratio N_K/N_t is also called reduction factor.
Looking at the expression (3.2) we may argue whether it is well defined, that is, whether $S_{p,k-k'}$ exists: in a standard Fourier Transform this would not be a problem, but in the more general context of non cartesian trajectories we should pay attention to the case that $k - k' \notin A$. However the issue does not arise in applications and the validity of the method is ensured by the positive results obtained.
Eq. (3.2) can expressed in matrix notation as

$$\mathbf{D}_p = \mathbf{S}_p\mathbf{F}$$

where $\mathbf{D}_p$ is a N_t dimension vector, $\mathbf{S}_p$ a $N_t \times N_K$ dimension matrix and $\mathbf{F}$ a N_K dimension vector (the unknown).
Putting the data from all coils together we obtain

$$\mathbf{SF} = \mathbf{D} \tag{3.3}$$

where we used the concatenations

$$\mathbf{S} = \begin{bmatrix} \mathbf{S_1} \\ \mathbf{S_2} \\ \dots \\ \mathbf{S_P} \end{bmatrix}$$

and

$$\mathbf{D} = \begin{bmatrix} \mathbf{D_1} \\ \mathbf{D_2} \\ \dots \\ \mathbf{D_P} \end{bmatrix}$$

In case the solution of (3.3) is possible (this depends on the characteristics of $\mathbf{S}$ and hence on the sensitivity spectra), we obtain the vector

$$\mathbf{F} = (\mathbf{S}^H\mathbf{S})^{-1}\mathbf{S}^H\mathbf{D}$$

whose Inverse Fourier Transform is the desired image function.

Numerical Note

The method we followed in the above description of parallel imaging is referred to as k-space approach. Equivalently, there is also an image-space

formulation of the problem. One major advantage of the k-space approach is that the matrix $\mathbf{S}$, is often *sparse* that is, most of its entries are zeros (or, more precisely speaking, *almost* zero: in this case the smallest entries could be discarded and substituted by zeros). This follows from the fact that the hybrid encoding functions are smooth and have often a large extent in the image domain: their k-space extent will be, in general, much more compact. The sparsity of $\mathbf{S}$ has a fundamental importance since its dimensions tend to be large. For instance: a cartesian discretization of the image domain by 128 points in both directions implies that $N_K = 128^2$ and by a 4-fold undersampling with 8 coils $PN_t = 8 \cdot 128^2/4$. It follows that $\mathbf{S}$ has 32768 rows and 16384 columns. Rather than inverting $\mathbf{S}$, iterative methods can be applied for the solution of (3.3) with greater efficiency and stability.

3.1.2 Transmit SENSE

The idea of parallel imaging can be adapted to the transmission of spatially selective multidimensional RF pulses. The use of multiple coils allows us to undersample the k-space without loosing accuracy in the obtained magnetization.
The parallel transmit systems have thus the advantage to require shorter pulses.
We will focus on the Transmit SENSE system as described for the first time in [12].
Suppose we have P coils which can send an excitation pulse independently from each other, that is, P independent and simultaneous RF-waveforms $B_{1,p}(t)$ with $0 \leq p < P$. Also, suppose the sensitivity profile $S_p(\vec{r})$ of each p-th coil is known. The resulting RF will be the weighted superposition of the individual waveforms:

$$B_1(\vec{r}, t) = \sum_{p=0}^{P-1} S_p(\vec{r}) B_{1,p}(t)$$

Substituting in (2.4) we obtain:

$$M_\perp(\vec{r}, T) = i\gamma M_0 \sum_{p=1}^{P} \left(S_p(\vec{r}) \int_0^T B_{1,p}(t) e^{i\vec{r}\cdot\vec{k}(t)} dt \right). \tag{3.4}$$

To find a numerical solution for the P requested pulses, we discretize eq. (3.4) and we obtain

$$\mathbf{Ax} = \mathbf{b}$$

where

- $\mathbf{b}$ is the discretized desired magnetization on the spatial grid $N_s \times N_s$,
- $\mathbf{A} = [\mathbf{S}_1\mathbf{F} \quad \mathbf{S}_2\mathbf{F} \ldots \mathbf{S}_P\mathbf{F}]$ i.e. a concatenation of matrices
- $\mathbf{S}_p$ is diagonal and contains the spatial weights $S_p(\vec{r})$
- $\mathbf{F}(m,n) = i\gamma M_0 \Delta t e^{i\vec{r}_m \cdot \vec{k}_n}$ with $1 \leq m \leq N_s^2$ and $1 \leq n \leq N_t$
- Δt is the sampling interval in time.
- $$\mathbf{x} = \begin{bmatrix} \mathbf{B_{1,1}} \\ \mathbf{B_{1,2}} \\ \cdots \\ \mathbf{B_{1,P}} \end{bmatrix}$$
  is the concatenation of the requested RF pulses.

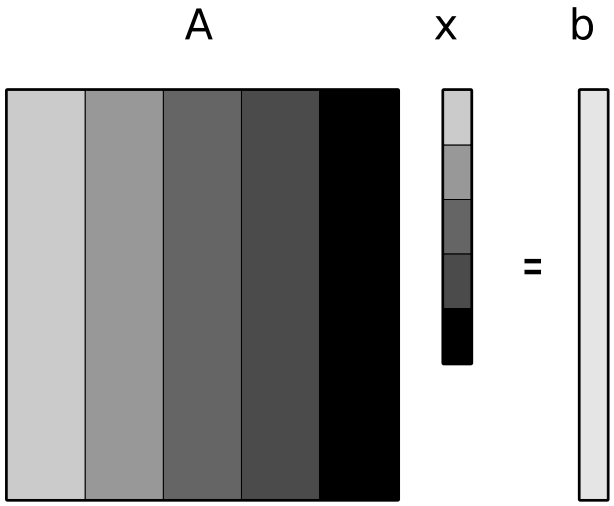

Figure 3.3: The structure of $\mathbf{A}$, $\mathbf{x}$ and $\mathbf{b}$. In this particular case $P = 5$ and the sub-matrices $\mathbf{S}_p\mathbf{F}$ have each a different colour as the five corresponding RF pulses from the vector $\mathbf{x}$

Note that $\mathbf{A}$ is a $N_s^2 \times PN_t$ matrix (N_t is the number of sample points in time, which means that $N_t\Delta t$ is the total pulse length). (See figure 3.3)

Correcting the main field inhomogeneities

In high field MRI, also the B_0 static magnetic field suffers from inhomogeneities. In this case we speak of *off resonance* since the proton spins do not precess with the same frequency. Given the main field inhomogeneity map $\Delta B_0(\vec{r})$, equation (2.2) becomes:

$$\frac{d\vec{M}}{dt} = \begin{pmatrix} 0 & \gamma(\vec{G}\cdot\vec{r}+\Delta B_0) & -\gamma B_{1,y} \\ -\gamma(\vec{G}\cdot\vec{r}+\Delta B_0) & 0 & \gamma B_{1,x} \\ \gamma B_{1,y} & -\gamma B_{1,x} & 0 \end{pmatrix} \begin{pmatrix} M_x \\ M_y \\ M_z \end{pmatrix} \tag{3.5}$$

and equation (3.4) takes the off-resonance form:

$$M_\perp(\vec{r},T) = i\gamma M_0 \sum_{p=1}^{P} \left(S_p(\vec{r}) \int_0^T B_{1,p}(t) e^{i\gamma\Delta B_0(\vec{r})(t-T)} e^{i\vec{r}\cdot\vec{k}(t)} dt \right).$$

The above discretization can be easily adapted to the more general case of a distorted B_0 field. In the present work we will focus only on the B_1 inhomogeneities since these cause the main problems in MRI. Including the off-resonance term $e^{i\gamma\Delta B_0(\vec{r})(t-T)}$ in the following work is straightforward and do not require additional mathematical treatments.

3.2 Regularized Least Square Problems

The original Integral Equation (3.4) is now reduced to the linear system $\mathbf{Ax} = \mathbf{b}$ which has to be solved in a least square sense, i.e., find

$$\text{argmin}_x \left(\|\mathbf{Ax} - \mathbf{b}\|_2^2 \right). \tag{3.6}$$

In general, A will be ill-conditioned, i.e. it will have a large condition number. As a consequence, small perturbations in the vector $\mathbf{b}$ or rounding off errors in the numerical process could lead to wrong numerical solutions. However, in this case the stability of the numerical process is undermined by the errors in the matrix $\mathbf{A}$ which are consequence of the approximations regarding the k-space scan and the B_1 maps.
Suppose $\mathbf{A} \in \mathbb{C}^{n\times n}$ is a perturbed matrix, that is: $\mathbf{A} = \mathbf{A}_e + \Delta_A$, where the term Δ_A represents the perturbation caused by the above mentioned approximation steps on the "true" matrix $\mathbf{A}_e$. As it is shown in the Appendix, solving the least squares problem (3.6) is equivalent to solving the Normal Equations

$$\mathbf{A}^T\mathbf{Ax} = \mathbf{A}^T\mathbf{b}$$

that is, writing out the terms:

$$(\mathbf{A}_e + \Delta_A)^T (\mathbf{A}_e + \Delta_A)(\mathbf{x}_e + \boldsymbol{\Delta}_x) = (\mathbf{A}_e + \Delta_A)^T \mathbf{b}$$

$$\Leftrightarrow \left(\mathbf{A}_e^T\mathbf{A}_e + \Delta_A^T\mathbf{A}_e + \mathbf{A}_e^T\Delta_A + \Delta_A^T\Delta_A\right)(\mathbf{x}_e + \boldsymbol{\Delta}_x) = \mathbf{A}_e^T\mathbf{b} + \Delta_A^T\mathbf{b} \quad (3.7)$$

where $\boldsymbol{\Delta}_x$ denotes the error in the computed solution and $\mathbf{b}$ is supposed to be unperturbed (remember that in our problem, $\mathbf{b}$ represents the (discretized) desired magnetization profile, thus it is not affected by noise or other error sources).
Neglecting the terms $\Delta_A^T\Delta_A$ and $\left(\Delta_A^T\mathbf{A}_e + \mathbf{A}_e^T\Delta_A\right)\Delta_x$, Eq. (3.7) becomes

$$\mathbf{A}_e^T\mathbf{A}_e\Delta_x + \left(\mathbf{A}_e^T\mathbf{A}_e + \Delta_A^T\mathbf{A}_e + \mathbf{A}_e^T\Delta_A\right)\mathbf{x}_e = \mathbf{A}_e^T\mathbf{b} + \Delta_A^T\mathbf{b} \quad (3.8)$$

while for the true system it holds

$$\mathbf{A}_e^T\mathbf{A}_e\mathbf{x} = \mathbf{A}_e^T\mathbf{b}.$$

Subtracting the last expression to (3.8) we obtain

$$\left(\Delta_A^T\mathbf{A}_e + \mathbf{A}_e^T\Delta_A\right)\mathbf{x}_e + \mathbf{A}_e^T\mathbf{A}_e\Delta_x = \Delta_A^T\mathbf{b}$$

$$\Rightarrow \Delta_x = -\left(\mathbf{A}_e^T\mathbf{A}_e\right)^{-1}\mathbf{A}_e^T\Delta_A\mathbf{x}_e + \left(\mathbf{A}_e^T\mathbf{A}_e\right)^{-1}\Delta_A^T\left(\mathbf{b} - \mathbf{A}_e\mathbf{x}_e\right). \quad (3.9)$$

We rewrite the term $\left(\mathbf{A}_e^T\mathbf{A}_e\right)^{-1}\mathbf{A}_e^T$ after performing the QR decomposition of $\mathbf{A}_e = \mathbf{QR}$:

$$\left(\mathbf{A}_e^T\mathbf{A}_e\right)^{-1}\mathbf{A}_e^T = \mathbf{R}^{-1}\mathbf{Q}^T.$$

Then Eq. (3.9) becomes

$$\Delta_x = -\left[\mathbf{R}^{-1}\mathbf{Q}^T\Delta_A\mathbf{x}_e + \left(\mathbf{A}_e^T\mathbf{A}_e\right)^{-1}\Delta_A^T\mathbf{r}\right]$$

$$\Rightarrow \|\Delta_x\| \leq \frac{1}{\sigma_{\min}}\|\Delta_A\|\|\mathbf{x}_e\| + \|\left(\mathbf{A}_e^T\mathbf{A}_e\right)^{-1}\|\Delta_A\|\|\mathbf{r}\|$$

$$= \frac{1}{\sigma_{\min}^2}\|\Delta_A\|\|\mathbf{r}\| + \frac{1}{\sigma_{\min}}\|\Delta_A\|\|\mathbf{x}_e\|$$

where $\sigma_{\min}$ denotes the smallest singular value of $\mathbf{A}_e$ and $\mathbf{r} = \mathbf{A}_e\mathbf{x}_e - \mathbf{b}$ the residual.
If $\mathbf{b} \in \text{Rang}(\mathbf{A_e}) \Rightarrow \mathbf{r} = \mathbf{0} \Rightarrow$

$$\|\Delta_x\| \leq \frac{1}{\sigma_{\min}}\|\Delta_A\|\|\mathbf{x}_e\| = \kappa(\mathbf{A}_e)\frac{\|\Delta_A\|}{\|\mathbf{A}_e\|}\|\mathbf{x}_e\|$$

$$\Leftrightarrow \frac{\|\Delta_x\|}{\|\mathbf{x}_e\|} \leq \kappa(\mathbf{A}_e)\frac{\|\Delta_A\|}{\|\mathbf{A}_e\|}$$

which means that, in this case, the relative error $\frac{\|\mathbf{\Delta}_x\|}{\|\mathbf{x}_e\|}$ can be $\kappa(\mathbf{A}_e)$ times the relative error in $\mathbf{A}_e$, $\frac{\|\Delta_A\|}{\|\mathbf{A}_e\|}$.
If $\mathbf{b} \notin \text{Rang}(\mathbf{A_e})$ then

$$\frac{\|\Delta_x\|}{\|\mathbf{x}_e\|} \leq \frac{\|\mathbf{A}_e\|^2}{\sigma_{\min}^2}\frac{\|\Delta_A\|}{\|\mathbf{A}_e\|}\frac{\|\mathbf{r}\|}{\|\mathbf{x}_e\|\|\mathbf{A}_e\|} + \frac{\|\mathbf{A}_e\|}{\sigma_{\min}}\frac{\|\Delta_A\|}{\|\mathbf{A}_e\|}$$

$$= \kappa^2(\mathbf{A}_e)\frac{\|\Delta_A\|}{\|\mathbf{A}_e\|}\frac{\|\mathbf{A}_e\mathbf{x}_e - \mathbf{b}\|}{\|\mathbf{x}_e\|\|\mathbf{A}_e\|} + \kappa(\mathbf{A}_e)\frac{\|\Delta_A\|}{\|\mathbf{A}_e\|}$$

$$= \kappa^2(\mathbf{A}_e)\frac{\|\Delta_A\|}{\|\mathbf{A}_e\|}\frac{\|\mathbf{A}_e\mathbf{x}_e - \mathbf{b}\|}{\|\mathbf{b}\|}\frac{\|\mathbf{b}\|}{\|\mathbf{x}_e\|\|\mathbf{A}_e\|} + \kappa(\mathbf{A}_e)\frac{\|\Delta_A\|}{\|\mathbf{A}_e\|}.$$

Note that

$$\frac{\|\mathbf{A}_e\mathbf{x}_e - \mathbf{b}\|}{\|\mathbf{b}\|} = \sin\alpha$$

where α denotes the angle between $\mathbf{b}$ and the subspace spanned by the columns of $\mathbf{A}_e$, that is $\text{Rang}(\mathbf{A}_e)$. Furthermore

$$\frac{\|\mathbf{b}\|}{\|\mathbf{x}_e\|\|\mathbf{A}_e\|} \leq \frac{\|\mathbf{b}\|}{\|\mathbf{A}_e\mathbf{x}_e\|} = \frac{1}{\cos\alpha}.$$

Putting these results together we find

$$\frac{\|\Delta_x\|}{\|\mathbf{x}_e\|} \leq \kappa^2(\mathbf{A}_e)\tan\alpha\frac{\|\Delta_A\|}{\|\mathbf{A}_e\|} + \kappa(\mathbf{A}_e)\frac{\|\Delta_A\|}{\|\mathbf{A}_e\|}.$$

From the last expression we see that the relative error $\frac{\|\mathbf{\Delta}_x\|}{\|\mathbf{x}_e\|}$ can be $\kappa(\mathbf{A}_e)^2$ times the relative error in $\mathbf{A}_e$, $\frac{\|\Delta_A\|}{\|\mathbf{A}_e\|}$.
A regularization term must be added to (3.6). The regularized least squares problem becomes

$$\text{argmin}_x \left(\|\mathbf{A}\mathbf{x} - \mathbf{b}\|_2^2 + \lambda\|\mathbf{x}\|_2^2\right) \tag{3.10}$$

where λ is a real, positive parameter. Clearly, a large λ (equivalent to a large amount of regularization) favors a small solution norm at the cost of a large residual norm, while a small λ (i.e., a small amount of regularization) has the opposite effect. Also, in case the matrix $\mathbf{A}$ is derived from the First Kind Fredholm integral equation (see Formula 3.4), the regularization has the effect of filtering the high frequency components of $\mathbf{x}$: increasing λ the respective regularized solution $\mathbf{x}_\lambda$ will be smoother (see [14]).
The regularized least squares solution can be analyzed in a special way by

mean of the singular value decomposition (SVD). The SVD is useful to gain theoretical insight into the numerical process, in practice it is too expensive to compute (in terms of FLOPs needed) and other (iterative) algorithms are employed, as we will seen is section 3.3.
Let be $\mathbf{A}$ an $m \times n$ matrix, then the singular value decomposition of $\mathbf{A}$ is given by:

$$\mathbf{A} = \mathbf{U}\mathbf{\Sigma}\mathbf{V}^{\mathbf{T}},$$

where

- $\mathbf{\Sigma}$ is an $m \times n$ matrix and has the form

  $$\mathbf{\Sigma} = \begin{bmatrix} \mathbf{D} & \mathbf{0} \\ \mathbf{0} & \mathbf{0} \end{bmatrix}$$

  with $\mathbf{0}$ the zero matrix and $\mathbf{D}$ a $r \times r$ diagonal matrix whose diagonal entries σ_i are called the *singular values of* $\mathbf{A}$ and are ordered in decreasing way, that is:

  $$\sigma_1 \geq \sigma_2 \geq \cdots \geq \sigma_r > 0$$

  (r is the rank of $\mathbf{A}$)

- $\mathbf{U} = [\mathbf{u_1} \quad \mathbf{u_2} \ldots \mathbf{u_m}]$ and $\mathbf{V} = [\mathbf{v_1} \quad \mathbf{v_2} \ldots \mathbf{v_n}]$ are orthonormal matrices whose column are called the *left and right singular vectors* respectively.

The Tikhonov regularized solution can be expressed as

$$\mathbf{x}_\lambda = \sum_{i=1}^{r} f_i \frac{\mathbf{u_i}^T \mathbf{b}}{\sigma_i} \mathbf{v_i} \tag{3.11}$$

where

$$f_i = \frac{\sigma_i^2}{\sigma_i^2 + \lambda}. \tag{3.12}$$

From (3.11) and (3.12) we see that the components of $\mathbf{x}_\lambda$ relative to the smallest singular values are the most damped ones by f_i: in case $\mathbf{A}$ represents a Fredholm integral operator, the respective singular vectors are usually responsible for the higher frequency components (their elements tend to have more sign changes)[14]. Increasing λ, the filtering effect increases smoothening $\mathbf{x}_\lambda$.

3.2.1 Specific Absorption Rate

Before we proceed with the numerical solution of (3.10) we introduce an important physical quantity: the *Specific Absorption Rate* (SAR).
The RF magnetic fields induce electric fields $\vec{E_p}(\vec{r})$ on the object being scanned. The resulting total electric field $\vec{E}(\vec{r},t)$ is the superposition of the individual electric fields weighted by the RF waveform:

$$\vec{E}(\vec{r},t) = \sum_{p=1}^{P} B_{1,p}(t)\vec{E}_p(\vec{r}) \tag{3.13}$$

Any Electric field applied on a medium cause a heating of the latter. In medical applications, this heating must be constrained, for safety reasons related to the patient's health. The average energy deposition in a region of a certain mass over an extended period of time due to the application of an excitation pulse (SAR) must be kept within certain limits. The SAR per voxel is defined as [15]:

$$\mathrm{SAR}(\vec{r}) \equiv \frac{\sigma(\vec{r})}{2\rho(\vec{r})}\frac{1}{D}\int_0^D \|\vec{E}(\vec{r},t)\|_2^2 dt \approx \frac{\sigma(\vec{r})}{2D\rho(\vec{r})}\Delta t \sum_{n=0}^{N_t-1} \|\vec{E}(\vec{r},n\Delta t)\|_2^2 \tag{3.14}$$

where now σ and ρ are the object's conductivity and density respectively and D the repetition time i.e. the amount of time that exists between successive pulse sequences (thus $D \geq T$). Note the square dependence between $\mathrm{SAR}(\vec{r})$ and $\|\vec{E}\|$ and between $\mathrm{SAR}(\vec{r})$ and $\|B_1\|$.
From (3.14) it is possible to compute the 1-g Local SAR by averaging the SAR per voxel values over a 1 gram cube. From (3.14) and (3.13) it is clear that controlling through regularization the quantity $\|x\|_2^2$, has a controlling effect on $\mathrm{SAR}(\vec{r})$ as well. This useful side effect of the regularization procedure could be exploited in SAR-constrained solutions of (3.10).

3.2.2 The choice for an optimal λ value: the L-curve

To solve (3.10) we need a good choice for λ that minimizes the residual and, at the same time, guarantees us an accurate approximation to the true solution. Also, we are concerned with SAR constrains, and therefore we are interested to solution with a small euclidean norm. The idea is not to focus on a single value of λ, but, rather, to investigate how the quantities $\|\mathbf{A}\mathbf{x}^\lambda - \mathbf{b}\|_2$ and $\|\mathbf{x}^\lambda\|_2$ vary as a function of this parameter. Figure 3.4 displays a typical path obtained by varying the values of λ and plotting the corresponding residual and solution norm (after having taken the logarithm).

Because its shape reminds of a L, this plot is commonly referred to as the *L-curve*. Note that for large values of λ the regularized solution has a smaller norm (and it is strongly filtered), hence it will correspond to a point on the bottom left part of the graph. Increasing λ the path moves to the upper left corner, where the norm is larger and the filter weaker, resulting in less smooth solutions. Since we are interested in minimizing both $\|\mathbf{A}\mathbf{x}^{\lambda}-\mathbf{b}\|_2$ and

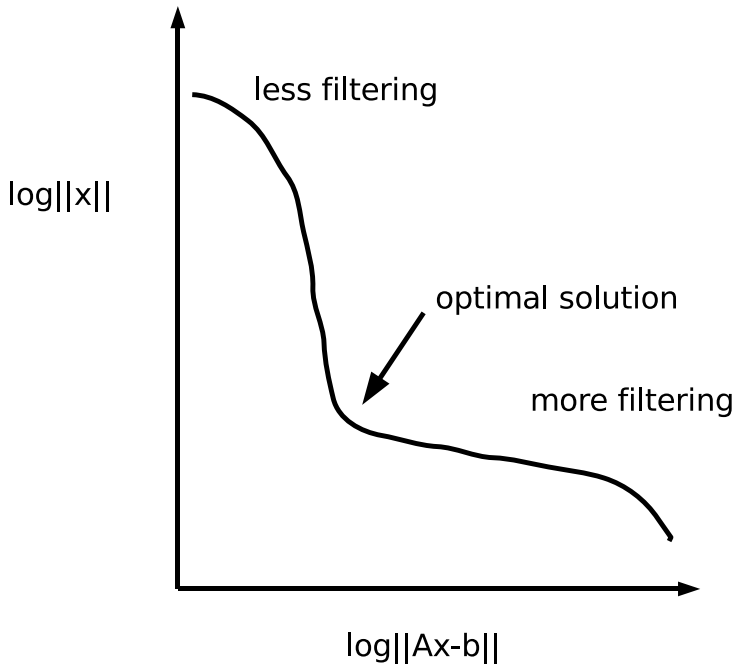

Figure 3.4: A typical L-curve.

$\|\mathbf{x}^{\lambda}\|_2$, the trade off element λ_0 should be chosen such that the corresponding point $(\log_{10}\|\mathbf{x}^{\lambda_0}\|_2, \log_{10}\|\mathbf{A}\mathbf{x}^{\lambda_0}-\mathbf{b}\|_2)$ lies on the left bottom corner of the L-curve. For this reason we will choose a range of values $\Lambda = \{\lambda_1, \lambda_2, \ldots, \lambda_S\}$, compute the corresponding $\mathbf{x}^{\lambda_i}$ with $1 \leq i \leq S$ and, after having plotted the L-curve, we will select the optimal solution $\mathbf{x}^{\lambda_0}$.

3.3 Multishift CGLS

The solution to (3.6) is given by the solution to the normal equation (see the Appendix)

$$\mathbf{A}^T\mathbf{A}\mathbf{x} = \mathbf{A}^T\mathbf{b}.$$

The method of Conjugate Gradients (CG) could be applied to this system. A modified version of CG for these Normal Equations is given by the CGLS

algorithm as reported in [16] (see Algorithm 1).

Note that in this version the residual of the least square problem $\mathbf{b} - \mathbf{Ax_j}$

Algorithm 1 CGLS

$\mathbf{z_0} = \mathbf{b}, \quad \mathbf{r_0} = \mathbf{A^T z_0}, \quad \mathbf{p_0} = \mathbf{r_0}, \quad \mathbf{x_0} = \mathbf{0}, \quad \phi_0 = \|\mathbf{r_0}\|^2$
for $j = 1, \ldots, k$ **do**
  $\mathbf{c_{j-1}} = \mathbf{Ap}_{j-1}$
  $\alpha_{j-1} = \phi_{j-1}/\|\mathbf{c}_{j-1}\|^2$
  $\mathbf{x}_j = \mathbf{x}_{j-1} + \alpha_{j-1}\mathbf{p}_{j-1}$
  $\mathbf{z}_j = \mathbf{z}_{j-1} - \alpha_{j-1}\mathbf{c}_{j-1}$
  $\mathbf{r_j} = \mathbf{A^T z_j}$
  $\phi_j = \|\mathbf{r_j}\|^2, \quad \beta_{j-1} = \phi_j/\phi_{j-1}$
  $\mathbf{p}_j = \mathbf{r}_j + \beta_{j-1}\mathbf{p}_{j-1}$
end for

(i.e. $\mathbf{z}_j$) is explicitly known in every step. Note also that CGLS requires two matrix-vector multiplications per step and the convergence speed and stability are worsened by the fact that $\kappa(\mathbf{A^T A}) = \kappa(\mathbf{A})^2$ where $\kappa(\mathbf{A})$ denotes the condition number of $\mathbf{A}$.

When the regularization is applied, solving (3.10) is equivalent to solving the shifted problem (see the Appendix)

$$(\mathbf{A}^T\mathbf{A} + \lambda\mathbf{I})\mathbf{x}^\lambda = \mathbf{A}^T\mathbf{b}. \tag{3.15}$$

The shifted version of CGLS is reported as algorithm 2.

Algorithm 2 CGLS for solving the shifted problem (3.15)

$\mathbf{z_0} = \mathbf{b}, \quad \mathbf{r_0} = \mathbf{A^T z_0}, \quad \mathbf{p_0} = \mathbf{r_0}, \quad \mathbf{x_0} = \mathbf{0}, \quad \phi_0 = \|\mathbf{r_0}\|^2$
for $j = 1, \ldots, k$ **do**
  $\mathbf{c_{j-1}} = \mathbf{Ap}_{j-1}$
  $\alpha_{j-1} = \phi_{j-1}/(\|\mathbf{c}_{j-1}\|^2 + \lambda\|\mathbf{p}_{j-1}\|^2)$
  $\mathbf{x}_j = \mathbf{x}_{j-1} + \alpha_{j-1}\mathbf{p}_{j-1}$
  $\mathbf{z}_j = \mathbf{z}_{j-1} - \alpha_{j-1}\mathbf{c}_{j-1}$
  $\mathbf{r_j} = \mathbf{A^T z_j} - \lambda\mathbf{x}_j$
  $\phi_j = \|\mathbf{r_j}\|^2, \quad \beta_{j-1} = \phi_j/\phi_{j-1}$
  $\mathbf{p}_j = \mathbf{r}_j + \beta_{j-1}\mathbf{p}_{j-1}$
end for

Since we are interested in solving (3.15) for a whole set Λ of shift-values, we will employ a multishift CGLS algorithm. The aim is to adapt algorithm

2 to find simultaneously $\mathbf{x}_k^{\lambda_i}$ for all $\lambda_i \in \Lambda$ in the k-th iteration step. The idea behind the multishift methods (see for example [17]) is to split CGLS into two parts: one part should be computed independently from λ_i , requiring thus to be computed only once, the other part should contain the update for the iterates $\mathbf{x}_k^{\lambda_i}$ and thus depending on λ_i. The splitting should be carried out in an efficient and stable way such the the computation burden in the second part (that has to be repeated for each λ_i) is minimized. In particular, the matrix-vector products should be carried out in the first, λ-independent, part. We will employ the method explained in [16].
Suppose $\hat{\mathbf{M}} = \mathbf{M} + \lambda\mathbf{I}$ where $\mathbf{M}$ is the symmetric matrix of the linear system $\mathbf{Mx} = \mathbf{b}$ and we wish to solve the system

$$\hat{\mathbf{M}}\hat{\mathbf{x}} = \hat{\mathbf{b}}.$$

If $\hat{\mathbf{r}}_0 = \mathbf{r}_0$ (this happens if $\hat{\mathbf{b}} = \mathbf{b}$ and $\hat{\mathbf{x}}_0 = \mathbf{x}_0 = \mathbf{0}$) then the Krylov subspaces $\mathcal{K}_j(\mathbf{M}, \mathbf{r}_0)$ and $\mathcal{K}_j(\hat{\mathbf{M}}, \hat{\mathbf{r}}_0)$ are the same [17]. From this fundamental property we conclude that the construction of the orthogonal basis (the Lanczos process in CG-based methods) needs to be computed only once.
In [16] it is shown that, once the Lanczos step is computed, the approximated solutions can be obtained by

$$\mathbf{x}_k^{\lambda} = \mathbf{R}_k(S_k + \lambda\mathbf{I})^{-1}e_1 \tag{3.16}$$

where

- $\mathbf{R}_k$ denotes the $n \times k$ matrix with columns $\mathbf{r}_0, \ldots, \mathbf{r}_{k-1}$
- S_k the tridiagonal matrix obtained by a modified Lanczos step (the standard tridiagonal Lanczos matrix $\mathbf{T}_k$ is related to S_k by

  $$\mathbf{T}_k = \Psi_k S_k \Psi_k^{-1}$$

  with Ψ_k diagonal matrix whose non zero elements are $\sqrt{\phi_j}$ from CGLS.
- e_1 is the first standard basis vector, i.e. $(1, 0, 0, 0, \ldots, 0)^T$

The inversion of $(S_k + \lambda\mathbf{I})$ in (3.16) can be rather unstable since the matrix S_k is ill-conditioned. In [16] an algorithm is derived that prevents the formation of S_k. The resulting mCGLS method (for $\mathbf{M} = \mathbf{A}^T\mathbf{A}$) is reported here as Algorithm 3. Note the subdivision in the two parts: the inversion part must be carried out for every $\lambda \in \Lambda$. The two matrix-vector products are both carried out in the first part. Furthermore, the norm of the residual of the shifted system (normal equations) is equal to $\|\mathbf{r}_j\|/|\lambda_j^{\lambda}| = \sqrt{\phi_j}/|\lambda_j^{\lambda}|$.

Algorithm 3 Multishift CGLS for solving the family of shifted problems of the form (3.15)

$\mathbf{z_0} = \mathbf{b}, \quad \mathbf{r_0} = \mathbf{A^T z_0}, \quad \mathbf{p_0} = \mathbf{r_0}, \quad \mathbf{x}_0^\lambda = \mathbf{0}, \quad \phi_0 = \|\mathbf{r_0}\|^2, \quad t_0^\lambda = \lambda$
for $j = 1, \ldots, k$ **do**

The Lanczos part
$\mathbf{c_{j-1}} = \mathbf{A p}_{j-1}$
$\alpha_{j-1} = \phi_{j-1}/(\|\mathbf{c}_{j-1}\|^2)$
$\mathbf{z}_j = \mathbf{z}_{j-1} - \alpha_{j-1}\mathbf{c}_{j-1}$
$\mathbf{r_j} = \mathbf{A^T z_j}$
$\phi_j = \|\mathbf{r_j}\|^2, \quad \beta_{j-1} = \phi_j/\phi_{j-1}$
$\mathbf{p}_j = \mathbf{r}_j + \beta_{j-1}\mathbf{p}_{j-1}$

The inversion part
$\ell_{j-1}^\lambda = 1 + \alpha_{j-1}t_{j-1}^\lambda, \quad t_j^\lambda = \lambda + (\beta_{j-1}/\ell_{j-1}^\lambda)t_{j-1}^\lambda, \quad \gamma_j^\lambda = \gamma_{j-1}^\lambda \ell_{j-1}^\lambda$
$\mathbf{x}_j = \mathbf{x}_{j-1} + (\alpha_{j-1}/\gamma_j^\lambda)\tilde{\mathbf{p}}_{j-1}^\lambda$
$\tilde{\mathbf{p}}_j = \mathbf{r}_j + (\beta_{j-1}/\ell_{j-1}^\lambda)\tilde{\mathbf{p}}_{j-1}^\lambda$
end for

3.4 k-space trajectories: constraints and optimization

Before we start the numerical tests relative to the parallel transmit system, we must consider (and solve) the following problem.
In the theoretical treatment of the k-space trajectories we assumed any path through the k-space could be feasible. In real-life this is not the case. There are two main physical, hardware-dependent, constraints to the design of trajectories: the maximum gradient amplitude $|\vec{G}|$ and the maximum Slew rate S which is defined as the amplitude of the gradient's first derivative

$$S(t) = \left| \frac{d\vec{G}}{dt} \right|.$$

Any k-space trajectory must therefore satisfy the constraints (remind that $\vec{G}(t) = \frac{1}{\gamma}\frac{d\vec{k}(t)}{dt}$)

$$\begin{aligned} |\vec{G}(t)| &\leq G_{\max} \\ S(t) &\leq S_{\max} \end{aligned}$$

for any $t \in \mathbb{R}$ where $G_{\max}$ and $S_{\max}$ depend on the hardware.
Given an arbitrary k-space trajectory of the form $k(t)$ ($t \in [0, T]$) we want

to develop an algorithm that computes a new trajectory which follows the path described by $k(t)$ and fulfills the two constraints. The method we used to achieve this goal is based on the following approximations (see also [18]):

$$\begin{aligned} G(t) &= \frac{1}{\gamma}\frac{dk(t)}{dt} = \frac{1}{\gamma}\frac{dk(\tau(t))}{d\tau}\frac{d\tau}{dt} \approx \frac{1}{\gamma}\left(\frac{k(\tau+\Delta\tau)-k(\tau)}{\Delta\tau}\right)\frac{\Delta\tau}{\Delta t} = \\ &= \frac{k(\tau+\Delta\tau)-k(\tau)}{\gamma\Delta t} \end{aligned}$$

Given τ_h (with $\tau_h \equiv \tau(h\Delta t)$) and $\Delta\tau_h = 0$, the idea is to iteratively increment $\Delta\tau_h$ by small steps $\Delta t/1000$ as long as $\left|\frac{k(\tau_h+\Delta\tau_h)-k(\tau_h)}{\gamma\Delta t}\right| < G_{\max}$ holds. With the obtained value for $\Delta\tau_h$ we set $\tau_{h+1} = \tau_h + \Delta\tau_h$.
Consequently we check whether the Slew rate constraint holds.
Denote $k_h \equiv k(\tau_h)$ and $S_h \equiv S(h\Delta t)$, then, similarly to the above derived approximation we can write

$$S_{h+1} \approx \frac{k_{h+1} - 2k_h + k_{h-1}}{\gamma\Delta t^2}.$$

If $|S_{h+1}| > S_{\max}$ we proceed in the opposite direction as we did in the previous step, that is, we shorten the step $\Delta\tau_h$ iteratively by small steps $0.0001\Delta t$ until the constraint is fulfilled. With the obtained value of $\Delta\tau_h$ we set $\tau_{h+1} = \tau_h + \Delta\tau_h$.
The whole process starts with $\tau_0 = 0$ and stops as soon as the distance to the center of the k-space (i.e. $|k(\tau)|$) is larger than a predetermined $k_{\max}$ (we assume here that $k_{\max}$ is the radius of the k-space region which carries the important part of the Fourier coefficients, we can neglect the values of k for which $|k| > k_{\max}$). The resulting algorithm is listed below as Algorithm 4.
Note that this procedure works for paths starting at the origin and moving outward. In case we want to follow the opposite direction (as we actually do) we just reverse the obtained trajectory (and corresponding Gradients).
A gradient coil system requires to start and to end at $G = 0$. For this reason we will add to the Gradient an initial ramp with slope $S_{\max}$ that connects the line $G = 0$ to the first value of the Gradient (in case this is non zero).

To see how the constraints affect the k-space trajectory, consider the constant angular rate spiral of the form

$$k(t) = Ate^{i2n\pi t}$$

where $k_x = \mathrm{Re}(k)$ and $k_y = \mathrm{Im}(k)$. Note that this spiral describes, unlike the previously studied one, an outward trajectory. Inverting k the trajectory becomes inward. The desired excitation pattern is again a Gaussian centered

Algorithm 4 Construction of a k-space trajectory subject to the constraints $|\vec{G}(t)| \leq G_{\max}$ and $S(t) \leq S_{\max}$

Input:

- function describing the parametrized trajectory $k(t)$
- maximum distance from the origin $k_{\max}$
- $G_{\max}, \quad S_{\max}, \quad \Delta t$

$\tau_0 = 0, \quad k_0 = 0, \quad G_0 = 0, \quad G_1 = 0, \quad S_0 = 0, \quad \text{normK} = 0$

while normK$< k_{\max}$ **do**
$\tau_h = \tau_{h-1}, \quad k_{\text{new}} = k_{h-1}, \quad G_{\text{new}} = G_{h-1}, \quad \text{normG}= 0, \quad \Delta\tau_h = 0$

Gradient Amplitude Constraint
while normG$< G_{\max}$ & $\Delta\tau_h < \Delta t$ **do**
$\Delta\tau_h = \Delta\tau_h + 0.001\Delta t$
$\tau_h = \tau_h + 0.001\Delta t$
$k_h = k_{\text{new}}, \quad G_h = G_{\text{new}}$
$k_{\text{new}} = k(\tau_h)$
$G_{\text{new}} = (k_{\text{new}} - k_{h-1})/(\gamma\Delta t)$
normG$= |G_{\text{new}}|$
end while

Slew rate Constraint
if $h > 2$ **then**
$S_{\text{new}} = (k_{h-2} - 2k_{h-1} + k_h)/\gamma\Delta t^2$
normS$=|S_{\text{new}}|$
while normS$> S_{\max}$ **do**
$\tau_h = \tau_h - 0.0001\Delta t$
$k_{\text{new}} = k(\tau_h)$
$S_{\text{new}} = (k_{h-2} - 2k_{h-1} + k_{\text{new}})/\gamma\Delta t^2$
normS$= |S_{\text{new}}|$
end while
$k_h = k_{\text{new}}, \quad S_h = S_{\text{new}}$
$G_h = (k_h - k_{h-1})/(\gamma\Delta t)$
end if
normK$= |k_h|$

end while

on the origin (figure 3.5).
Before the constrained optimization process starts, we must choose a "good" value for $k_{\max}$, that is, for the radius of the circular region in the k-space to be scanned. We determine the value of $k_{\max}$ in the following way: given the maximum absolute value of the Fourier coefficients $W(\vec{k})$ (this will be the value corresponding to $\vec{k} = (0, 0)$ and we denote it by $\max_W$) we set a threshold value $v \equiv \max_W /100$. Then we set

$$k_{\max} = \max_k \{|\vec{k}| : |W(\vec{k})| \geq v\}.$$

In this way, only the region of the k-space where $|W(\vec{k})|$ are larger then $\max_W /100$ will be scanned (in signal processing this procedure is also called *quantization*). Of course this choice of $k_{\max}$ is arbitrary but it can work very well in case Fourier coefficients become very small and their contribution to the reconstructed profile can be neglected.
The graph of the unconstrained trajectory is displayed in figure 3.6. The corresponding inverted Gradients and Slew rate are reported in figure 3.7.

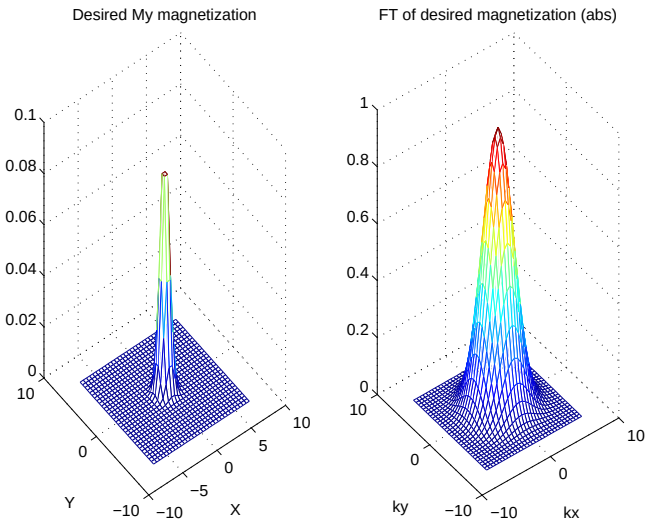

Figure 3.5: Desired Gaussian shaped excitation pattern.

We run Algorithm 4 setting

$$\begin{aligned} G_{\max} &= 3.0 \quad [\text{G/cm}] \\ S_{\max} &= 14.0 \quad [\text{G/cm/ms}]. \end{aligned}$$

The resulting constrained spiral and corresponding Gradients (with Slew rate) are plotted in figure 3.8 and 3.9 respectively. Note that the obtained

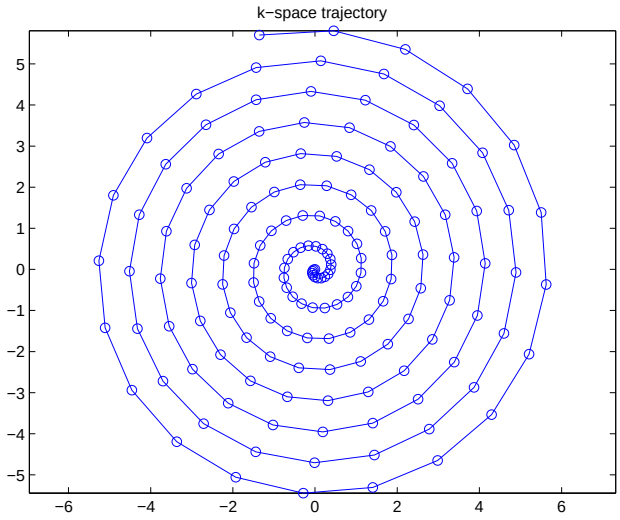

Figure 3.6: Unconstrained spiral trajectory for the desired excitation pattern.

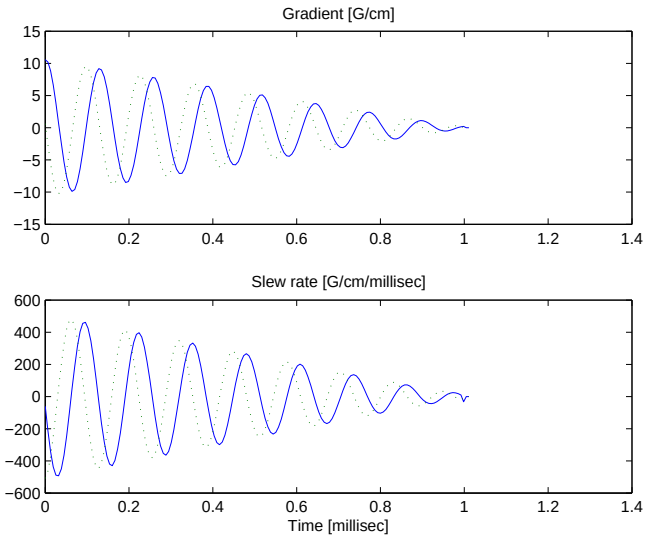

Figure 3.7: Corresponding unconstrained Gradients and Slew rate.

spiral runs constantly at the maximum Slew rate allowed, while the maximum Gradient amplitude is, in this case, never attained. Note also that, obviously, when the k-trajectory exceeds one of the two constrains, we must slow it down. This deceleration results in a longer pulse length. While for the unconstrained trajectory $N_t = 159$, for the constrained one we have $N_t = 642$.

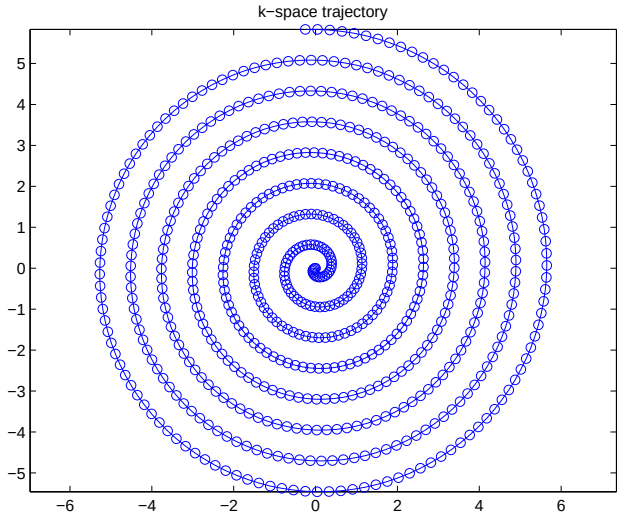

Figure 3.8: Constrained spiral trajectory for the desired excitation pattern.

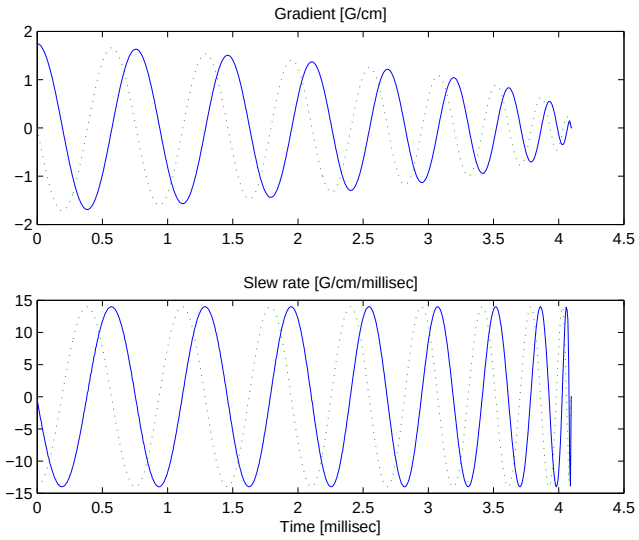

Figure 3.9: Corresponding constrained Gradients and Slew rate.

Chapter 4

Numerical Simulations and Experiment.

We can now proceed with the numerical simulations relative to the Parallel Transmit system SENSE. In particular we will study:

1. the functioning of the algorithm mCGLS for the regularized least square problem (3.10). The influence of the parameter λ on the numerical solution;

2. the effect of the sensitivity maps on the magnetization profile obtained by an undersampling of the k-space;

3. further numerical issues like a different magnetization profile, an extra regularization term and a larger spatial resolution;

4. SAR computations.

Finally, we will report the result of the first experiment on a 7 Tesla MRI scanner.

4.1 Simulation 1

Numerical Solution vs Analytical solution: effect of regularization.

The aim of the first simulation is to investigate the behavior of λ on the solution of the regularized problem (1.6). We set then $P = 1$ (that is: only one transmit channel is employed) and suppose the sensitivity profile is perfectly homogeneous (i.e. $S(\vec{r}) = 1$ for each $\vec{r} \in$ FOV).
We start with the magnetization profile given by (2.9) with $\mu_1 = 0.2$ and

$\mu_2 = 0.6$. With the same spiral k-space trajectory as given by (2.11) (unconstrained) the required RF wave form ($\mathbf{x}$) is given by formula (2.12). We will refer to $\mathbf{x}$ as analytical solution although this solution was derived by mean of approximations (see the previous chapter). The fact we dispose of a reference solution will be useful for the error analysis.
For the shift values we choose $\Lambda = \{10^4, 10^3, 10^2, \ldots, 10^{-9}, 10^{-10}\}$. After having run mCGLS we plot the L-curve. This is displayed in Figure 4.1. The analytic solution is also shown in the graph. Note that the approximations in the analytical solution and the ill-conditioning of $\mathbf{A}$ cause the relative residual norm $\|\mathbf{Ax}-\mathbf{b}\|/\|\mathbf{b}\|$ to be larger than the relative residual norm for some regularized numerical solutions. To see this, suppose $\mathbf{x} = \mathbf{x}_e + \Delta_x$ where $\mathbf{x}_e$ is the *exact solution* and Δ_x is the perturbation due to the approximation steps done to obtain $\mathbf{x}$. Then:

$$\frac{\|\mathbf{Ax}-\mathbf{b}\|}{\|\mathbf{b}\|} = \frac{\|\mathbf{A}(\mathbf{x}_e+\Delta_x)-\mathbf{b}\|}{\|\mathbf{b}\|} \leq \frac{\|\mathbf{Ax_e}\| + \|\mathbf{A}\Delta_x\| + \|\mathbf{b}\|}{\|\mathbf{b}\|}.$$

While for the exact residual holds:

$$\frac{\|\mathbf{Ax}_e-\mathbf{b}\|}{\|\mathbf{b}\|} \leq \frac{\|\mathbf{Ax_e}\| + \|\mathbf{b}\|}{\|\mathbf{b}\|}.$$

The term $\frac{\|\mathbf{A}\Delta_x\|}{\|\mathbf{b}\|}$ gives an estimate of how small perturbation in the exact solution can affect the residual. Working it out:

$$\frac{\|\mathbf{A}\Delta_x\|}{\|\mathbf{b}\|} \leq \frac{\|\mathbf{A}\|\|\Delta_x\|}{\|\mathbf{b}\|}.$$

If $\frac{\|\mathbf{A}\|}{\|\mathbf{b}\|}$ is large, small perturbations in $\mathbf{x}$ could give rise to large perturbations in the residual (in this simulation, $\frac{\|\mathbf{A}\|}{\|\mathbf{b}\|} \approx 250$).

To see how λ affects the solution $\mathbf{x}^\lambda$ we plot $|\mathbf{x}^\lambda|$ for a couple of values of λ (figure 4.2). The analytical solution has no imaginary part, hence we expect for the numerical solution the same holds. Actually $\mathbf{x}^\lambda$ does have an imaginary component (deriving presumably from rounding off errors) but this is negligible if compared with the real component (they differ by a factor in the order of 10^{-8}).

The smoothing effect of λ (more evident for larger values) is clear. Furthermore, we see that for $\lambda = 1000$ and $\lambda = 10^{-5}$ the numerical solution deviates strongly from the analytical one. We should expect that the optimal numerical solutions correspond to the corner of the L-curve, that is, for $\lambda = 0.1$ and $\lambda = 0.01$. In table (4.1) and figure 4.3 we report the relative error $\frac{\|\mathbf{x}^\lambda-\mathbf{x}\|}{\|\mathbf{x}\|}$ together with the residual $\frac{\|\mathbf{Ax}^\lambda-\mathbf{b}\|}{\|\mathbf{b}\|}$. Looking at table 4.1 and

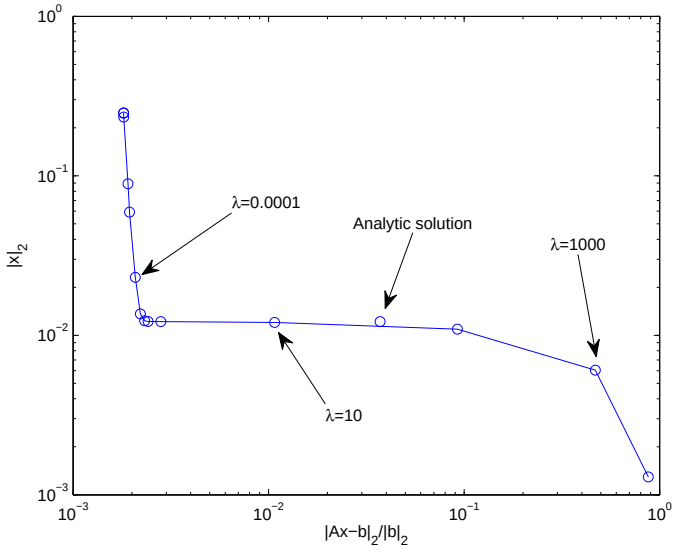

Figure 4.1: L-curve for Simulation 1. Each circle corresponds to a different value of λ. The analytic solution is also shown in the graph.

figure 4.3 we see that the best numerical solution (that one with the smallest error) corresponds to $\lambda = 10$, thus not exactly what we predicted. This can be explained by the fact that $\mathbf{x}$ is not the exact solution: the approximations made to derive it have surely a negative effect on its accuracy and hence the computation of the error in this case has only an indicative character.

Note also that this L-curve representation may not describe optimally the problem. Plotting the residual norm against the solution norm does not give a specific insight about the smoothness of $\mathbf{x}^\lambda$. In general, large values of λ guarantee smooth solutions but at cost of a low solution norm. This means that optimal numerical solutions may attain small norm but still a rather irregular profile. Compare, for example, $\mathbf{x}^{10}$ with $\mathbf{x}^{0.1}$ from Figures 4.1 and 4.2: $\mathbf{x}^{0.1}$ is closer to the sharp corner of the L-curve, therefore one may think it is the best numerical approximation to $\mathbf{x}$. Actually, looking to Figure 4.2, we see that $\mathbf{x}^{10}$ has a much smoother profile (and from the simulations we saw that the minimum error is indeed attained for $\mathbf{x}^{10}$): we may conclude that this solution would be a better choice than $\mathbf{x}^{0.1}$.
A possible approach to solve this problem could be to modify the least squares problem including a penalty on the second derivative of $\mathbf{x}^\lambda$. This could be

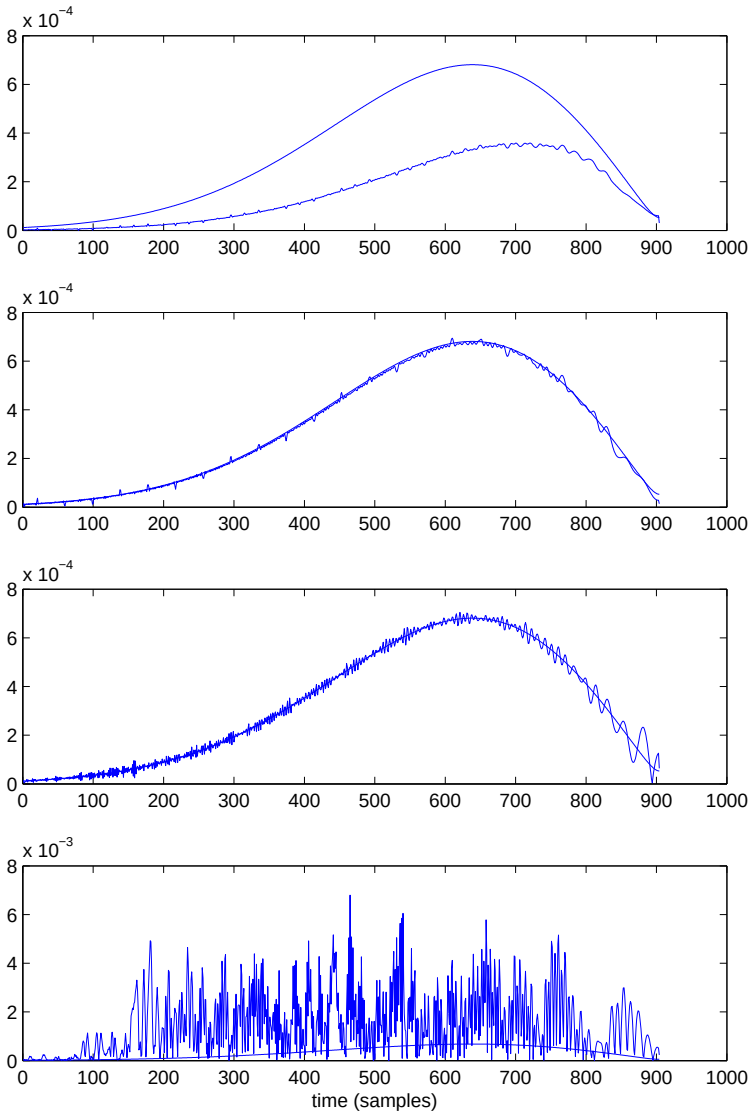

Figure 4.2: $|\mathbf{x}^\lambda|$ and $\mathbf{x}$ for (from top to the bottom) $\lambda = 1000, 10, 0.1$ and 10^{-5}.

done by mean of the second-derivative operator $\mathbf{D}$:

$$\mathbf{D} = \frac{1}{\Delta t^2}\begin{pmatrix} -2 & 1 & 0 & 0 & \dots \\ 1 & -2 & 1 & 0 & \dots \\ 0 & 1 & -2 & 1 & \dots \\ 0 & 0 & 1 & -2 & \dots \\ \vdots & \vdots & \vdots & \vdots & \ddots \end{pmatrix}$$

The modified least squares problem becomes

$$\text{argmin}_{\mathbf{x}^\lambda} \left(\|\mathbf{A}\mathbf{x}^\lambda - \mathbf{b}\|_2^2 + \lambda \|\mathbf{x}^\lambda\|_2^2 + \eta \|\mathbf{D}\mathbf{x}^\lambda\|_2^2 \right) \tag{4.1}$$

with η a positive, real parameter. Note that (4.1) can be simplified to the form

$$\text{argmin}_{\mathbf{x}^\lambda} \left(\|\mathbf{A}\mathbf{x}^\lambda - \mathbf{b}\|_2^2 + \|\mathbf{L}_{\lambda,\eta}\mathbf{x}^\lambda\|_2^2 \right). \tag{4.2}$$

To see this, write

$$\mathbf{C} \equiv \lambda \mathbf{I} + \eta \mathbf{D}^H \mathbf{D}$$

and perform the Cholesky decomposition (this is possible since $\mathbf{C}$ is symmetric positive definite)

$$\mathbf{C} = \mathbf{L}_{\lambda,\eta}\mathbf{L}_{\lambda,\eta}^H$$

where $\mathbf{L}_{\lambda,\eta}$ is a lower triangular matrix with strictly positive diagonal entries. It follows that:

$$\begin{aligned} \|\mathbf{L}_{\lambda,\eta}\mathbf{x}\|^2 &= \mathbf{x}^H \mathbf{L}_{\lambda,\eta}^H \mathbf{L}_{\lambda,\eta}\mathbf{x} = \mathbf{x}^H \mathbf{C}^H \mathbf{x} = \mathbf{x}^H (\lambda \mathbf{I} + \eta \mathbf{D}^H \mathbf{D})^H \mathbf{x} = \\ &= \mathbf{x}^H \lambda \mathbf{I}\mathbf{x} + \mathbf{x}^H \eta \mathbf{D}^H \mathbf{D}\mathbf{x} = \lambda \|\mathbf{x}^\lambda\|_2^2 + \eta \|\mathbf{D}\mathbf{x}^\lambda\|_2^2 \end{aligned}$$

Extra work could be done to implement the term $\|\mathbf{L}_{\lambda,\eta}\mathbf{x}^\lambda\|^2$ instead of $\lambda\|\mathbf{x}^\lambda\|^2$ in the mCGLS algorithm. This would go beyond the scopes of the present project and we leave it to future extensions of this paper.

Another phenomenon of fundamental importance is the discrepancy between the error and the residual for $\lambda < 10$: while the residual keeps reducing and eventually converge to 0.0019, the error increases. This fact is explained by the numerical instability of the original unregularized least square problem. In this case $\kappa(\mathbf{A}) \approx 3.5 \cdot 10^{11}$ resulting in a strongly unstable algorithm (remember that CG applied to the normal equations requires working with $\mathbf{A}^T\mathbf{A}$ whose condition number is $\kappa(\mathbf{A})^2$). For small values of λ the problem persists, while the regularization starts to have a beneficial effect for $\lambda \geq 10^{-5}$: the matrix $\mathbf{A}^\lambda$ defined as

$$\mathbf{A}^\lambda \equiv \begin{bmatrix} \mathbf{A} \\ \sqrt{\lambda}\mathbf{I} \end{bmatrix}$$

becomes better conditioned. For instance, for $\lambda = 1$ and $\lambda = 100$ we have $\kappa(\mathbf{A}^\lambda) \approx 101$ and $\kappa(\mathbf{A}^\lambda) \approx 10.1$ respectively.

λ	$\frac{\|\mathbf{x}^\lambda - \mathbf{x}\|}{\|\mathbf{x}\|}$	$\frac{\|\mathbf{A}\mathbf{x}^\lambda - \mathbf{b}\|}{\|\mathbf{b}\|}$
10^4	0.9074	0.8746
10^3	0.5290	0.4692
10^2	0.1125	0.0923
10^1	0.0260	0.0107
10^0	0.0313	0.0028
10^{-1}	0.0634	0.0024
10^{-2}	0.1469	0.0023
10^{-3}	0.4965	0.0022
10^{-4}	1.6301	0.0021
10^{-5}	4.7461	0.0019
10^{-6}	7.2343	0.0019
10^{-7}	7.6516	0.0019
10^{-8}	7.6964	0.0019
10^{-9}	7.7009	0.0019
10^{-10}	7.7014	0.0019

Table 4.1: Relative error $\frac{\|\mathbf{x}^\lambda - \mathbf{x}\|}{\|\mathbf{x}\|}$ and residual $\frac{\|\mathbf{A}\mathbf{x}^\lambda - \mathbf{b}\|}{\|\mathbf{b}\|}$ for Simulation 1.

Finally, we test the numerical solutions with a Bloch Equation simulator. The respective errors for different values of λ are reported in table 4.2 and plotted in figure 4.4. Note that the errors from the simulator behave similarly to the residuals from the mCGLS algorithm: they decrease quickly as λ decreases in the range $[10^4, 1]$. For smaller values of λ they stabilize.

In conclusion, the effect and the need for the regularization is clear: the extremely unstable numerical process gains in stability and the computed solutions are, depending on the parameter λ, smoother and more reliable. Of course, the exact solution is in general not known but from the L-curve we are able to choose a good numerical solution which approximates the exact one. The error obtained from the Bloch equation simulator is also highly informative w.r.t. a good choice of the numerical solution: this can be another valuable criterion for an optimal choice and, for applications, it may be more reliable than the L-curve approach, since the residuals computed for this curve suffer of instability problems.

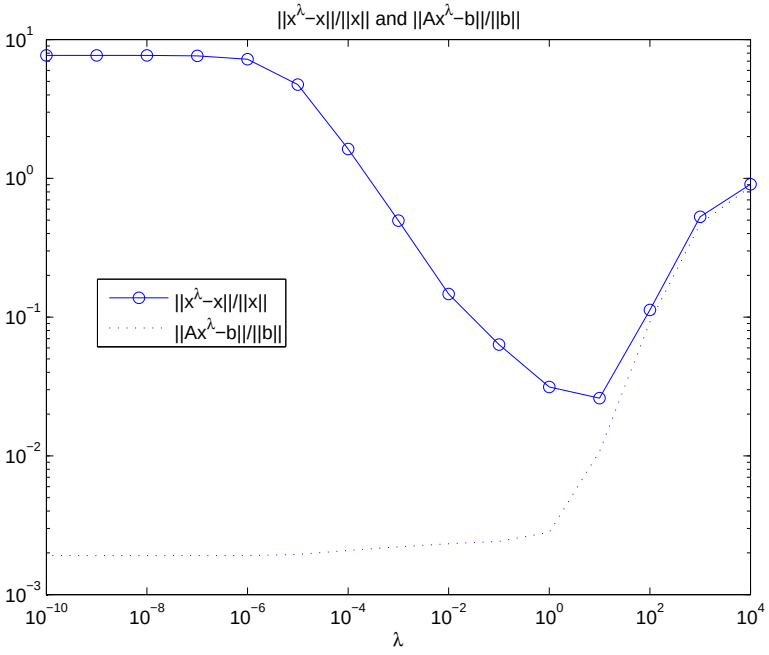

Figure 4.3: Relative error $\frac{\|\mathbf{x}^\lambda - \mathbf{x}\|}{\|\mathbf{x}\|}$ (solid line) and residual $\frac{\|\mathbf{A}\mathbf{x}^\lambda - \mathbf{b}\|}{\|\mathbf{b}\|}$ (dotted line) for Simulation 1.

λ	$\|E_x\|_2$	$\|E_y\|_2$	$\|E_{\text{abs}}\|_2$	$\|E_x\|_\infty$	$\|E_y\|_\infty$	$\|E_{\text{abs}}\|_\infty$
1e+04	5.48e-03	1.75e+00	1.75e+00	5.76e-04	7.35e-01	7.35e-01
1e+03	2.60e-03	9.45e-01	9.45e-01	3.61e-04	4.17e-01	4.17e-01
1e+02	2.93e-03	2.01e-01	2.01e-01	6.39e-04	9.28e-02	9.28e-02
1e+01	3.32e-03	4.05e-02	4.06e-02	7.47e-04	1.93e-02	1.93e-02
1e+00	2.95e-03	2.26e-02	2.27e-02	7.11e-04	1.09e-02	1.09e-02
1e-01	2.58e-03	2.10e-02	2.10e-02	7.27e-04	1.02e-02	1.02e-02
1e-02	2.50e-03	2.09e-02	2.10e-02	7.46e-04	1.01e-02	1.01e-02
1e-03	2.45e-03	2.08e-02	2.09e-02	7.48e-04	1.01e-02	1.01e-02
1e-04	2.42e-03	2.05e-02	2.05e-02	7.31e-04	9.97e-03	9.97e-03
1e-05	2.67e-03	2.15e-02	2.16e-02	6.68e-04	9.55e-03	9.55e-03
1e-06	2.95e-03	2.53e-02	2.54e-02	6.53e-04	9.14e-03	9.14e-03
1e-07	3.01e-03	2.60e-02	2.61e-02	6.58e-04	9.07e-03	9.07e-03
1e-08	3.01e-03	2.61e-02	2.62e-02	6.59e-04	9.06e-03	9.06e-03
1e-09	3.01e-03	2.61e-02	2.62e-02	6.59e-04	9.06e-03	9.06e-03
1e-10	3.02e-03	2.61e-02	2.62e-02	6.59e-04	9.06e-03	9.06e-03

Table 4.2: Simulation 1. Errors obtained by the Bloch Equation Simulator run for every numerical solution.

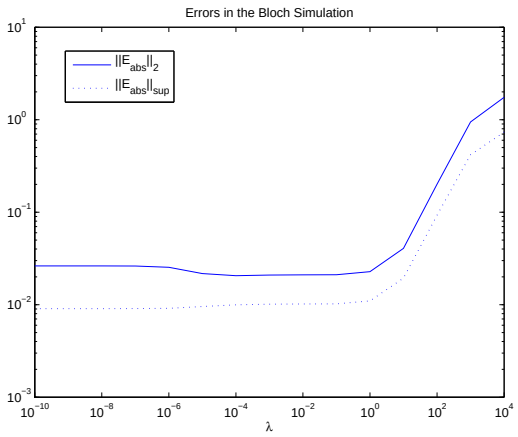

Figure 4.4: $\|E_{\text{abs}}\|_2$ (solid line) and $\|E_{\text{abs}}\|_\infty$ (dotted line) for from the Bloch Simulation for Simulation 1.

4.2 Simulation 2

Undersampling of k-space and Sensitivity encoding. Effect of Sensitivity profile on the obtained magnetization

As we have seen in the explanation of the SENSE method for parallel imaging, the non uniform sensitivity profiles S_p can be seen as a new kind of encoding functions which have a larger extent in the spatial frequency domain (standard Fourier encoding functions are plane waves whose corresponding Fourier Transform is a Dirac peak). An important consequence is that information collected during k-space scanning is not limited to a single sampled point but it is a weighted integral over a neighborhood of the corresponding point in k-space. We will investigate the functioning of SENSE (transmit version) by undersampling by a factor 2 the k-space scan in the radial direction (i.e. reducing the number of spiral interleaves n by a factor 2). In standard Fourier encoding this would lead to a aliases en hence to a large error between the desired magnetization profile and the obtained profile. We will employ 4 different sensitivity profiles relative to 2 transmit channels:

- profile a): two perfectly uniform profiles: $S_p(\vec{r}) = 1$ for every $\vec{r}$ and $p = 1, 2$.
- profile b): two complex valued Gaussian profiles (see figure 4.5)
- profile c): as profile b) but with an extra oscillating term (see figure 4.6)

- profile d): two complex profiles obtained by electromagnetic simulations relative to a slice in a human brain (see figure 4.7).

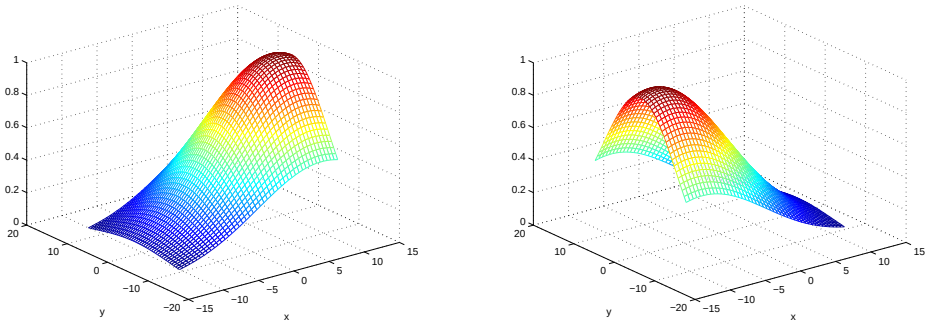

Figure 4.5: Sensitivity profiles b) (absolute value).

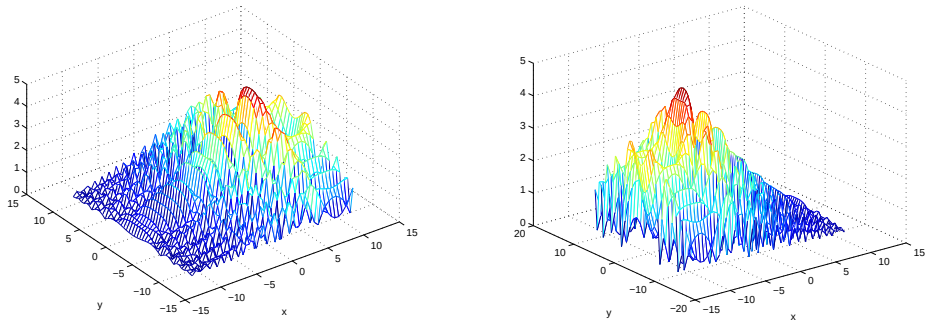

Figure 4.6: Sensitivity profiles c) (absolute value).

We choose again, a Gaussian magnetization profile with $\mu_1 = 0.1$, $\mu_2^2 = 0.4\pi$ and centered at $\vec{r} = (0, 0)$. Furthermore we set FOV=22.5 and $N_s = 46$, resulting in a spatial resolution $\Delta r = 0.5$. With a Nyquist sampling, we should require $n = 13$ and, running the optimization algorithm for the spiral trajectory under constraints $G_{\max} = 3.0$ and $S_{\max} = 14.0$, the required number of sample points would be $N_t = 1825$. By halving the number of spiral interleaves, i.e. setting $n = 13/2$ we get $N_t = 927$, thus the reduction factor is about 2. To the gradients obtained from Algorithm 4 we append an initial ramp (with maximum allowed slope, that is the maximum allowed slew rate) since the initial condition is $\vec{G}(0) = \mathbf{0}$ (see figure 4.8). The dimensions of the

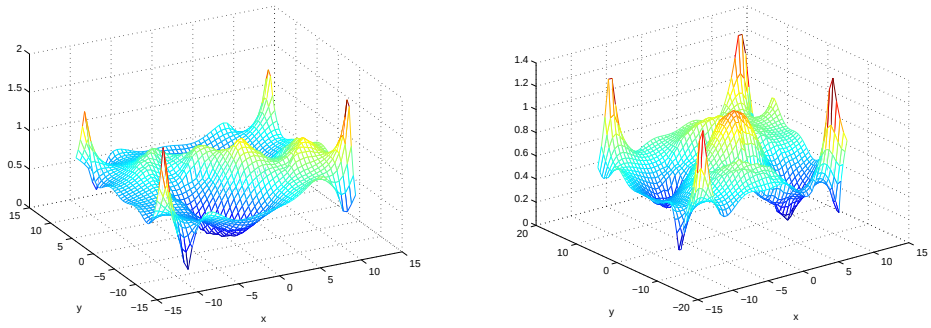

Figure 4.7: Sensitivity profiles d) (absolute value).

matrix $\mathbf{A}$ will be $N_s^2 \times N_t P = 46^2 \times 927 \cdot 2 = 2116 \times 1854$.

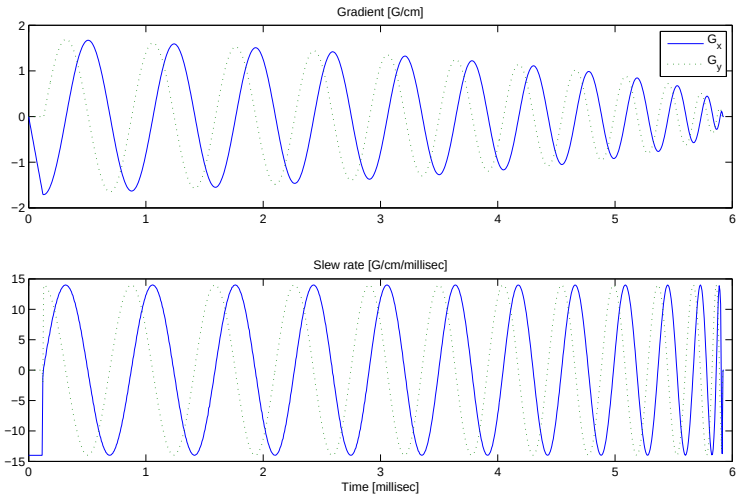

Figure 4.8: The Gradient (and slew rate) for the 2-fold radially undersampled k-space trajectory. Note the initial ramp to the G_x component.

We run mCGLS for the four profiles described above. The resulting L-curve are displayed in figures 4.9 and 4.10. Note that, indeed, the sensitivity encoding has a dramatically positive effect on the residuals $\mathbf{r}$. While for the profile a) (standard Fourier encoding) $\frac{\|\mathbf{r}\|}{\|\mathbf{b}\|} > 10^{-0.4} \approx 0.4$, for the other three profiles we achieve $\frac{\|\mathbf{r}\|}{\|\mathbf{b}\|} \leq 10^{-1} = 0.1$ (for our applications purposes, a relative residual norm of 0.1 can be considered small enough). Also, note that the

achieved accuracy for profiles b) and d) is larger w.r.t that one obtained for profile c): a reason for this could be that the oscillating term has a negative impact on the smoothness of $S(\vec{r})$ causing a noise-like effect (see figure 4.6). Looking at the behavior of the errors obtained from the Bloch Simulator (figure 4.11) we note a fundamental difference w.r.t. the errors from Simulation 1 (figure 4.4): $\|E_{\text{abs}}\|_2$ and $\|E_{\text{abs}}\|_\infty$ do not longer monotonically grow. There is a value of λ for which the errors attain a minimum and the choice for the good shift value (and hence for a good numerical solution) is therefore unambiguous and less free.

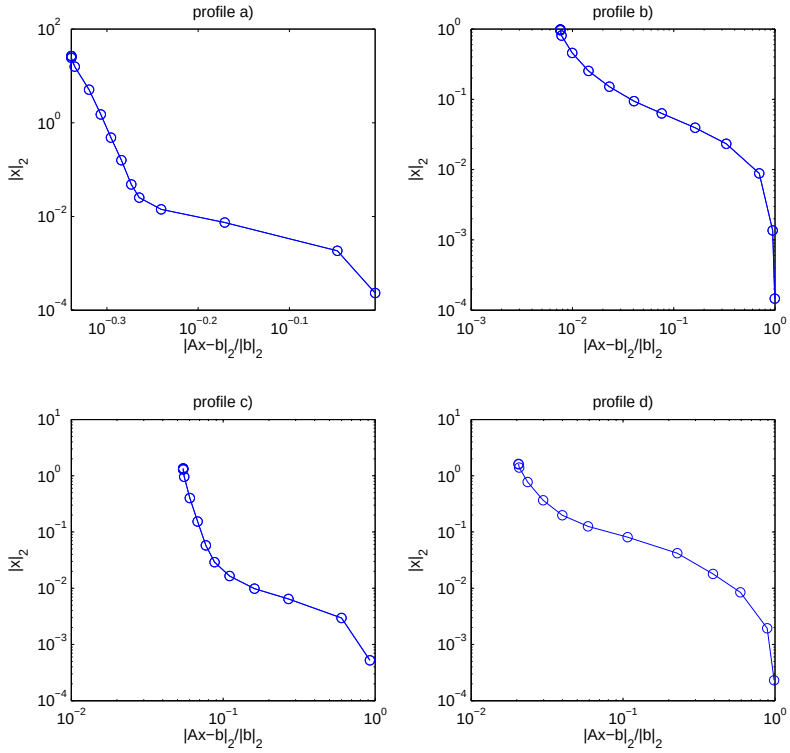

Figure 4.9: The L-curves for the four sensitivity profiles.

Eight-fold radial undersampling

It is interesting to investigate how the accuracy of the obtained magnetization is related to the sensitivity profiles for a larger reduction factor. For this purpose we take eight parallel transmit channels ($P = 8$) and we construct 3 different kinds of sensitivity patterns. They are displayed in figure

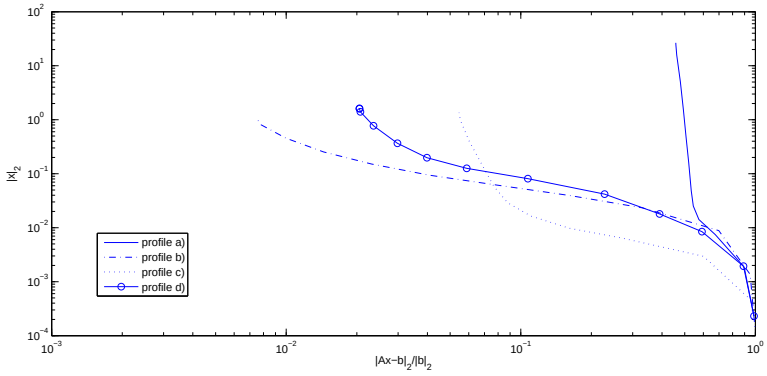

Figure 4.10: The L-curves for the four sensitivity profiles.

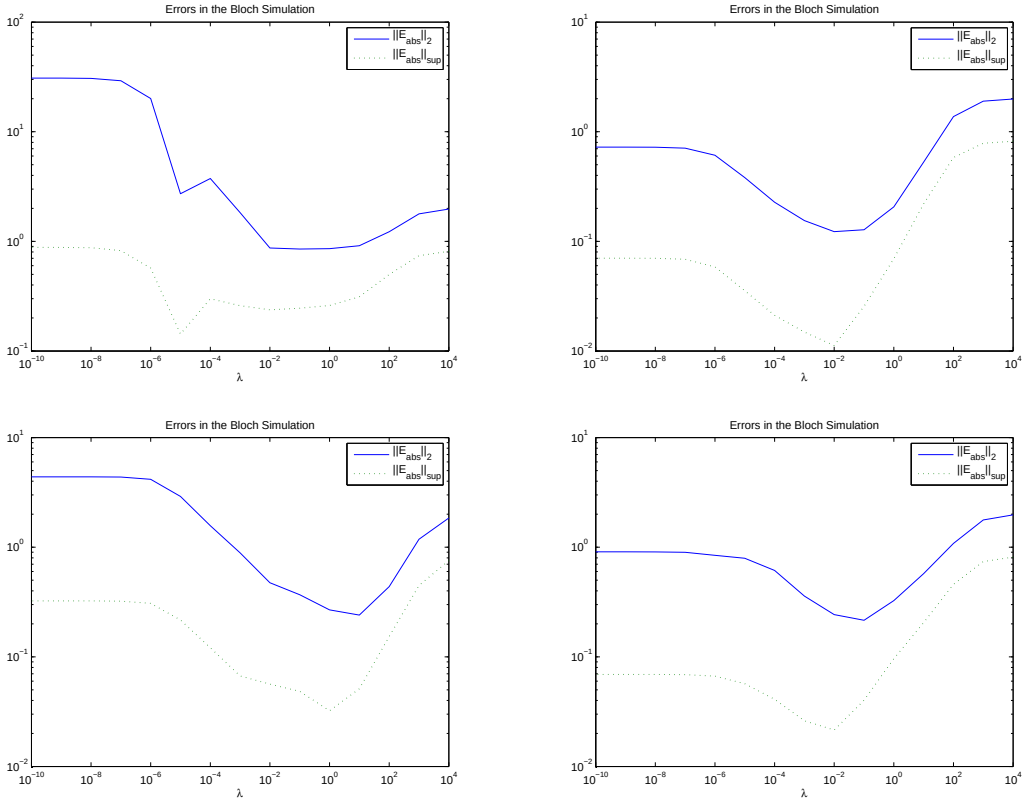

Figure 4.11: Errors $\|E_{\text{abs}}\|_2$ (solid line) and $\|E_{\text{abs}}\|_\infty$ (dotted line) from the simulated magnetizations corresponding to profile a) (top-left), profile b) (top-right), profile c) (bottom-left) and profile d) (bottom-right).

4.12 together with their respective Discrete Fourier Transforms (the other 7 profiles are not displayed but have the same form, only they are rotated by intervals of 45^o and have different phases). Note that the sensitivity spectra have an increasing extent from profile e) to profile g). We should expect that the errors obtained from the simulated magnetization decrease as the spectrum extent increases. First we run mCGLS for the 3 cases and plot the resulting L-curves in figure 4.13. The spiral trajectory is radially undersampled by a factor 8 , that is $n = 13/8$ and it is showed in figure 4.15 (now $N_t = 260$ for the same magnetization pattern as above: a reduction factor of $1825/260 \approx 7$).
Indeed, the residual from the profile g) lies mostly below that from profile f) which lies on his turn below that of profile e). The errors obtained from the Bloch Simulator for the 3 sets of numerical solutions are plotted in figure 4.14. The accuracy seems to improve with the increasing of the spectrum extent.
The eight waveforms extracted from the numerical solution $\mathbf{x}^{0.01}$ relative to profile g) and the corresponding simulated magnetization profile are displayed in figure 4.16 and 4.17 respectively.

In conclusion: the non homogeneous sensitivity profiles allow an accurate excitation even in case of k-space undersampling. In case the frequency extent of the sensitivity maps is large enough, it is possible to achieve large reduction factors (in the previous case it was about 7) and still ensure an accurate enough excitation pattern.

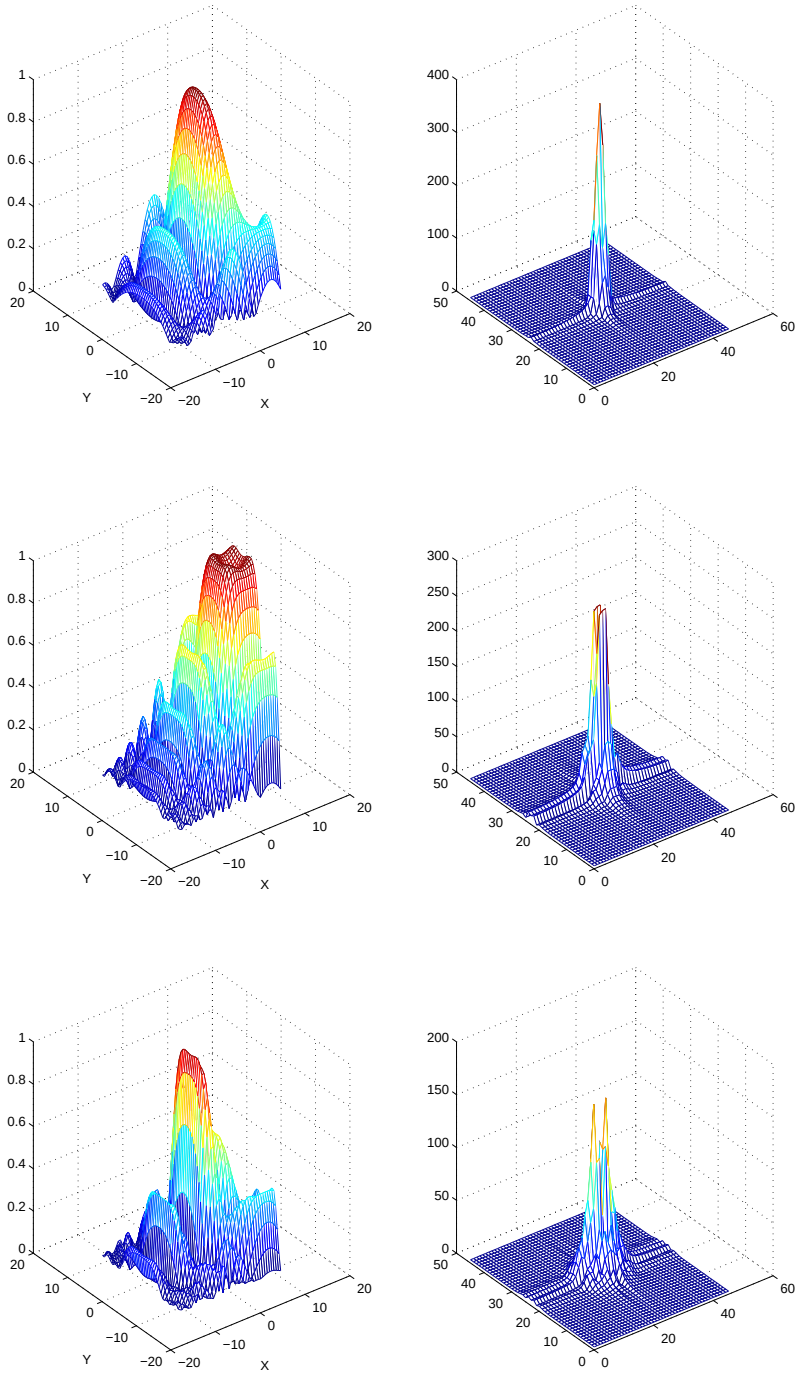

Figure 4.12: Eight-fold radial undersampling: sensitivity profiles (absolute values). Profile e) (top), profile f) (center) and profile g) (bottom) .

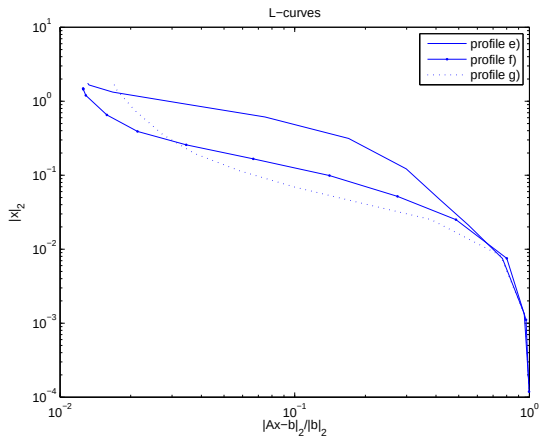

Figure 4.13: Eight-fold radial undersampling: the L-curves for the sensitivity profiles e), f) and g).

4.3 Simulation 3

Other numerical aspects: a different excitation profile, an extra regularization term and a larger spatial resolution

We will now treat the problem of exciting uniformly the inner part of an object (in this specific case it will be a human head), trying to avoid excitation of the outer part. The external part of the human head corresponds to the fat and bone tissues: the signal coming from these two materials can considerably disturb the signal coming from the brain. Avoiding the excitation of the fat and bone tissues improves the SNR in MRI applications like spectroscopy.
This problem asks for a new kind of function, since the Gaussian profile is no longer able to describe accurately the desired magnetization function. We need a function which is close to a non zero constant inside a given (elliptic) region and it is close to zero outside. Also, the function should be as smooth as possible, making possible a good reconstruction from the $k-$space representation to the spatial domain. For this purpose, we introduce a combination of Fermi functions given by

$$M_y(\vec{r}) = \mu_1 \left(\frac{1}{e^{\frac{\rho-\alpha}{\beta}} + 1} - \frac{1}{e^{\frac{\rho+\alpha}{\beta}} + 1} \right) \tag{4.3}$$

with

$$\rho = \sqrt{(x/a)^2 + (y/b)^2}$$

where $\vec{r} = (x, y)$, a and b are parameters related to the elliptic profile of the desired excitation region, α and β determine the width and steepness of

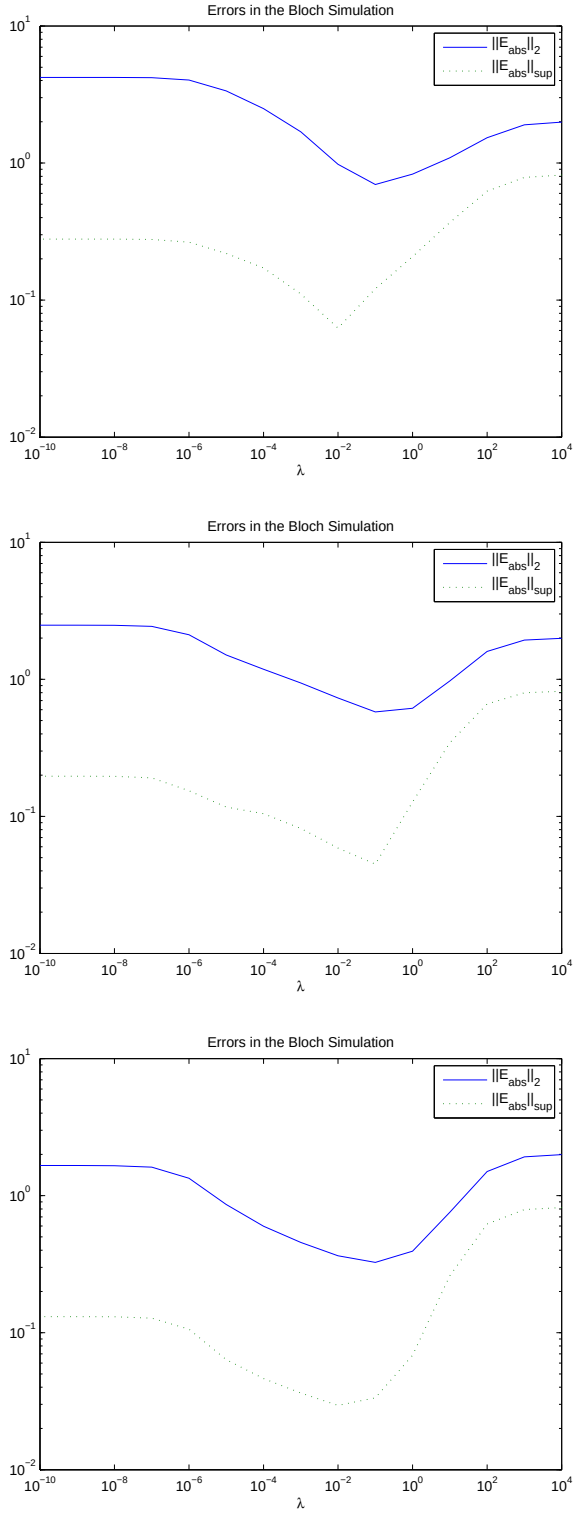

Figure 4.14: Eight-fold radial undersampling: errors $\|E_{\text{abs}}\|_2$ (solid line) and $\|E_{\text{abs}}\|_\infty$ (dotted line) from the simulated magnetizations corresponding to profile e) (top), profile f) (center) and profile g) (bottom) .

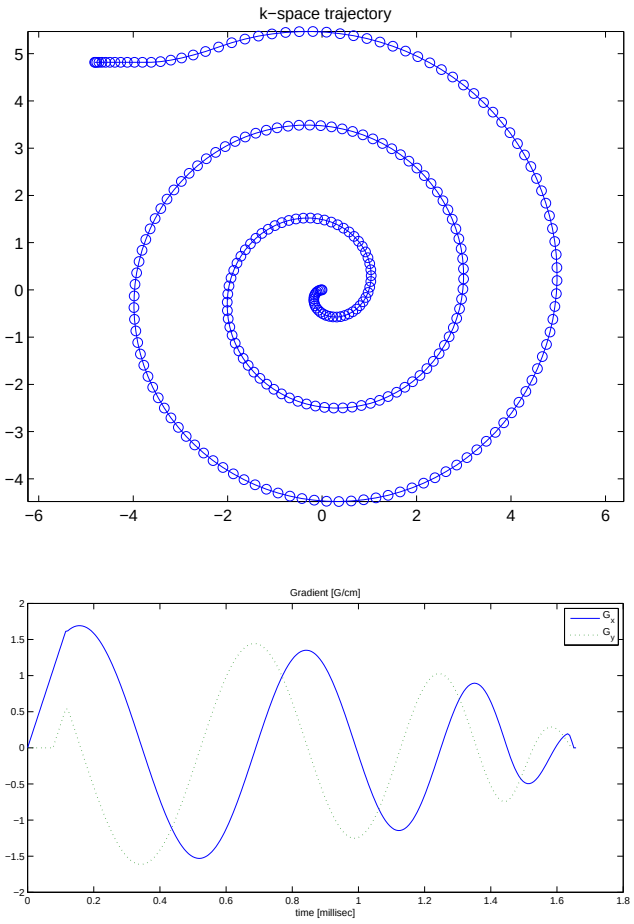

Figure 4.15: The eight-fold undersampled k-space trajectory (top) with the respective Gradient (bottom).

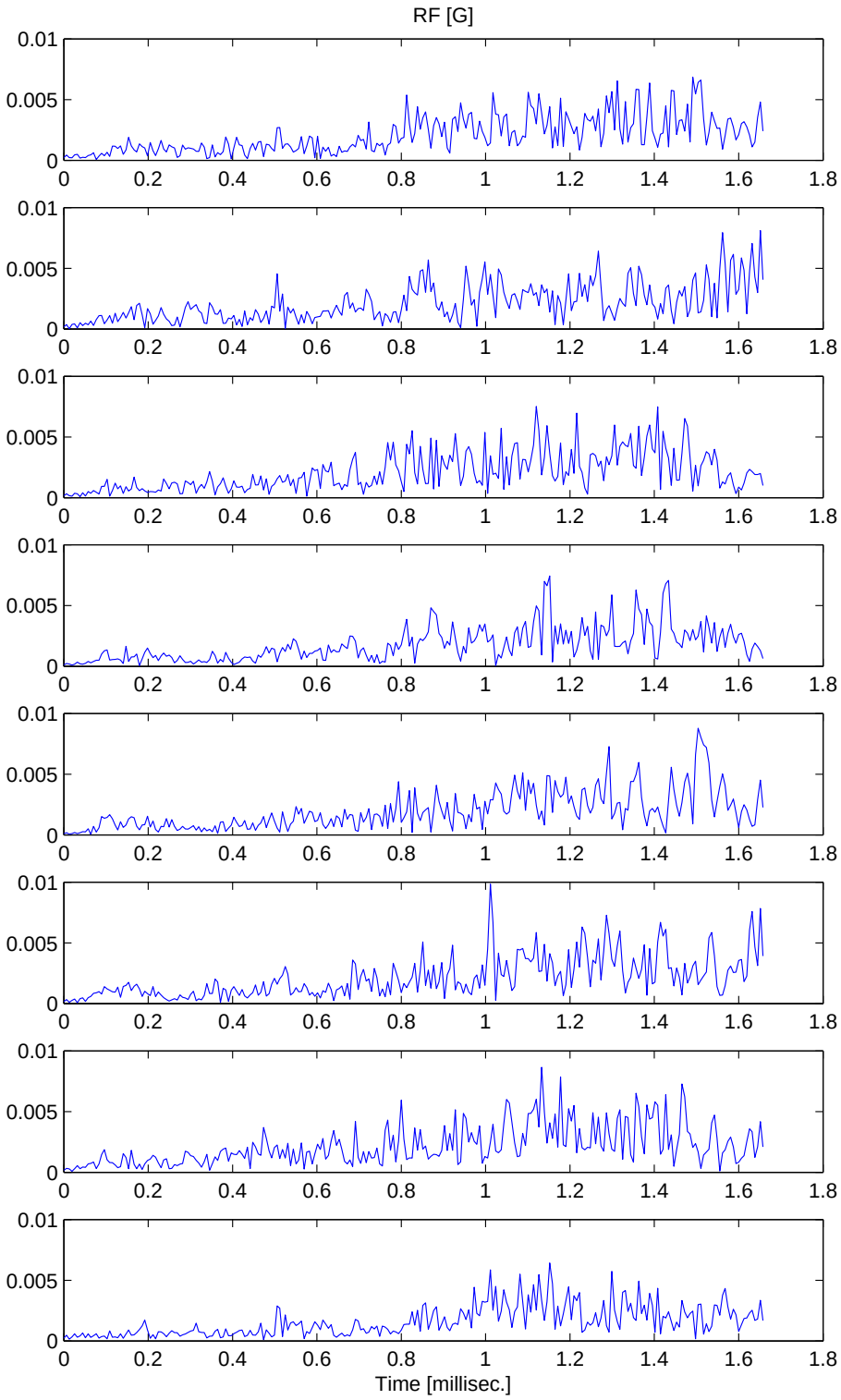

Figure 4.16: The eight RF waveforms (numerical solution) for profile g) and $\lambda = 10^{-2}$.

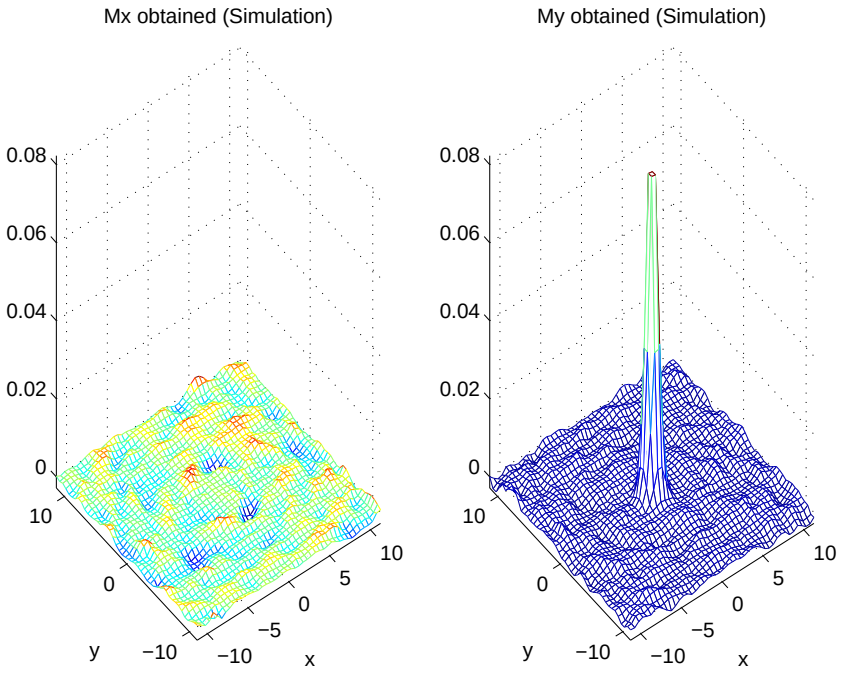

Figure 4.17: The simulated magnetization obtained for profile g) and $\lambda = 10^{-2}$.

the Fermi function and μ_1 scales the flip angle. For instance, for $a = 8, b = 10, \alpha = 1, \beta = 0.03$ and $\mu_1 = 0.1$ we get the magnetization profile displayed in figure 4.18. The respective Discrete Fourier Transform and the profile section along the line $y = 0$ are also displayed.

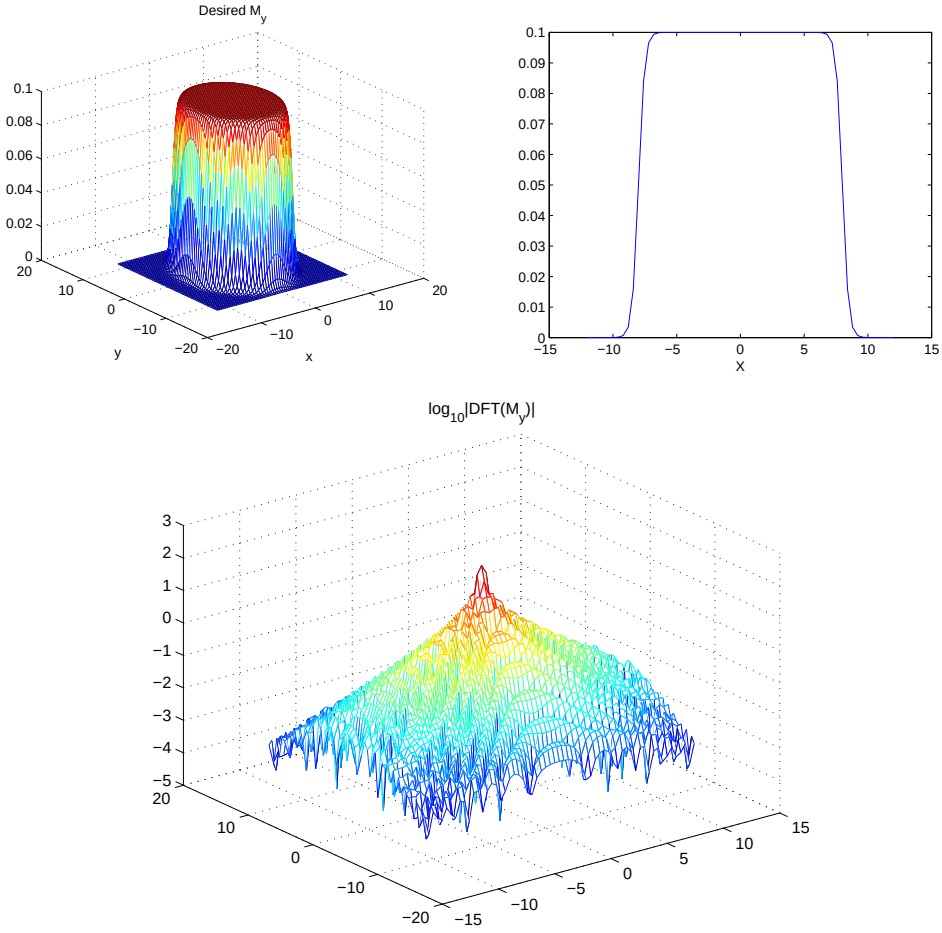

Figure 4.18: M_y for $\beta = 0.03$. Top-left: over the whole spatial domain; top-right: along the line $y = 0$; bottom: Discrete Fourier Transform.

The parameter β determines the steepness of the profile at the boundaries of the excitation region. Taking a smaller value for β the profile approximates a boxcar function. This implies that more Fourier coefficients are required in the k-space scanning and thus a larger number of sample points. In figure 4.19 is displayed $M_y(\vec{r})$ for $\beta = 0.001$: note the larger magnitude of the Fourier coefficients w.r.t. the previous case. This combination of Fermi functions can

therefore be viewed as a filtered version of a two-dimensional elliptic-shaped boxcar-function: the parameter β quantifies the filtering effect.

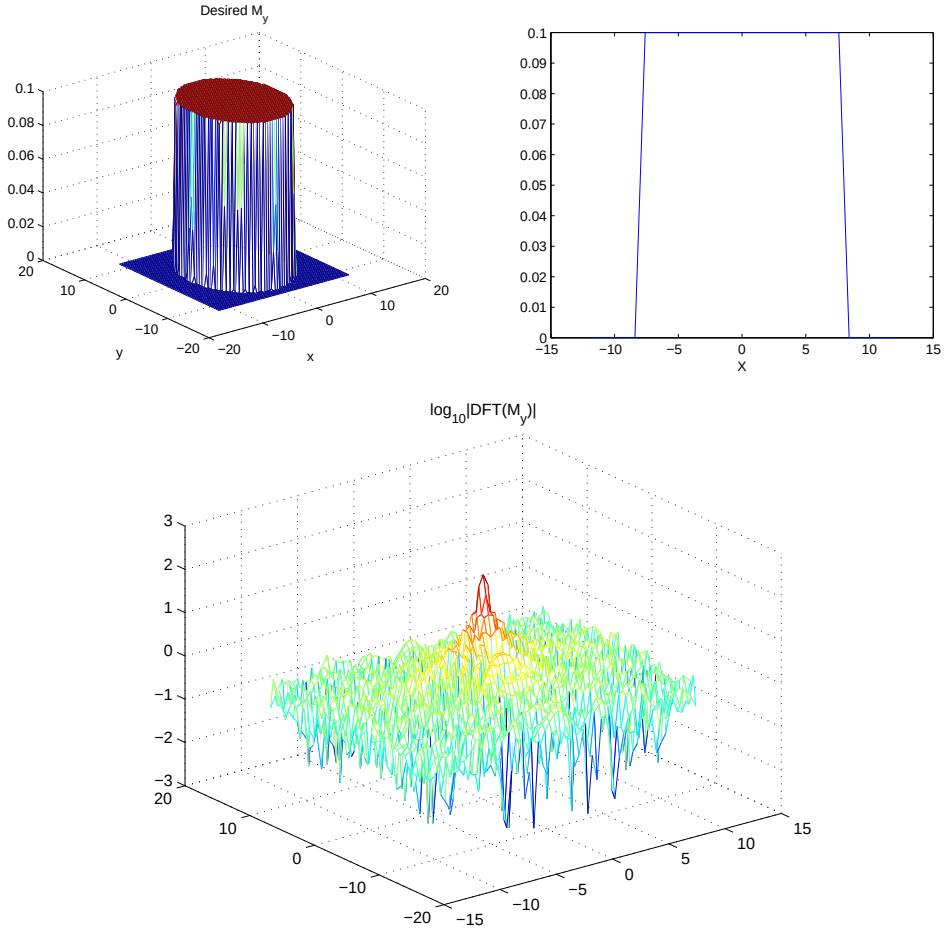

Figure 4.19: M_y for $\beta = 0.001$. Top-left: over the whole spatial domain; top-right: along the line $y = 0$; bottom: Discrete Fourier Transform.

When we solve the problem

$$\text{argmin}_x\{\|\mathbf{Ax} - \mathbf{b}\|_2^2 + \lambda\|\mathbf{x}\|_2^2\} \tag{4.4}$$

we do not take into account that a great part of the spatial domain corresponds to an area outside the body being excited. In practice, we are only interested on what happens to the spins inside the body, since signal from the surrounding medium (air) can be neglected. We define a region of interest (ROI) of elliptic shape and we distinguish between the residual inside the

ROI and outside of it through an extra spatial weight term in (4.4) in the form of a diagonal matrix $\mathbf{W}$ defined as

$$\mathbf{W}(i,i) = \begin{cases} \xi & \text{if } \mathbf{p}(i) \in \text{ROI} \\ 1 & \text{otherwise} \end{cases}$$

where $\xi > 1$ has to be chosen and $\mathbf{p}(i)$ refers to the pixel corresponding to the i-th diagonal entry of $\mathbf{W}$. The least square problem (4.4) becomes then

$$\text{argmin}_x\{\|\mathbf{W}(\mathbf{A}\mathbf{x} - \mathbf{b})\|_2^2 + \lambda\|\mathbf{x}\|_2^2\}. \tag{4.5}$$

For large values of ξ we force the residual components to be smaller inside the ROI while we allow them to be larger outside.
To speed up the computations, in particular the running time of mCGLS, we may reduce the size of $\mathbf{A}$. A spatial resolution of $\Delta r = 0.5$ implies $N_s = 48$ for FOV=24 cm. This means that $\mathbf{A}$ will have $48^2 \approx 2300$ rows. Assuming $\mathbf{A}$ is approximately square, the two matrix-vector products in a single iteration step of the algorithm require about $2 \cdot 2300^2 \approx 10 \cdot 10^6$ FLOP's each. In practice, a coarser resolution, for instance $\Delta r = 0.75$, this implies that a matrix-vector product requires about $2 \cdot 10^6$ FLOP's. In comparison to the previous spatial resolution, a speed up factor of at least 5 can be achieved (in general, a smaller matrix requires also fewer iterations steps than a larger one, thus the speed up factor should be higher than 5).

We take the profile given by (4.3) with $a = 6$, $b = 8$, $\alpha = 1$, $\beta = 0.05$, $\mu_1 = 0.5$, FOV=24cm and $\Delta r = 0.75$cm (see Figure 4.20). Note also, from Figure 4.20, that the frequency-domain profile (DFT) is much more irregular than the Gaussian profiles we have studied so far. We could expect problems caused by an undersampled k-space scanning, due to the irregularity of DFT(M_y). The spiral trajectory could be no longer an effective choice. However, also in this case, we will study the behavior of the transmit SENSE method through a spiral sampling to get insight in the problem. For the ROI we choose an elliptic-shaped region centered at the origin, i.e.

$$\text{ROI} = \left\{(x,y) \in \mathbb{R}^2 : \left(\frac{x}{a^*}\right)^2 + \left(\frac{y}{b^*}\right)^2 \leq 1\right\}$$

with $a^* = 9$cm and $b^* = 11$cm (this choice of parameters corresponds approximately to the typical dimension of an adult head's transversal section). In Figure 4.21 are displayed M_y and the ROI (region delimited by the black line). We run mCGLS for a two channels system with sensitivity profiles d) from simulation 2. The simulation is repeated three times, with the following changes:

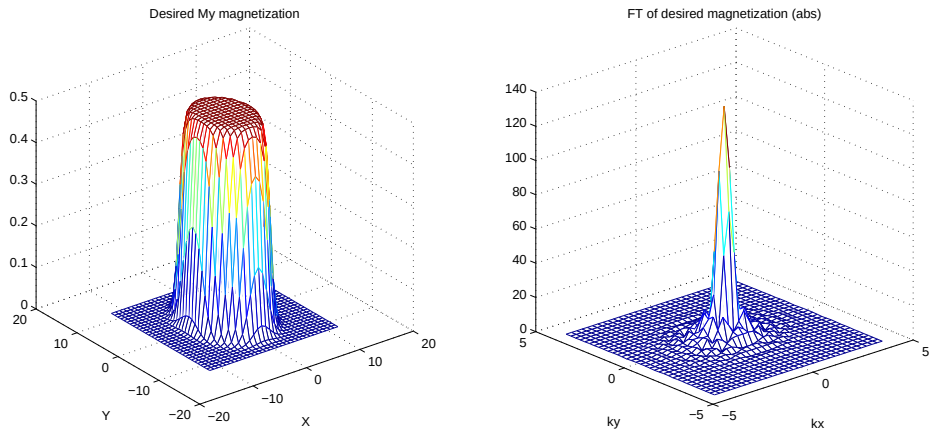

Figure 4.20: The desired magnetization profile M_y (left) and its Discrete Fourier Transform (right) for simulation 3.

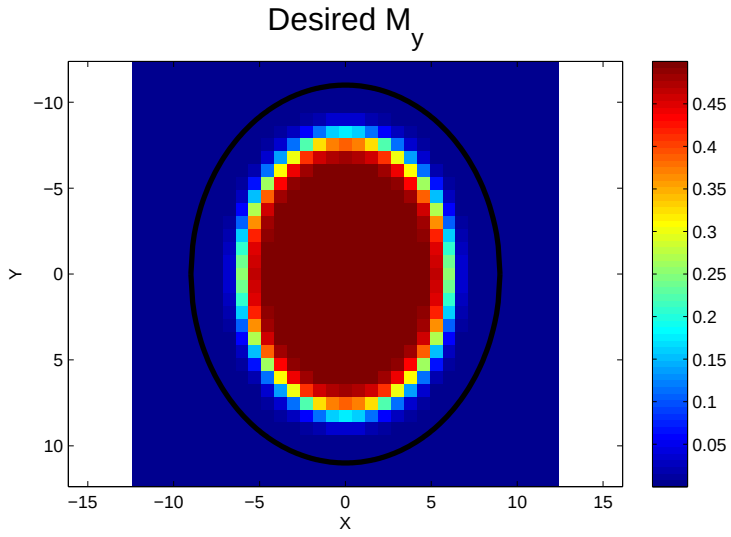

Figure 4.21: The desired magnetization profile M_y and the boundary of the ROI (black line) for simulation 3.

- Simulation 3a: No weighting matrix is employed and $n = n_a \equiv N_s/2/2 = 33/4$ (radial undersampling by factor 2)
- Simulation 3b: the weighting matrix $\mathbf{W}$ is employed and $n = n_a$ (again a radial undersampling by factor 2)
- Simulation 3c: the weighting matrix $\mathbf{W}$ is employed and $n = n_a * 1.2$ (radial undersampling by factor 1.7)

In simulation 3c we slightly increase the spiral density by a factor 1.2. In this way we hope to achieve a better accuracy without loosing speed in the k-space scan. We run Algorithm 4: for simulations 3a and 3b we obtain $N_t = 511 \approx 3.3$ millisec. ($\Delta t = 0.0064$ millisec) while for simulation 3c we have $N_t = 606 \approx 3.9$ millisec. The graph of the respective error $\|E_{abs}\|_2$ and $\|E_{abs}\|_\infty$ evaluated inside the ROI are plotted in Figure 4.22.

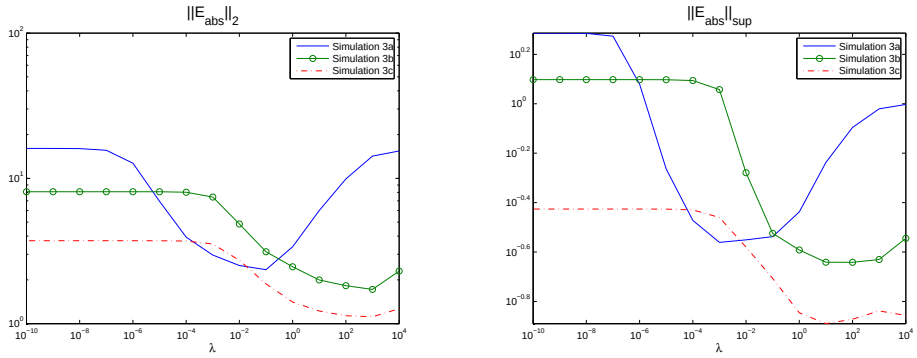

Figure 4.22: Errors $\|E_{\text{abs}}\|_2$ (left) and $\|E_{\text{abs}}\|_\infty$ (right) from the magnetization of Simulation 3. The errors are evaluated inside the ROI

Looking at Figure 4.22 we see that the introduction of the weighting matrix $\mathbf{W}$ has indeed a benefical effect on the error obtained. However, the accuracy achieved with the two-fold radial undersampling is now much lower than that one achieved when a Gauss profile had to be excited (see Simulation 2). As we predicted, the irregular spatial frequency profile of M_y gives rise to problems regarding an efficient and accurate way to scan the k-space. Undersampling following a spiral trajectory does not seem to be the best strategy. Note that, increasing the scanning density, a better accuracy is obtained: this facts confirms that the problems is how to find an optimal k-space trajectory which guarantee the shortest scanning time and the smallest error in the obtained magnetization. However, the best numerical solution from simulation 3 (that is, $\mathbf{x}^{10}$ from simulation 3c) can

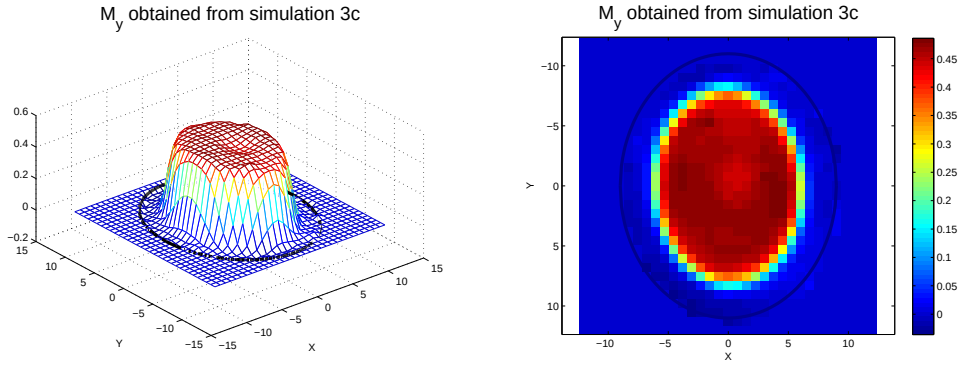

Figure 4.23: The magnetization profile M_y obtained from simulation 3c for $\lambda = 10$.

still be employed , since the corresponding simulated profile (see Figure 4.23) is considered "good enough" for MRI applications.

4.4 Simulation 4

SAR computations

An important constraint for clinical application of any transmit system is the 1-gram SAR constraint. Recall, from chapter 3, that the SAR per voxel is defined as

$$\mathrm{SAR}(\vec{r}) \equiv \frac{\sigma(\vec{r})}{2\rho(\vec{r})}\frac{1}{D}\int_0^D \|\vec{E}(\vec{r},t)\|_2^2 dt \approx \frac{\sigma(\vec{r})}{2D\rho(\vec{r})}\Delta t \sum_{n=0}^{N_t-1} \|\vec{E}(\vec{r},n\Delta t)\|_2^2 \quad (4.6)$$

with

$$\vec{E}(\vec{r},t) = \sum_{p=1}^{P} B_{1,p}(t)\vec{E}_p(\vec{r}) \quad (4.7)$$

and $B_{1,p}$ the RF pulse from the p-th transmit channel. After having computed $\mathrm{SAR}(\vec{r})$ over the whole (3 dimensional) region exposed to the RF fields, the 1-g SAR can be evaluated by averaging $\mathrm{SAR}(\vec{r})$ over a one gram cube. Suppose, for instance, that the voxel dimensions are $2.5 \times 2.5 \times 2.5$ mm, and the tissue being scanned has a density of 1000 kg/m^3 (a good estimate for human tissue), then the 1-g SAR will be

$$\text{1-g SAR}(\vec{r}) = \frac{1}{4^3}\sum_{\vec{r}_i \in C(\vec{r})} \mathrm{SAR}(\vec{r}_i)$$

where $C(\vec{r}_i)$ denotes the $4 \times 4 \times 4$ pixels cube whose center lies at $\vec{r}$. The weighting factor $\frac{1}{4^3}$ derives from the dimensions of the cube: 4×2.5 mm=1cm, and 1cm^3 weights, with good approximation, 1 gram.
The computational burden can be large. To see this, suppose P transmit channels are being used. The computation of $\vec{E}(\vec{r}, t)$ from Eq. (4.7) needs $3P$ multiplications and $3(P-1)$ additions ($\vec{E}(\vec{r}, t)$ has 3 components). The L_2-norm of $\vec{E}(\vec{r}, t)$ from Eq. (4.6) requires 3 multiplications and 2 additions. In total, for every time step, and for each voxel $6P+2$ FLOPs are needed. A typical 3 dimensional spatial domain is made of about $100 \times 100 \times 100 \approx 10^6$ voxels. Neglecting the computational cost of the quantity $\frac{\sigma(\vec{r})}{2D\rho(\vec{r})}\Delta t$ and of the averaging step, the total amount of FLOPs needed for $\text{SAR}(\vec{r})$ is about $10^6(6P+2)N_t$. Considering the fact that $\vec{E}(\vec{r}, t)$ and $B_{1,p}$ are complex valued, the estimate should be doubled, leading to $2(6P+2)10^6 N_t$ FLOPs.
In case of a two channels system ($P = 2$) and $N_t = 200$ the number of FLOPs required is approximately $5.6 \cdot 10^9$. With an Intel Core2 Duo 3.0 GHz CPU and implementing the computations in an optimal MATLAB code (that is, by making use of precompiled routines and avoiding, where it is possible, `for` loops) this can be computed in about one minute. It is clear that implementing this procedure in an iterative process would require too much time (note that the above computation should be carry out for each numerical solution $\mathbf{x}^\lambda$, that is we need 1g-SAR^λ for each λ). At this moment, no efficient approach is known for a good estimate of 1g-SAR: the only reliable method to make sure the safety constraint has being fulfilled is to compute the SAR after the numerical solutions are known. In case 1g-$\text{SAR}^\lambda > \text{SAR}_{\max}$ either a scaling of $\mathbf{x}^\lambda$ has to be performed or another numerical solution, with lower L_2-norm and still acceptable error could be taken. Note that the SAR is proportional to $\|\mathbf{x}^\lambda\|_2^2$, and $\|\mathbf{x}^\lambda\|_2$ on his turn, to the flip angle θ. Scaling θ by a factor R, implies scaling the SAR by a factor R^2.
We will run the 1g-SAR for a Gaussian shaped magnetization profile centered at the origin with $\mu_1 = 0.25$, that is, for a flip angle θ equal to 14.5^o at the center of the ROI. We calculate the RF pulses for a two channels system with sensitivity profiles as in simulation 2d). Setting $\Delta t = 0.013$ milliseconds and with the same Gradient and Slew rate constraints as in the previous simulations we get $N_t = 142$ (two fold radial undersampling). The L-curve and the simulations errors corresponding to the numerical solution $\mathbf{x}^\lambda$ are plotted in figure 4.24. The maximum 1g-SAR for $\mathbf{x}^{100}$ computed making use of the electric fields data obtained from simulations is reported in Table 4.3 (only the four best numerical solutions are taken into account). Every SAR evaluation took about 90 seconds. The maximum SAR constraint is set equal

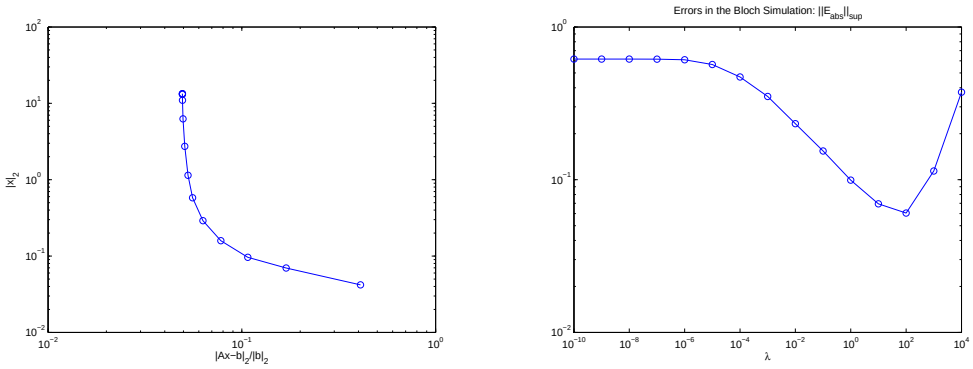

Figure 4.24: The L-curve and the errors $\|E_{\text{abs}}\|_\infty$ for Simulation 4.

λ	$\max_{\vec{r}}$ 1g-SAR($\vec{r}$) [W/kg]
1000	0.275
100	0.500
10	1.37
1	4.79

Table 4.3: Maximal 1g-SAR corresponding to the four best numerical solutions found in Simulation 4.

to

$$\mathrm{SAR}_{\max} \equiv 8 \quad [\mathrm{W/kg}].$$

Note that, $\mathbf{x}^{1000}$ and $\mathbf{x}^{100}$ are far below the maximum SAR allowed making possible to increase the flip angle up to a factor 4 (achieving a flip angle of about 60^o). For the other numerical solutions this would not be acceptable.

4.5 Experiment

At the end of this work on RF pulse design we were able to run a first experiment on a two channels transmit system for the 7 Tesla MRI scanner at the University Medical Center, Utrecht. The goal of this test was to check whether a spatially selective excitation could be achieved by mean of two RF channels and by Gradients corresponding to a spiral scanning of the k-space. The problem of evaluating the B_1 sensitivity profiles of each coil in an accurate and robust way was, at that stage, not yet solved. To overcome this issue, we decided to scan a spherical phantom filled with oil, which gives rise to a very uniform B_1 profile hence we can assume $S_p(\vec{r}) = 1$ for all p and $\vec{r}$ in formula (3.4). The phantom had a diameter of 17 cm and we choose for a Gaussian magnetization profile, centered at the origin, corresponding to a flip angle of 15^o (see Figure 4.25). Because of the assumption $S_1(\vec{r}) = S_2(\vec{r}) = 1$ for all $\vec{r} \in$ ROI, no undersampling could be performed and the total requested time, after spiral trajectory optimization, was $T \approx 4.2$ millisec. The RF pulses found after running mCGLS were implemented in the hardware. See Figure 4.26 for a screen-shot of the hardware input showing the gradients G_x and G_y (sinusoidal curves on the top two lines), the G_z gradient (this is zero all the time, see third line from above) and the RF's amplitude (third line from the bottom).
The obtained magnetization is displayed in Figure 4.27: in the right picture is plotted the profile along the straight line from the left picture. The spatial selective magnetization following the desired Gaussian pattern is achieved. This result may be considered a good starting point for further work in this field: in particular, implementation of B_1 (and B_0) profiles has to be addressed, making possible to exploit all the advantages (e.g. speed up) of the parallel transmit system.

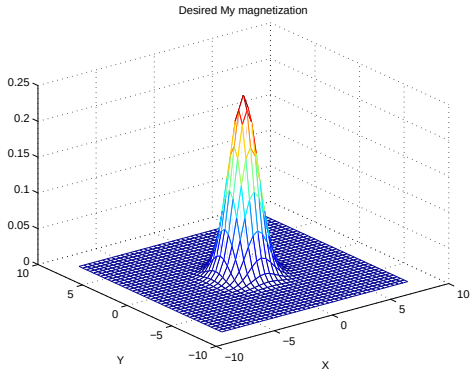

Figure 4.25: Experiment 1: desired excitation profile.

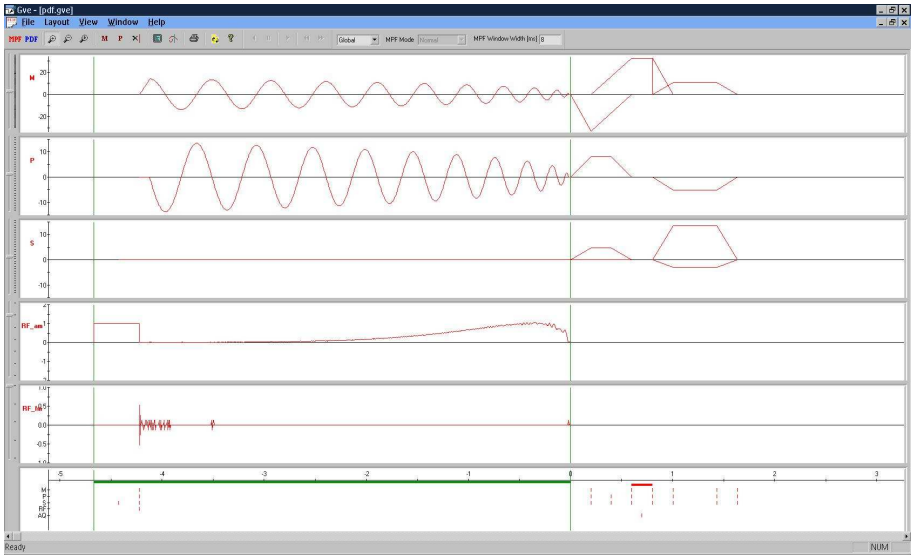

Figure 4.26: Experiment: input for the parallel transmit system (2ch) of the 7 Tesla MRI.

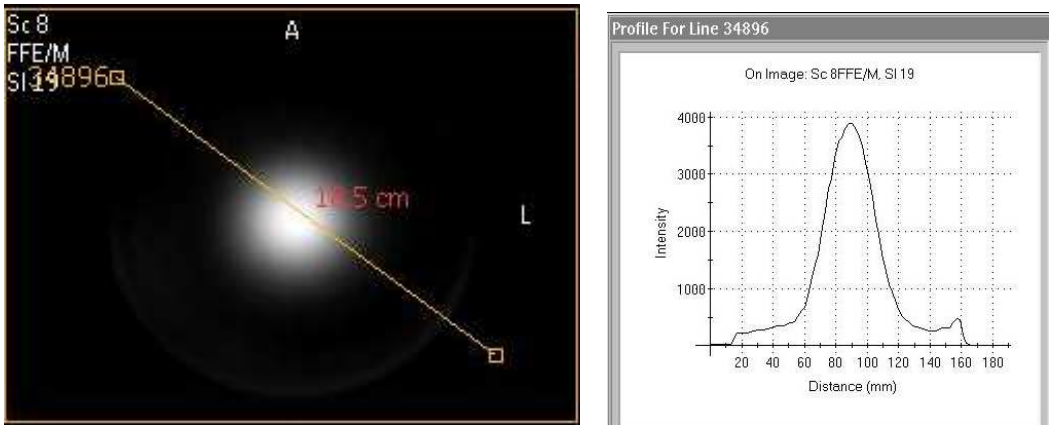

Figure 4.27: Obtained magnetization.

Chapter 5

Conclusions and Outlook

In the present work we described and studied a procedure to design RF pulses for parallel transmit system at high field MRI. The main goals were:

- to achieve spatially selective excitation and in particular
  - inner volume excitation
  - homogenization
- to shorten the RF pulse length (time speed up).

Both goals were achieved. The overall scheme we followed is:

1. choose a desired magnetization pattern
2. get B_1 (and B_0) sensitivity maps
3. calculate the optimal constrained k-space trajectory
4. construct the matrix $\mathbf{A}$ and solve the least squares problem with the mCGLS algorithm
5. choose a good numerical solution $\mathbf{x}$
6. calculate the corresponding 1-g SAR for $\mathbf{x}$ and check the SAR constraint
7. implement $\mathbf{x}$ (i.e. the RF pulse) and the gradients in the MRI hardware.

We will shortly summarize the results relative to each step and, where possible, give some outlook for further work related on the subject.

5.1 The desired magnetization pattern

In Chapter 2 we have seen how, under the assumption of low flip angle, the formula (see (2.4))

$$M_{\perp}(\vec{r},T) = i\gamma M_0 \int_0^T B_1(t) e^{i\vec{r}\cdot\vec{k}(t)} dt \tag{5.1}$$

can be derived which describes the magnetization pattern obtained for given RF pulses and gradients. Inverting the same formula, it is possible to find B_1 for a desired excitation pattern and gradients. An approximated analytic solution is also derived for the special case that the magnetization has a Gaussian profile over a two dimensional spatial domain. For general imaging applications, it may be desirable to obtain a homogeneous magnetization over a whole region, in this case the combination of Fermi functions

$$M_y(\vec{r}) = \mu_1 \left(\frac{1}{e^{\frac{\rho-\alpha}{\beta}}+1} - \frac{1}{e^{\frac{\rho+\alpha}{\beta}}+1} \right)$$

can be a valid alternative to a boxcar profile which has the disadvantage to require a long k-space scanning, due to the extent of the frequency spectrum. As we reported in Chapter 4, varying the parameter β has a filtering effect, making the transition region smoother and thus requiring less Fourier coefficients (and thus shorter pulses) for an accurate reconstruction.
In Chapter 2 we have also seen that the low flip angle formula works quite well even for flip angles of 90^o. For larger angle other strategies should be followed, this was beyond the scope of this work. For the interested reader we indicate the Shinnar-le Roux algorithm which has been developed for this scope (see also [24]).
Three dimensional spatially selective excitation could also be implemented in the design procedure by the introduction of a slice selective gradient component G_z along the z-axis. However, this would require a longer pulse and speed up becomes necessary.

5.2 The B_1 (and B_0) maps

Knowing with a good accuracy the field maps is of fundamental importance to obtain a good magnetization profile. Furthermore, we have seen that an efficient employment of the parallel transmit system requires the B_1 maps to be substantially different for each transmit channel and to have an extended frequency spectrum. In this case undersampling of the k-space can be performed without loosing accuracy in the obtained magnetization: the speed

up is the direct consequence of the reduced k-space trajectory. We have seen in chapter 4 that simulations with 8 transmit channels and eight-fold radial undersampling of the k-space trajectory can reduce the pulse length up to a factor 7 with respect to a single channel excitation. In applications, it becomes important to construct an accurate B_1 map for each patient. This requires computation time and efforts must be done to be able to perform the whole procedure in a reasonable time.

5.3 An optimal k-space trajectory

Under the Gradient and Slew rate constraints we designed an implemented an algorithm which computes an optimal k-space trajectory fulfilling the two conditions. We focused on spiral trajectories: while for circular symmetric and smooth profiles this could be a valid choice, for other more irregular profiles they are no longer the best choice. Furthermore, in the k-space scanning, also the sensitivity profile must be taken into account. Introducing the B_1 sensitivity map $S(\vec{r})$ in formula (5.1):

$$M_\perp(\vec{r}) = i\gamma M_0 \int_0^T S(\vec{r}) B_1(t) e^{i\vec{r}\cdot\vec{k}(t)} dt,$$

that is, assuming $S(\vec{r}) \neq 0$ for any $\vec{r}$:

$$\frac{M_\perp(\vec{r})}{S(\vec{r})} = i\gamma M_0 \int_0^T B_1(t) e^{i\vec{r}\cdot\vec{k}(t)} dt.$$

Denoting

$$\tilde{M}(\vec{r}) \equiv \frac{M_\perp(\vec{r})}{S(\vec{r})}$$

we see that the above formula is equivalent to formula (5.1) for $\tilde{M}$ instead of $M_\perp$. This means that we must solve (5.1) for $\tilde{M}$. In general, the inversion of the sensitivity profile S will result in an irregular $\tilde{M}$ with an irregular Fourier Transform. In this case is preferable to select the most important Fourier Coefficients (for example, those ones with the largest absolute value) and adapt the k-space trajectory to let it pass through these points in the k-space. In the literature, these reference points in k-space are called *spokes*. Suppose for instance that the desired magnetization profile is a combination of Fermi functions, to achieve an homogeneous excitation over an elliptic region and the sensitivity profile of the transmit channel is the same as for channel 1 in simulation 2d) from Chapter 4. Then the effective magnetization $\tilde{M}$ looks like that one displayed in Figure 5.1 The spokes are chosen

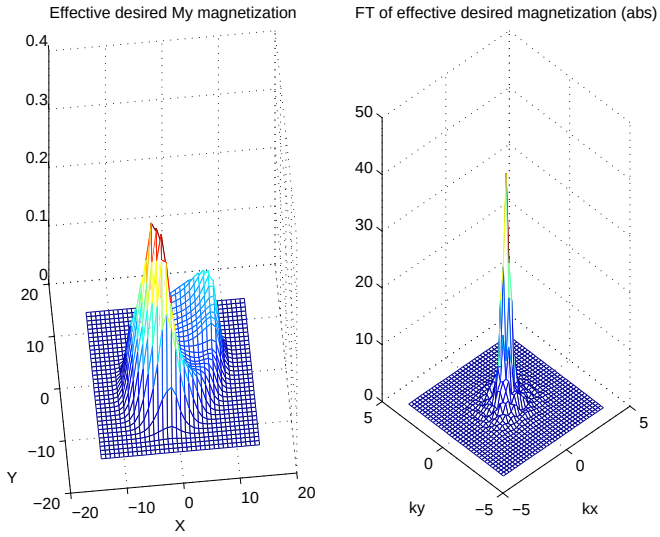

Figure 5.1: Effective desired magnetization profile $\tilde{M}$ after inversion of the sensitivity map.

as the points in the discrete Fourier transform domain of $\tilde{M}$ whose absolute value is larger than a certain thresh-value. They are displayed in Figure 5.2 (left). Designing the k-space trajectory can be done by mean of a Traveling Salesman Problem (TSP) algorithm which finds the shortest path which connect all the spokes. An example of such an adapted trajectory is displayed in Figure 5.2 (right). Of course, any k-space trajectory must satisfy the gradient and slew rate constraints, thus extra optimization work must be done. Furthermore, each transmit channel is characterized by a different S profile and thus by a different DFT of S, it follows that determining the spokes is not unambiguous and we can expect that a Least Squares Problem can be set up and applied to the search of a set of spokes which are optimal for all transmitting coils.

5.4 The Least Squares Problem and mCGLS

We have seen how important is to regularize the least squares problem

$$\text{argmin}_x \left(\|\mathbf{Ax} - \mathbf{b}\|_2^2 \right)$$

deriving form the discretization of

$$M_\perp(\vec{r}, T) = i\gamma M_0 \sum_{p=1}^{P} \left(S_p(\vec{r}) \int_0^T B_{1,p}(t) e^{i\vec{r}\cdot\vec{k}(t)} dt \right).$$

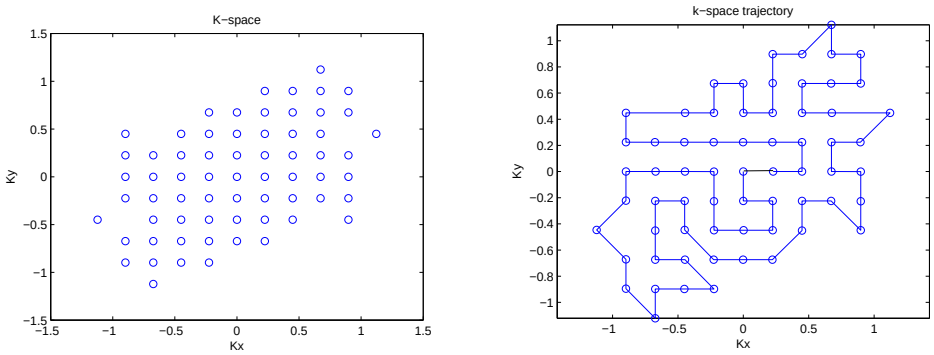

Figure 5.2: Spokes for the effective magnetization profile (left) and k-space trajectory computed by a TSP algorithm (right).

The Matrix $\mathbf{A}$ will be in general ill-conditioned and the numerical solutions will suffer from the instability. As a consequence, perturbations in the matrix $\mathbf{A}$ (which may be caused, for instance, by errors in the B_1-map evaluations or by approximations of the discretized integral and k-space trajectory) lead to large errors in the numerical solutions.
Regularizing the least square problem by mean of parameters $\lambda_j \in \Lambda$ is necessary but it can be time consuming when the corresponding system of normal equations

$$(\mathbf{A}^T\mathbf{A} + \lambda\mathbf{I})\mathbf{x}^\lambda = \mathbf{A}^T\mathbf{b}$$

is solved separately for each $\lambda \in \Lambda$. A good alternative is a multi-shift algorithm: it computes simultaneously $\mathbf{x}^\lambda$ for each $\lambda \in \Lambda$ in such a way that the main computational burden, that is, the two matrix-vector products, are computed only once per iteration step. The algorithm we employ, namely mCGLS, has the major advantage to be also highly stable.
A valuable extension to the regularized least squares problem could be the additional implementation of a penalty on the second derivative of $\mathbf{x}^\lambda$ by mean of the term $\|\mathbf{L}_{\lambda,\eta}\mathbf{x}^\lambda\|^2$ instead of $\lambda\|\mathbf{x}^\lambda\|^2$ in the mCGLS algorithm (see the discussion in Section 4.4). This would result into a smoother RF profile and thus into less amplifier distortion.

5.5 The choice of a good numerical solution

The output of the mCGLS algorithm is a set of numerical solutions $\mathbf{x}^\lambda$ for $\lambda \in \Lambda$. The L-curve helps to visualize the relation between the residual and the norm of these solutions. As a rule of thumb, the optimal numerical

solution has to be chosen among those ones whose L-curve representation lies closer to the origin, that is, when both solution norm and residual norm are minimized. However, as we have seen in Chapter 4, having a Bloch Equation Simulator at our disposal offers an extra possibility for an optimal choice: after having run the simulator for each $\mathbf{x}^{\lambda}$, we are able to quantify the error between the desired magnetization profile and the simulated ones: the choice is then straightforward.

5.6 SAR computation

A final, patient's safety-related constraint is the maximum 1-g SAR. Before any RF pulse can be implemented and employed in human MRI it must fulfill the SAR constraint

$$\max_{\vec{r}} \text{1g-SAR}(\vec{r}) \leq \text{SAR}_{\max}.$$

Given the square dependence between $\max_{\vec{r}}$ 1g-SAR$(\vec{r})$ and $\|\mathbf{x}\|$ which is proportional to the flip angle, reduction of the SAR can be obtained by scaling the RF pulse (and thus the flip angle) or choosing another numerical solution with a smaller norm and still acceptable error from the simulation. However, for sake of efficiency, we would like to adapt the least squares problem in step 4 and add the SAR constraint to it. For a typical clinical set up, the computation of 1g-SAR$(\vec{r})$ requires an amount of flops of order 10^9 for each RF pulse. Implementing this computation in the mCGLS algorithm is prohibitively expensive in terms of computation time if a single processor is used. The nature of the problem suggests a parallel computing approach. Once the spatial domain is divided over all processors and information regarding the electric fields are stored in the local memories, no additional communication is needed, except for the RF pulse vector: the $\max_{\vec{r}}$ 1g-SAR$(\vec{r})$ can be computed locally and, once the resulting local maximum is known, it can be sent to a central processor which determines the absolute maximum. Note that a parallelization strategy can also be followed to evaluate the B_1 sensitivity maps.

5.7 Implementation in the MRI hardware

The promising results from the simulations are confirmed by the successful first experiment at the UMC's 7 Tesla MRI scanner (parallel transmit system). The experiment we performed was a simple test: no sensitivity map was employed and the desired magnetization has a Gaussian profile. The resulting RF waveform is rather smooth (see figure 4.26). Implementing other

RF pulses with a more irregular profile, comparable with those displayed in figure 4.16, is revealing technical problems due to extra noise in the MRI hardware which sums up to the input RF pulse and cause a major distortion of the signal.

The solution of this technical problem, together with the possibility to evaluate accurately and efficiently the B_1 maps and $\max_{\vec{r}}$ 1g-SAR($\vec{r}$) are now being under investigation at the 7 Tesla research group of the UMC.

Appendix A

Derivation of the Normal Equations

Solving the least squares problems

$$\text{argmin}_x \left(\|\mathbf{Ax} - \mathbf{b}\|_2^2 \right) \tag{A.1}$$

and

$$\text{argmin}_x \left(\|\mathbf{Ax}^\lambda - \mathbf{b}\|_2^2 + \lambda \|\mathbf{x}^\lambda\|_2^2 \right) \tag{A.2}$$

is equivalent to solving, respectively, the normal equations

$$\mathbf{A}^T\mathbf{Ax} = \mathbf{A}^T\mathbf{b} \tag{A.3}$$

and

$$(\mathbf{A}^T\mathbf{A} + \lambda\mathbf{I})\mathbf{x}^\lambda = \mathbf{A}^T\mathbf{b}. \tag{A.4}$$

To see why this is true, write first

$$\|\mathbf{Ax}-\mathbf{b}\|_2^2 = (\mathbf{Ax}-\mathbf{b})^T(\mathbf{Ax}-\mathbf{b}) = \mathbf{x}^T\mathbf{A}^T\mathbf{Ax}-\mathbf{b}^T\mathbf{Ax}-\mathbf{x}^T\mathbf{A}^T\mathbf{b}+\mathbf{b}^T\mathbf{b} = f(\mathbf{x}).$$

The function f is a quadratic form. Furthermore, $\mathbf{A^TA}$ is symmetric and *Positive Definite*, that is:

$$\mathbf{x}^T\mathbf{A}^T\mathbf{Ax} > 0 \quad \forall \mathbf{x} \neq \mathbf{0}.$$

This is easy to prove, since $\mathbf{x}^T\mathbf{A}^T\mathbf{Ax} = (\mathbf{Ax})^T\mathbf{Ax} = \|\mathbf{Ax}\|^2 > 0 \quad \forall \mathbf{x} \neq \mathbf{0}$. Thus f attains the global minimum where the gradient vanishes. Writing

out the gradient:

$$\begin{aligned} f'(\mathbf{x}) &\equiv \lim_{\|\mathbf{h}\|\to\mathbf{0}} \frac{f(\mathbf{x}+\mathbf{h})-f(\mathbf{x})}{\|\mathbf{h}\|} = \\ &= \lim_{\|\mathbf{h}\|\to\mathbf{0}} \frac{(\mathbf{A}(\mathbf{x}+\mathbf{h})-\mathbf{b})^T(\mathbf{A}(\mathbf{x}+\mathbf{h})-\mathbf{b})-(\mathbf{A}\mathbf{x}-\mathbf{b})^T(\mathbf{A}\mathbf{x}-\mathbf{b})}{\|\mathbf{h}\|} \\ &= \lim_{\|\mathbf{h}\|\to\mathbf{0}} \frac{2\mathbf{h}^T(\mathbf{A}^T\mathbf{A}\mathbf{x}-\mathbf{A}^T\mathbf{b})+\mathbf{h}^T\mathbf{A}^T\mathbf{A}\mathbf{h}}{\|\mathbf{h}\|} \\ &= \lim_{\|\mathbf{h}\|\to\mathbf{0}} \left(\frac{\mathbf{h}^T}{\|\mathbf{h}\|}2(\mathbf{A}^T\mathbf{A}\mathbf{x}-\mathbf{A}^T\mathbf{b})+\frac{\mathbf{h}^T\mathbf{A}^T\mathbf{A}\mathbf{h}}{\|\mathbf{h}\|}\right). \end{aligned}$$

Note that

$$0 \le \frac{\mathbf{h}^T\mathbf{A}^T\mathbf{A}\mathbf{h}}{\|\mathbf{h}\|} = \frac{\|\mathbf{A}\mathbf{h}\|^2}{\|\mathbf{h}\|} \le \frac{\|\mathbf{A}\|^2\|\mathbf{h}\|^2}{\|\mathbf{h}\|} = \|\mathbf{A}\|^2\|\mathbf{h}\| \overset{\|\mathbf{h}\|\to\mathbf{0}}{\longrightarrow} 0,$$

thus the gradient f' vanishes if and only if

$$\lim_{\|\mathbf{h}\|\to\mathbf{0}} 2\frac{\mathbf{h}^T}{\|\mathbf{h}\|}(\mathbf{A}^T\mathbf{A}\mathbf{x}-\mathbf{A}^T\mathbf{b}) = 0.$$

For any $\mathbf{h}$, the vector $\frac{\mathbf{h}^T}{\|\mathbf{h}\|}$ has length 1, thus the above limit can be 0 if and only if

$$\mathbf{A}^T\mathbf{A}\mathbf{x}-\mathbf{A}^T\mathbf{b}=\mathbf{0} \quad \Leftrightarrow \quad \text{Eq.}(A.3).$$

For the regularized least squares problem (A.2) write

$$\|\mathbf{A}\mathbf{x}^\lambda-\mathbf{b}\|_2^2+\lambda\|\mathbf{x}^\lambda\|_2^2 = \left\|\begin{bmatrix}\mathbf{A}\mathbf{x}^\lambda-\mathbf{b}\\ \sqrt{\lambda}\mathbf{x}^\lambda\end{bmatrix}\right\|_2^2 = \left\|\begin{bmatrix}\mathbf{A}\\ \sqrt{\lambda}\mathbf{I}\end{bmatrix}\mathbf{x}^\lambda-\begin{bmatrix}\mathbf{b}\\ \mathbf{0}\end{bmatrix}\right\|_2^2$$

where $\mathbf{I}$ denotes the identity matrix whose number of columns equals the number of columns of $\mathbf{A}$.
It follows that the problem (A.2) is equivalent to the problem

$$\text{argmin}_x\left(\|\tilde{\mathbf{A}}\mathbf{x}^\lambda-\tilde{\mathbf{b}}\|_2^2\right)$$

with

$$\tilde{\mathbf{A}} \equiv \begin{bmatrix}\mathbf{A}\\ \sqrt{\lambda}\mathbf{I}\end{bmatrix} \quad \text{and} \quad \tilde{\mathbf{b}} \equiv \begin{bmatrix}\mathbf{b}\\ \mathbf{0}\end{bmatrix}.$$

The solution to this modified least square problem is given by the solution of the normal equation (A.3) applied to $\tilde{\mathbf{A}}$, $\mathbf{x}^\lambda$ and $\tilde{\mathbf{b}}$. The corresponding normal equation becomes

$$\tilde{\mathbf{A}}^T\tilde{\mathbf{A}}\mathbf{x}^\lambda = \tilde{\mathbf{A}}^T\tilde{\mathbf{b}} \Leftrightarrow \begin{bmatrix}\mathbf{A}^T & \sqrt{\lambda}\mathbf{I}\end{bmatrix}\begin{bmatrix}\mathbf{A}\\ \sqrt{\lambda}\mathbf{I}\end{bmatrix}\mathbf{x}^\lambda = \begin{bmatrix}\mathbf{A}^T & \sqrt{\lambda}\mathbf{I}\end{bmatrix}\begin{bmatrix}\mathbf{b}\\ \mathbf{0}\end{bmatrix},$$

that is:

$$(\mathbf{A}^T\mathbf{A}+\lambda\mathbf{I})\mathbf{x}^\lambda = \mathbf{A}^T\mathbf{b}.$$

Appendix B

The Bloch Simulator

In the following we will shortly describe how the Bloch Equation simulators work. See also [7] and [22].
The Bloch equation in matrix form (2.2) describes a rotation of $\vec{M}$ in $\mathbb{R}^3$. To get more insight in this process, rewrite first (2.2) as

$$\frac{d\vec{M}(t)}{dt} = \mathbf{C}(t)\vec{M}(t) \tag{B.1}$$

with

$$\mathbf{C}(t) = \begin{pmatrix} 0 & \gamma\vec{G}\cdot\vec{r} & -\gamma B_{1,y} \\ -\gamma\vec{G}\cdot\vec{r} & 0 & \gamma B_{1,x} \\ \gamma B_{1,y} & -\gamma B_{1,x} & 0 \end{pmatrix}.$$

Consider a RF pulse in the piecewise constant approximation $B_1(t) = B_1(t_j)$ for $t \in [t_j, t_{j+1})$, $j = 0, 1, 2, \ldots, N_t - 1$ and $t_{j+1} - t_j = \Delta t$ (note that this approximation is actually the true version of B_1 when it is sampled and implemented in the MRI transmit hardware). The Bloch equation in the time interval $[t_j, t_j + \Delta t)$ becomes

$$\frac{d\vec{M}(t)}{dt} = \mathbf{C_j}\vec{M}(t) \tag{B.2}$$

with $\mathbf{C_j} \equiv \mathbf{C}(t_j)$. In this case the solution to (B.2) is straightforward:

$$\vec{M}_{j+1} = e^{\mathbf{C_j}\Delta t}\vec{M}_j. \tag{B.3}$$

where $\vec{M}_j \equiv \vec{M}(t_j)$.
The matrix $\mathbf{C_j}$ is Anti-hermitian (that is: ${\mathbf{C_j}}^H = -\mathbf{C_j}$), it follows that $e^{\mathbf{C_j}\Delta t}$ is an unitary matrix (i.e. $e^{\mathbf{C_j}\Delta t} = \mathbf{R_j}$ with ${\mathbf{R_j}}^H\mathbf{R_j} = \mathbf{I}$) and thus it represents a rotation in $\mathbb{R}^3$. Setting $\mathbf{R_j} \equiv e^{\mathbf{C_j}\Delta t}$ the total rotation will be

$$\vec{M}_{N_t} = \mathbf{R_{N_t-1}R_{N_t-2}}\ldots\mathbf{R_1R_0}\vec{M}_0.$$

The magnetization at the end of the RF pulse can be expressed as

$$\vec{M}(T) = \mathbf{R}\vec{M}(0)$$

with

$$\mathbf{R} = \mathbf{R_{N_t-1}R_{N_t-2}}\dots\mathbf{R_1R_0}$$

and, assuming the initial magnetization is aligned along the $\vec{B}_0$ field (equilibrium):

$$\vec{M}(0) = \begin{pmatrix} 0 \\ 0 \\ 1 \end{pmatrix}.$$

To find a closed form for the matrices $\mathbf{R_j}$ consider the following argument: using the spin matrices

$$\mathbf{S_x} = \begin{pmatrix} 0 & 0 & 0 \\ 0 & 0 & -1 \\ 0 & 1 & 0 \end{pmatrix} \quad \mathbf{S_y} = \begin{pmatrix} 0 & 0 & 1 \\ 0 & 0 & 0 \\ -1 & 0 & 0 \end{pmatrix} \quad \mathbf{S_z} = \begin{pmatrix} 0 & -1 & 0 \\ 1 & 0 & 0 \\ 0 & 0 & 0 \end{pmatrix}$$

we can rewrite $\mathbf{C_j}$ as

$$\mathbf{C_j} = \left(-\gamma B^j_{1,x}\mathbf{S_x} - \gamma B^j_{1,y}\mathbf{S_y} - \gamma(\vec{G}^j \cdot \vec{r})\mathbf{S_z}\right). \tag{B.4}$$

The vector $\vec{\Omega}_j = (-\gamma B^j_{1,x}, -\gamma B^j_{1,y}, -\gamma(\vec{G}^j \cdot \vec{r}))$ describes the axis and the velocity of the rotation during the time interval $[t_j, t_j + \Delta t)$: the angular velocity is

$$\omega_j \equiv -\|\vec{\Omega}_j\| = -\gamma\sqrt{(B^j_{1,x})^2 + (B^j_{1,y})^2 + (\vec{G}^j \cdot \vec{r})^2}$$

and the axis of the rotation is given by the unit vector

$$\hat{n}_j \equiv -\frac{\vec{\Omega}_j}{\|\vec{\Omega}_j\|} = \frac{\gamma}{|\omega_j|}\left(B^j_{1,x}, B^j_{1,y}, (\vec{G}^j \cdot \vec{r})\right).$$

Finally, setting

$$\begin{aligned} \tilde{\mathbf{C}}_\mathbf{j} &\equiv \frac{1}{\omega_j}\mathbf{C_j} \\ \text{and} \quad \theta_j &\equiv \omega_j \Delta t \end{aligned}$$

we have $\mathbf{R_j} = e^{\tilde{\mathbf{C}}_\mathbf{j}\theta_j}$ which can be expressed in closed form by mean of the Rodrigues' Rotation Formula (see, for instance, [23]).

Instead of evaluating the above 3×3 matrices, Bloch Equation simulators usually make use of the more compact, two-dimensional, *spinor representation* or, in mathematical terms, the *Special Unitary Group* $\mathrm{SU}_2(\mathbb{C})$. The underlying principle is the same we have seen above, namely: calculate the rotation matrix corresponding to each j-th time step and multiply them all to obtain the final magnetization. Below some more detail.
Write the magnetization vector $\vec{M}$ as a new vector (called spinor) $\vec{\Psi} = (\alpha, \beta)^T \in \mathbb{C}^2$. The relation between the magnetization and the spinor is given by the following formulas:

$$M_x = \vec{\Psi}^H \sigma_x \vec{\Psi} \qquad M_y = \vec{\Psi}^H \sigma_y \vec{\Psi} \qquad M_z = \vec{\Psi}^H \sigma_z \vec{\Psi} \tag{B.5}$$

where σ_x, σ_y and σ_z are the Pauly matrices

$$\sigma_x = \begin{pmatrix} 0 & 1 \\ 1 & 0 \end{pmatrix} \quad \sigma_y = \begin{pmatrix} 0 & -i \\ i & 0 \end{pmatrix} \quad \sigma_z = \begin{pmatrix} 1 & 0 \\ 0 & -1 \end{pmatrix} .$$

The differential equation (B.2) takes the following form:

$$\begin{aligned} \frac{d\vec{\Psi}(t)}{dt} &= \frac{i}{2}\left(-\gamma B^j_{1,x}\sigma_x - \gamma B^j_{1,y}\sigma_y - \gamma(\vec{G}^j \cdot \vec{r})\sigma_z\right)\vec{\Psi}(t) \\ &= \frac{i\omega_j}{2}\left(n^j_x\sigma_x + n^j_y\sigma_y + n^j_z\sigma_z\right)\vec{\Psi}(t) \end{aligned}$$

with ω_j and $\hat{n}^j = (n^j_x, n^j_y, n^j_z)^T$ as defined above (that is the angular velocity and the rotation axis respectively). Under the assumption of piecewise constant RF pulse and gradients, we can write, in analogy with (B.3):

$$\vec{\Psi}_{j+1} = e^{\frac{i\omega_j}{2}\mathbf{\Sigma_j}\Delta t}\vec{\Psi}_j = e^{\frac{i\omega_j\Delta t}{2}\mathbf{\Sigma_j}}\vec{\Psi}_j = \mathbf{Q_j}\vec{\Psi}_j \tag{B.6}$$

where we set $\mathbf{\Sigma_j} \equiv \left(n^j_x\sigma_x + n^j_y\sigma_y + n^j_z\sigma_z\right)$ and $\mathbf{Q_j} \equiv e^{\frac{i\omega_j\Delta t}{2}\mathbf{\Sigma_j}}$. The unitary matrix $\mathbf{Q_j}$ can be expressed in the following form:

$$\mathbf{Q_j} = \begin{pmatrix} \alpha_j & -\beta^*_j \\ \beta_j & \alpha^*_j \end{pmatrix}$$

with

$$\begin{aligned} \alpha_j &= \cos(\omega_j\Delta t/2) - i\, n_z \sin(\omega_j\Delta t/2) \\ \beta_j &= -i(n_x + in_y)\sin(\omega_j\Delta t/2) \end{aligned}$$

the so called *Cayley-Klein* parameters. We finally obtain the following expression for the spinor at the end of the RF pulse:

$$\vec{\Psi}_{N_t} = \mathbf{Q}_{N_t-1}\mathbf{Q}_{N_t-2}\ldots\mathbf{Q}_0\vec{\Psi}_0$$

with

$$\vec{\Psi}_0 = \begin{pmatrix} 1 \\ 0 \end{pmatrix}.$$

The Bloch Simulator computes stepwise the Cayley-Klein parameters, forms the matrices $\mathbf{Q_j}$ and, once $\vec{\Psi}_{N_t} = (\alpha, \beta)^T$ is found, back transformation to the transversal magnetization is obtained through formulas (B.5), that is:

$$\begin{aligned} M_x &= \alpha^*\beta + \beta^*\alpha \\ M_y &= -i\alpha^*\beta + i\alpha\beta^* \\ M_z &= \alpha^*\alpha - \beta^*\beta. \end{aligned}$$

Bibliography

[1] E. Mark Haacke, Robert W. Brown, Michael R. Thompson, Ramesh Venkatesan, *Magnetic Resonance Imaging*, Wiley, 1999

[2] `www.magnet.fsu.edu/education/tutorials/magnetacademy/mri/`

[3] `www.e-mri.org`

[4] `http://www.phys.cwru.edu/courses/p431/notes-2003`

[5] J. Pauly, D. Nishimura, and A. Macovski, *A k-space Analysis of Small-Tip-Angle Excitation*, J. Magn. Res. 81,43-56 (1989)

[6] M. T. Vlaardingerbroek and J. A. den Boer, *Magnetic Resonance Imaging. Theory and Practice*, Springer, 1996

[7] J. Pauly *Class Handouts for the course "RF Pulse Design for Magnetic Resonance Imaging"* available at the author's website `http://www.stanford.edu/~pauly/` December 2006

[8] Klaas P. Pruessmann, Markus Weiger, Markus B. Scheidegger and Peter Boesiger *SENSE: Sensitivity Encoding for Fast MRI*, Magn. Reson. Med. 42,952-962 (1999)

[9] David O. Brunner and Klaas P. Pruessmann B_1^+ *Interferometry for the Calibration of RF Transmitter Arrays* Magn. Reson. Med. 61, 1480-1488 (2009)

[10] Glen R. Morrel *A Phase-Sensitive Method of Flip Angle Mapping* Magn. Reson. Med. 60, 889-894 (2008)

[11] Jung-Jiin Hsu, Greg Zaharchuk and Gary H. Glover *rapid Methods for Concurrent measurements of the RF-Pulse Flip Angle and the Longitudinal Relaxation Time* Magn. Reson. Med. 61,1319-1325 (2009)

[12] Ulrich Katscher, Peter Börnert, Christoph Leussler and Johan S. van den Brink *Transmit SENSE* Magn. Reson. Med. 49,144-150 (2003)

[13] Gene H. Golub and Charles F. Van Loan *Matrix Computations* Third edition, Baltimore 1996.

[14] Per Christian Hansen *Regularization Tools. A Matlab Package for Analysis and Solution of Discrete Ill-Posed Problems* Technical University of Denmark , March 2008. Available at the author's website `http://www.imm.dtu.dk/~pch`

[15] A. C. Zelinski, L. M. Angelone, V. K Goyal, G. Bonmassar, E. Adalsteinsson, L. L. Wald *Specific Absorption Rate Studies of the Parallel Transmission of Inner-Volume Excitations at 7 Tesla* J. Magn. Reson. Imaging 2008, 28, 1005-1018, (2008)

[16] Jasper van den Eshof and Gerard L.G. Sleijpen *Accurate gradient methods for families of shifted systems* Applied Numerical Mathematics, 49,17-37 (2004)

[17] Andreas Frommer and Peter Maas *Fast CG-Based Methods for Tikhonov-Phillips Regularization* SIAM J. Sci. Comput. 20,1831-1850 (1999)

[18] Christopher J. Hardy and Harvey E. Cline *Broadband nuclear magnetic resonance pulses with two-dimensional spatial selectivity* J. Appl. Phys. 66,1513-1516 (1989)

[19] Yi Wang *Description of Parallel Imaging in MRI Using Multiple Coils* Magn. Res. Med. 44, 495-499 (2000)

[20] Klaas P. Pruessmann *Encoding and Reconstruction in Parallel MRI* NMR Biomed. 19, 288-299 (2006)

[21] Grissom W., Yip C., Zhang Z., Stenger V.A., Fessler J. A. and Noll D. C. *Spatial Domain Method for the design of RF Pulses in Multicoil Parallel Excitation* Magn. Reson. Med. 56, 620-629 (2006)

[22] E. T. Jaynes *Matrix Treatment of Nuclear Induction*, The Physical Review, 98, 1099-1105 (1955)

[23] `http://mathworld.wolfram.com/RodriguesRotationFormula.html`

[24] Pauly J, Nishimura D, Macovski A. *A linear class of large-tip-angle selective excitation pulses*, J Magn Reson 1989; 82(3):571-587